Lire
la première partie
de la thèse

Part II

High-fidelity simulations of azimuthal modes

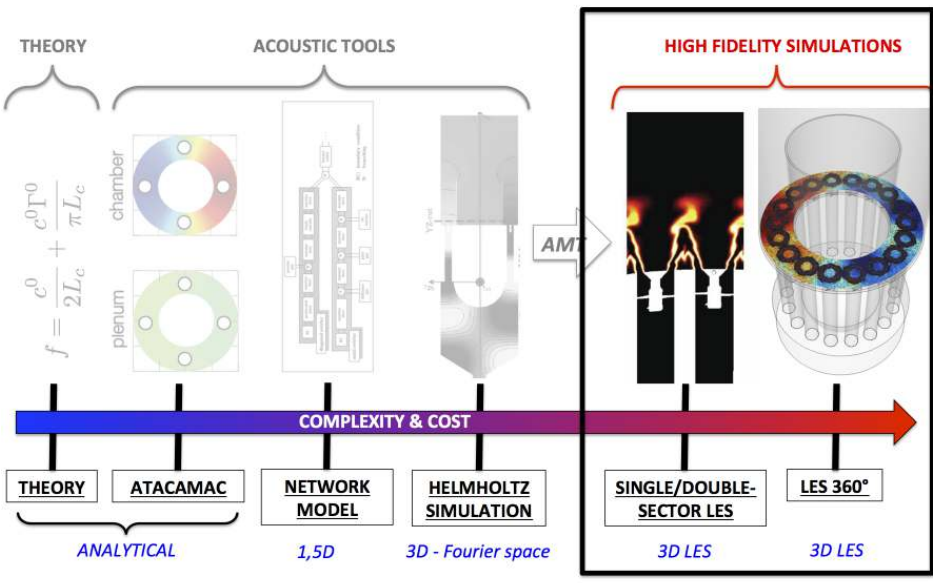

This part has lead to the following publications and communications:

1) M. Bauerheim, G. Staffelbach, N.A. Worth, J.R. Dawson, L. Gicquel and T. Poinsot, *'Sensitivity of LES-based harmonic flame response model for turbulent flames and impact on the stability of azimuthal modes' (2014)* **Proceedings of the 35th Combustion Institute** (in press, DOI 10.1016/j.proci.2014.07.021)
2) M. Bauerheim, L. Gicquel and T. Poinsot, *'Numerical investigation of azimuthal combustion instabilities in annular combustors' (2014)*, **CRCT, Centrale Paris, FRANCE**
3) M. Bauerheim, G. Staffelbach, N.A. Worth, J.R. Dawson, L. Gicquel and T. Poinsot, *'Numerical and experimental investigation of the establishment of azimuthal modes in an academic annular combustor'* **(in preparation)**

Chapter 6

Large Eddy Simulations and AVBP

This chapter gives a general introduction to Computational Fluid Dynamics and presents the concept and the governing equations for Large Eddy Simulations of turbulent reactive flows. It summarize models used in the AVBP code for reactive LES of combustors. The specific reduced kinetic schemes for methane and ethylene used and/or developed for the Cambridge experiment are presented. Transport coefficients used in the AVBP code have been validated. Finally, turbulent combustion modeling, a key feature of reacting flow computations, is briefly described.

(a) Claude Louis Navier (1785-1836).

(b) George Gabriel Stokes (1819-1903).

6.1 An introduction to Computational Fluid Dynamics

The aim of fluid mechanics is to study liquids and gases properties in various configurations, initially to predict its motion. The history of the equations governing the motion of a fluid started in 1757 when Leonhard Paul Euler published an important set of equations

to describe the motion of inviscid flows that are known as the Euler equations. Then in 1822 Claude-Louis Navier, a French engineer, introduced the notion of viscosity. Finally in 1845 George Gabriel Stokes wrote the final equations describing the motion of a viscous fluid (including the terms proposed by C.L. Navier). These nonlinear partial differential equations are now known as the 'Navier-Stokes equations'. They are used to study a wide range of situations: the design of aircraft and cars, the study of blood flows, the weather or ocean currents. Except in some very simple cases where analytical solutions exist, these nonlinear equations have to be solved numerically on computers: this field is called Computational Fluid Dynamics (CFD).

First, Section 6.1.1 presents the governing equations in fluid dynamics and then a short description of the methods to solve them is provided in Sec. 6.1.2.

6.1.1 The Navier-Stokes equations

The exact behavior of complex turbulent reacting flows is fully described by the following 'full' Navier-Stokes equations:

$$\frac{\partial \rho}{\partial t} + \frac{\partial}{\partial x_i}(\rho u_i) = 0 \quad \text{(Mass conservation)} \tag{6.1}$$

$$\frac{\partial \rho u_j}{\partial t} + \frac{\partial}{\partial x_j}(\rho u_i u_j) = -\frac{\partial}{\partial x_j}\left(P\delta_{ij} - \tau_{ij}\right) \quad \text{(Momentum conservation)} \tag{6.2}$$

$$\frac{\partial \rho E}{\partial t} + \frac{\partial}{\partial x_j}(\rho E u_j) = -\frac{\partial}{\partial x_j}[u_i(P\delta_{ij} - \tau_{ij}) + q_j] + \dot{\omega}_T \quad \text{(Energy conservation)} \tag{6.3}$$

$$\frac{\partial \rho Y_k}{\partial t} + \frac{\partial}{\partial x_j}(\rho Y_k u_j) = -\frac{\partial}{\partial x_j}(J_{j,k}) + \dot{\omega}_k \quad \text{(Specie } k \text{ conservation)} \tag{6.4}$$

where ρ is the mixture density, u_i is the i-component of the velocity, P is the static pressure, τ_{ij} is the viscous tensor, E is the energy, q_i is the i-component of the the energy flux, $\dot{\omega}_T$ is the heat release due to combustion, Y_k is the mass fraction of species k, $J_{i,k}$ is the i-component of the diffusive flux of species k and $\dot{\omega}_k$ is the reaction rate of species k.

Assuming a Newtonian fluid and the equality between the mechanical and dynamic pressure (Stokes assumption, null bulk viscosity) leads to:

$$\tau_{ij} = 2\mu S_{ij} + \mu_V S_{kk}\delta_{ij} = 2\mu\left(S_{ij} - \frac{1}{3}\delta_{ij}S_{kk}\right) \tag{6.5}$$

with μ the dynamic viscosity, μ_V is the volume (or second) viscosity and S_{ij} is the deformation tensor:

$$S_{ij} = \frac{1}{2}\left(\frac{\partial u_j}{\partial x_i} + \frac{\partial u_i}{\partial x_j}\right). \tag{6.6}$$

When combustion instabilities arise, viscosity mainly affects the acoustic damping and the sound speed field. From a linearization of the Navier-Stokes equations, Stokes (1845) expressed the sound speed and damping of acoustic waves due to tangential forces:

$$c = \sqrt{\gamma r \bar{T} - \frac{16\pi^2\mu^2}{9\lambda^2\bar{\rho}^2}} \quad \text{and} \quad \alpha = \frac{8\pi^2\mu}{3\lambda^2\bar{\rho}} \tag{6.7}$$

where c is the sound speed, α is the acoustic damping and λ is the acoustic wavelength. It appears that the damping (due to viscosity) and sound speed field can be approximated by $\alpha = 0$ and $c = \sqrt{\gamma r \bar{T}}$ since typical values of viscosity are 10^{-5}. Moreover, the damping increases as $1/\lambda^2 \sim \omega^2$ and therefore should be considered only at high frequencies and can be neglected for azimuthal modes which usually occur at low frequencies.

The reaction term is expressed as:

$$\dot{\omega}_T = -\sum_{k=1}^{N_s} \Delta h^0_{f,k} \dot{\omega}_k \tag{6.8}$$

where N_s is the number of species in the flow, $h^0_{f,k}$ is the mass enthalpy of formation of species k at $T = T_0$ and $\dot{\omega}_k$ is the reaction rate of species k. All details on $\dot{\omega}_k$ are given in Sec. 6.4. The computation of the exact formulation of the diffusive flux of species k, $J_{i,k}$, is a very difficult and costly task. A first-order approximation of this diffusive flux (approximation of Hirschfelder *et al.*, 1969) reads:

$$J_{i,k} = -\rho \left(D_k \frac{W_k}{\overline{W}} \frac{\partial X_k}{\partial x_i} - Y_k V_i^c \right),$$

where D_k is not a binary diffusion but an equivalent diffusion coefficient of species k in the rest of the mixture. In the AVBP code, a simpler formulation of these diffusion coefficients are used:

$$D_k = \frac{1 - Y_k}{\sum_{j \neq k} X_j / D_{jk}} \simeq \frac{\mu}{\rho S_{c,k}} \quad \text{where } S_{c,k} \text{ are constant parameters} \tag{6.9}$$

W_k is the molecular weight of species k and $\overline{W}$ is the mean molecular weight of the mixture. X_k is the mole fraction of species k and Y_k is the mass fraction of species k. V_i^c is a correction velocity to ensure global mass conservation:

$$V_i^c = \sum_{k=1}^{N_s} D_k \frac{W_k}{\overline{W}} \frac{\partial X_k}{\partial x_i} \tag{6.10}$$

This correction velocity impacts the heat flux term in multi-species flows: an additional term appears in the diffusive heat flux due to heat transport by species diffusion. The total heat flux vector then reads:

$$q_i = \underbrace{-\lambda_q \frac{\partial T}{\partial x_i}}_{\text{Heat conduction}} \underbrace{- \rho \sum_{k=1}^{N_s} \left(D_k \frac{W_k}{\overline{W}} \frac{\partial X_k}{\partial x_i} - Y_k V_i^c \right) h_{s,k}}_{\text{Heat flux through species diffusion}} \tag{6.11}$$

where λ_q is the heat conduction coefficient of the mixture.

6.1.2 Turbulence and simulation

Unfortunately, the exact resolution of Eqs. 6.1 - 6.4 using Computational Fluid Dynamics (CFD) for turbulent flows in complex geometries is and will remain a challenge for a long time. Indeed, turbulent flows are characterized by a wide range of length scales (eddies): from the integral scale (the largest) to the 'Kolmogorov' scales (the smallest). The size of the largest eddies l_t is typically of the order of the geometry considered. These structures contain most of the energy of the flow. The smallest eddies are the ones where the energy is dissipated. There is a 'cascade' of energy from the large scale to the smallest scales because large eddies interact with each other and breakdown into smaller eddies. The size of the Kolmogorov scale is noted η. Kolmogorov showed in 1941 (Kolmogorov, 1941) that the ratio between the integral length scale l_t and η is (see Fig. 6.2):

$$\frac{l_t}{\eta} = Re_t^{3/4} = \frac{\rho u' l_t}{\mu} \tag{6.12}$$

where Re_t is the turbulent Reynolds number based on a turbulent velocity u' and the integral length scale. The ratio l_t/η represents the number of points in each direction required to compute all the scales in the flow. Therefore, the total number of points N_{pt} needed to compute the flow in the three dimensions scales as:

$$N_{pt} \simeq \left(Re_t^{3/4}\right)^3 = Re_t^{9/4} \tag{6.13}$$

For example, lets imagine the number of points required to compute the flow in the Dawson's experiment computed in this PhD. thesis: the mean velocity at the bluff body exit is $U_{bb} = 18\ m/s$. Assuming that the turbulent velocity is five percent of this value leads to: $u' \simeq 0.05 \times U_{bb} = 0.9\ m/s$. The integral length scale can be approximated here by the chamber width which is 2.2 times the burner diameter (D) so that $2.2 \times D \simeq l_t \simeq 77\ mm$, the turbulent Reynolds number being therefore:

$$Re_t = \frac{\rho U_{bb} L_c}{\mu} = \frac{1.2 \times 0.9 \times 0.077}{1.8.10^{-5}} \simeq 4.6\ 10^3 \tag{6.14}$$

According to Eq. 6.13, the total number of grid points needed to compute this configuration is around $N_{pt} = 1.75\ 10^8$ which is not feasible considering current computer resources.

Therefore, three numerical approaches with different resolutions have been developed to describe flows using CFD:

- the Reynolds Averaged Navier-Stokes (RANS) computations have historically been the first possible approach thanks to their affordable computational costs. RANS techniques were developed to solve the mean values of all quantities. The balance equations for the averaged quantities are obtained by averaging the instantaneous balance of equations and require closure models for turbulence and combustion.

- The second level corresponds to Large Eddy Simulations (LES). The largest scale of the turbulence are explicitly calculated whereas the effects of smaller scales are modeled using subgrid closure rules. The balance of equations for LES are obtained by filtering the instantaneous balance of equations. unlike RANS, LES capture instantaneous motions and not only mean values.
- The third level of computations is Direct Numerical Simulations (DNS) where the full instantaneous Navier-Stokes equations are solved without any model for turbulent motions: all turbulence scales are explicitly determined. DNS would predict all time variations exactly like a high-resolution sensor in an experiment. This approach has changed the analysis of turbulent combustion but DNS requires a very important computational cost. Today, this approach is mainly used to study flows in academic configurations (low Reynolds number, very small configuration).

Figure 6.1 shows an example of the time evolution of local temperature predicted by RANS, LES or DNS for a stabilized flame. RANS capture only the mean value, LES capture the low frequency variations and DNS captures all time variations. These prop-

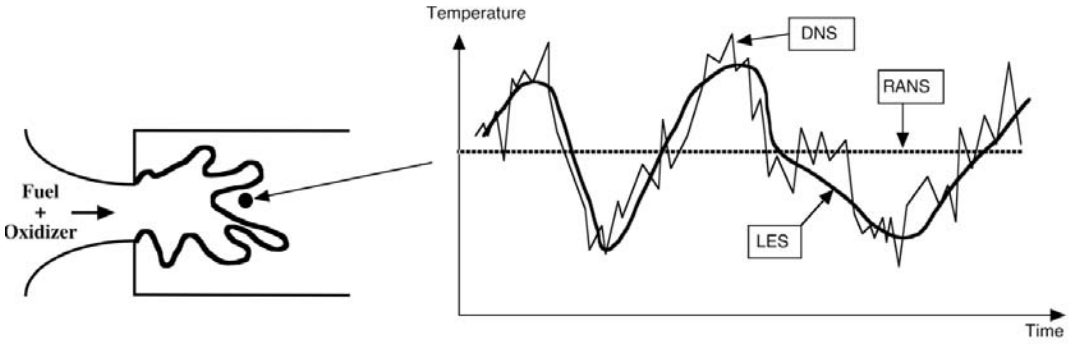

Figure 6.1: Time evolutions of local temperature computed with RANS, LES or DNS in a turbulent brush (Poinsot & Veynante, 2011).

erties can also be presented in terms of energy spectra as shown by Fig. 6.2. All spatial frequencies are resolved in DNS. In LES, the largest scales (up to a cut-off wave number k_c) are computed whereas the smallest are modeled. By construction, LES is expected to tend toward DNS when the cut-off length goes to zero (*ie.* the mesh is fine). In RANS, only mean flow fields are resolved: no turbulent motion is explicitly calculated.

6.2 The LES concept

Large Eddy Simulation is nowadays recognized as an intermediate approach in comparisons to classical RANS methodologies and expensive DNS. As previously discussed, in RANS, only mean fields are calculated (the derivation of the method consists in a temporal averaging of the Navier-Stokes equations Eqs. 6.1 - 6.4). It means than only a steady state can be expected. The unclosed terms (appearing during the derivation of the mean equations) are representative of the physics taking place over the entire range of

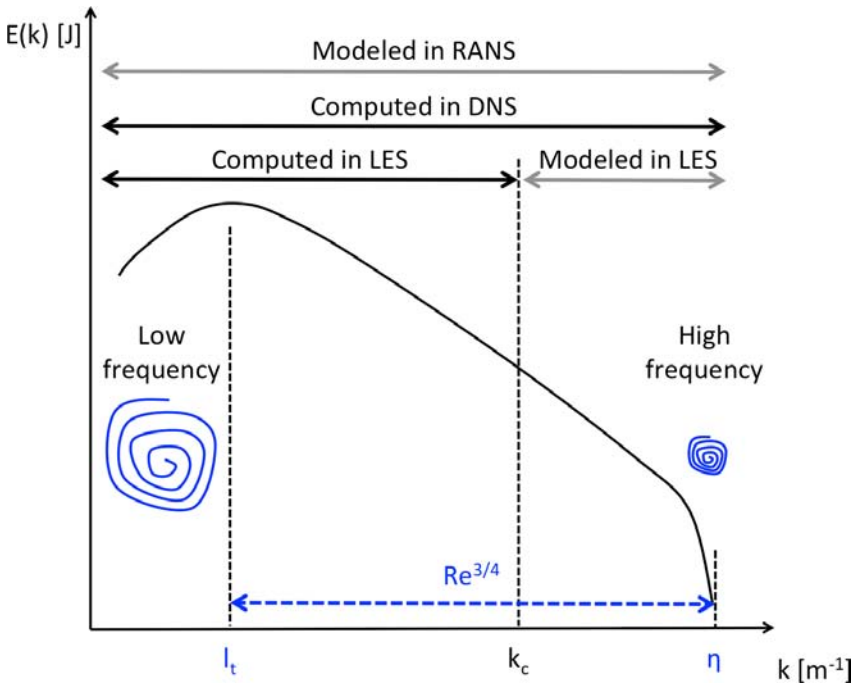

Figure 6.2: Log-log turbulence energy spectrum versus wave number. k_c is the cut-off wave number used in LES.

frequencies (see Fig. 6.2) and the closure models have an important prediction job to do. It explains the big impact of the model on the results. In LES, the operator is a spatially localized time independent filter of given size Δ. This 'spatial average' creates a separation between the large (greater than the filter size) and small (smaller than the filter size) scales. The unclosed terms are in LES representative of the physics associated with the small structures (with high frequencies) present in the flow. LES allows a dynamic representation of the large scale motions whose contributions are critical in complex geometries. The LES predictions of complex turbulent flows are henceforth closer to the physics since large scale phenomena such as large vortex shedding and acoustic waves are embedded in the set of governing equations.

For these reasons, LES has a clear potential in predicting turbulent flows encountered in industrial applications. All simulations performed in this thesis are LES, realized with the AVBP code developed at CERFACS and IFPEN on different grids to ensure grid dependency.

6.3 Multi-species flows

Combustion necessarily involves multi-species flows: at least one fuel (for example methane CH_4) and one oxidizer (for example O_2). In this section, the equation of state, the transport coefficients and the thermodynamical variables (enthalpy, energy and entropy) of such flows are presented.

6.3.1 The equation of state

In a flow composed of N_s species, the proportion of each species k can be described by its mass fraction Y_k or by its molar fraction X_k. Y_k (resp. X_k) is defined as the mass (resp. the mole number) of species k, m_k (resp. n_k) divided by the total mass m (resp. the total mole number n) in a given volume: $Y_k = m_k/m$ (reps. $X_k = n_k/n$). Necessarily, $\sum_k X_k = \sum_k Y_k = 1$.

The equation of state for an ideal gas mixture writes:

$$P = \rho r T \tag{6.15}$$

where r is the gas constant of the mixture dependent on time and space: $r = R/\overline{W}$ where $\overline{W}$ is the mean molecular weight of the mixture:

$$\frac{1}{\overline{W}} = \sum_{k=1}^{N} \frac{Y_k}{W_k} \tag{6.16}$$

The gas constant r and the heat capacities of the gas mixture depend on the local gas composition as:

$$r = \frac{R}{\overline{W}} = \sum_{k=1}^{N} \frac{Y_k}{W_k} R = \sum_{k=1}^{N} Y_k r_k \tag{6.17}$$

$$C_p = \sum_{k=1}^{N} Y_k C_{p,k} \quad \text{and} \quad C_v = \sum_{k=1}^{N} Y_k C_{v,k} \tag{6.18}$$

where $R = 8.3143$ J/mol.K is the universal gas constant. The adiabatic exponent for the mixture is given by $\gamma = C_p/C_v$. Thus, the gas constant, the heat capacities and the adiabatic exponent are no longer constant: they depend on the local gas composition as expressed by the local mass fractions $Y_k(x,t)$.

The temperature is deduced from the the sensible energy, using Eqs. 6.27 and 6.28.

6.3.2 Transport coefficients

In CFD codes for multi-species flows the molecular viscosity μ is often assumed to be independent of the gas composition. However, it depends on the temperature and a power-law or a Sutherland law provides a good estimation of this evolution:

$$\mu = \mu_0 \left(\frac{T}{T_0} \right)^b \quad \text{(Power law)} \quad \mu = c_1 \frac{T^{3/2}}{T + c_2} \frac{T_{ref} + c_2}{T_{ref}^{3/2}} \quad \text{(Sutherland law)} \tag{6.19}$$

with b typically ranging between 0.5 and 1.0 (e.g. $b = 0.76$ for air) or $c_1 = 1.71\ 10^{-5}$ kg/m.s and $c_2 = 110.4$ K for air $T_{ref} = 273$ K.

The heat conduction coefficient λ_q of the gas mixture can then be computed by introducing the molecular Prandtl number of the mixture as:

$$\lambda_q = \frac{\mu C_p}{Pr} \tag{6.20}$$

The Prandtl number Pr is supposed to be constant in time and space and is given in an input file in the AVBP code. For the molecular diffusion coefficients D_k the same approximation can be used in CFD codes. The Schmidt number of species k, Sc_k, is supposed to be constant (in space and time) so that the diffusion coefficient for each species is computed as:

$$D_k = \frac{\mu}{\rho S_{c,k}} \tag{6.21}$$

These thermal and species diffusions act together in a reacting flow. Therefore, an important dimensionless number is defined in combustion to characterize their respective strength: the Lewis number Le which compares the thermal heat diffusivity $D_{th} = \lambda/(\rho C_p)$ to the molecular diffusivity D_k:

$$Le_k = \frac{D_{th}}{D_k} \tag{6.22}$$

6.3.2.a Methane (CH_4) or ethylene (C_2H_4) / air flame transport coefficients

To determine the Schmidt number of species k, Sc_k, to impose in LES and the Prandtl number Pr, a reference flame with a complex transport is computed with Cantera. Cantera is an object-oriented, open source suite of software tools for reacting flow problems involving detailed chemical kinetics, thermodynamics and transport processes. For example, this software can compute one-dimensional laminar premixed flames with detailed chemistry and different transport model. The target fuels for the Cambridge experiment where methane and ethylene. Therefore, a methane/air and ethylene/air laminar flames have been computed with this tool using two different transport models: (1) a complex mixture model called "MIX" where the Schmidt number is not assumed to be constant and (2) the AVBP transport model implemented in Cantera called "AVBP" with constant Schmidt and Prandtl numbers. Typical variation of the Schmidt and Prandtl numbers in the MIX Cantera flame are displayed in Tab. 6.1. They confirm that indeed, $S_{c,k}$ and P_r numbers are almost constant. Their values in the burnt gas were used in AVBP ($S^b_{c,k}$ and P^b_r in Tab. 6.1). The impact of using constant Schmidt and Prandtl numbers can be measured by comparing MIX and AVBP results: adiabatic temperature (left) and laminar flame speed (right) results are displayed in Tab. 6.2 comparing the same ethylene/air flame at $\Phi = 0.85$ computed with these two models (and several kinetic schemes). The two quantities match very well ($T_{ad}^{MIX} = 2239K$, $T_{ad}^{AVBP} = 2245K$, $s_L^{MIX} = 0.557m/s$ and $s_L^{AVBP} = 0.531m/s$) which indicates that assuming constant Schmidt and Prandtl numbers is a valid approximation.

Species	$S^u_{c,k}$	$S^b_{c,k}$
C_2H_4	0.95	0.88
O_2	0.77	0.73
N_2	0.73	0.68
CO_2	0.99	0.94
CO	0.75	0.74
H_2O	0.69	0.54
Prandlt	$P^u_r = 0.713$	$P^b_r = 0.711$

Table 6.1: Schmidt and Prandlt numbers in the unburnt ($S^u_{c,k}$, P^u_r) and burnt ($S^b_{c,k}$, P^b_r) gas from an ethylene/air flame computed by Cantera. Burnt quantities are used in AVBP.

Data	**UCSD**	**MIX**	**AVBP**
s_L (m/s)	0.587	0.557	0.531
T_{ad} (K)	2233	2239	2245

Table 6.2: Adiabatic temperature and laminar flame speed are computed using Cantera ethylene/air flames with MIX and AVBP transport and a two-step mechanism. These results are compared to the detailed mechanism provided by UCSD.

6.3.3 Thermodynamical variables

Species energy and enthalpy are defined in reference to a given temperature T_0. Mass enthalpy of species k, h_k, is the sum of a reference enthalpy at $T = T_0$ and a sensible enthalpy $h_{s,k}$:

$$h_k = \underbrace{h_{s,k}}_{\text{sensible}} + \underbrace{\Delta h^0_{f,k}}_{\text{chemical}} \tag{6.23}$$

The internal energy of species k, $e_k = h_k - RT/W_k$, can also be split into a sensible and a chemical contribution $e_k = e_{s,k} + \Delta h^0_{f,k}$.

The standard reference state used in AVBP is $P_0 = 1$ bar and $T_0 = 0$ K. The sensible mass enthalpies ($h_{s,k}$) and entropies (s_k) for each species are tabulated for 51 values of the temperature (T_i with $i = 1...51$) ranging from 0K to 5000K with a step of 100 K. Therefore these variables can be evaluated by:

$$h_{s,k}(T_i) = \int_{T_0=0K}^{T_i} C_{p,k} dT = \frac{h^m_{s,k}(T_i) - h^m_{s,k}(T_0)}{W_k} \tag{6.24}$$

and:

$$s_k(T_i) = \frac{s^m_k(T_i) - s^m_k(T_0)}{W_k} \tag{6.25}$$

The superscript m corresponds to molar values. The tabulated values for $h_{s,k}(T_i)$ and $s_k(T_i)$ can be found in the JANAF tables (Stull & Prophet, 1971). With this assumption, the sensible energy for each species can be reconstructed using the following expression:

$$e_{s,k}(T_i) = \int_{T_0=0K}^{T_i} C_{v,k} dT = h_{s,k}(T_i) - r_k T_i \tag{6.26}$$

Note that the mass heat capacities at constant pressure $C_{p,k}$ and volume $C_{v,k}$ are supposed constant between T_i and $T_{i+1} = T_i + 100$. They respectively are defined as the slope of

the sensible enthalpy and the slope of the sensible energy ($C_{p,k} = \partial h_{s,k}/\partial T$ and $C_{v,k} = \partial e_{s,k}/\partial T$). The sensible energy henceforth varies continuously with the temperature and is obtained by using a linear interpolation:

$$e_{s,k}(T) = e_{s,k}(T_i) + (T - T_i)\frac{e_{s,k}(T_{i+1}) - e_{s,k}(T_i)}{T_{i+1} - T_i} \qquad \text{for T} \in [\mathrm{T_i}; \mathrm{T_{i+1}}] \tag{6.27}$$

The sensible energy and enthalpy of the mixture may then be expressed as:

$$\rho e_s = \sum_{k=1}^{N} \rho_k e_{s,k} = \rho \sum_{k=1}^{N} Y_k e_{s,k} \tag{6.28}$$

$$\rho h_s = \sum_{k=1}^{N} \rho_k h_{s,k} = \rho \sum_{k=1}^{N} Y_k h_{s,k} \tag{6.29}$$

6.4 Kinetics

The combustion process transforms cold reactants into hot products when a sufficiently high energy is available to activate the reactions. This process can be modeled by a global reaction where a budget between reactants and major products is written. For example, the global reaction of methane oxidation is:

$$CH_4 + 2O_2 \quad \longrightarrow \quad CO_2 + 2H_2O \tag{6.30}$$

Such a global reaction does not describe elementary reactions that occur during the combustion process. Combustion of reactants is in fact a set of reactions involving major and minor species. Generally, N_s species $\mathcal{M}_{kj}$ react through $j = 1, ..., M$ reactions, where N_s and M can be of the order of hundred or thousand:

$$\sum_{k=1}^{N} \nu'_{kj} \mathcal{M}_{kj} \rightleftharpoons \sum_{k=1}^{N} \nu''_{kj} \mathcal{M}_{kj}, \qquad j = 1, ..., M \tag{6.31}$$

The reaction rate of species k, $\dot{\omega}_k$, is the sum of rates $\dot{\omega}_{kj}$ produced by all M reactions:

$$\dot{\omega}_k = \sum_{j=1}^{M} \dot{\omega}_{kj} = W_k \sum_{j=1}^{M} \nu_{kj} \mathcal{Q}_j \tag{6.32}$$

where $\nu_{kj} = \nu''_{kj} - \nu'_{kj}$ and $\mathcal{Q}_j$ is the rate progress of reaction j. The total mass conservation gives:

$$\sum_{k=1}^{N} \dot{\omega}_k = 0 \tag{6.33}$$

The rate $\mathcal{Q}_j$ is written:

$$\mathcal{Q}_j = K_{f,j} \prod_{k=1}^{N} \left(\frac{\rho Y_k}{W_k} \right)^{\nu'_{kj}} - K_{r,j} \prod_{k=1}^{N} \left(\frac{\rho Y_k}{W_k} \right)^{\nu''_{kj}} \tag{6.34}$$

The $K_{f,j}$ and $K_{r,j}$ are the forward and reverse rates of reaction j:

$$K_{f,j} = A_{f,j} \exp\left(-\frac{E_{a,j}}{\mathcal{R}T} \right) \tag{6.35}$$

where $A_{f,j}$ and $E_{a,j}$ are the pre-exponential factor and the activation energy given in an input file. $K_{r,j}$ is deduced from the equilibrium assumption:

$$K_{r,j} = \frac{K_{f,j}}{K_{eq}} \tag{6.36}$$

where K_{eq} is the equilibrium constant defined by:

$$K_{eq} = \left(\frac{p_0}{\mathcal{R}T} \right)^{\sum_{k=1}^{N} \nu_{kj}} \exp\left(\frac{\Delta S_j^0}{\mathcal{R}} - \frac{\Delta H_j^0}{\mathcal{R}T} \right) \tag{6.37}$$

where $p_0 = 1$ bar. ΔH_j^0 and ΔS_j^0 are respectively the enthalpy (sensible + chemical) and the entropy changes for reaction j:

$$\Delta H_j^0 = h_j(T) - h_j(0) = \sum_{k=1}^{N} \nu_{kj} W_k (h_{s,k}(T) + \Delta h_{f,k}^0) \tag{6.38}$$

$$\Delta S_j^0 = \sum_{k=1}^{N} \nu_{kj} W_k s_k(T) \tag{6.39}$$

where $\Delta h_{f,k}^0$ is the mass enthalpy of formation of species k at temperature $T_0 = 0$ K and is given in an input file (molar value). Finally, the heat released by the combustion $\dot{\omega}_T$ in the initial enthalpy equation (Poinsot & Veynante, 2011) is calculated as:

$$\dot{\omega}_T = -\sum_{k=1}^{N} \dot{\omega}_k \Delta h_{f,k}^0 \tag{6.40}$$

6.4.1 Reduced schemes

In real flames, the combustion process involves many species and reactions as already mentioned. For example, the widely used GRI-MECH 3.0 mechanism describes the reaction of methane with air. It consists of 325 reactions that involve 53 species. These full schemes can be used only on very simple configurations (one-dimensional laminar flames for example). In an LES or DNS code, it is nor reasonable neither necessary to transport

such a large number of species (the code must solve one conservation equation for each specie). Moreover some of these reactions can be very fast and could limit the time step drastically. One possible solution consists in reducing the detailed chemistry. Reduced mechanisms are built to reproduce a minimum of flame features. In practice reduced schemes with two reactions are sufficient to reproduce the flame speed, the adiabatic flame temperature and the flame thickness for lean flames. Three criteria are usually sufficient to capture the important kinetic phenomena in most lean premixed turbulent flames.

1. For methane a standard one-step scheme is employed.

$$CH_4 + 2\ O_2 \longrightarrow CO_2 + 2\ H_2O \tag{6.41}$$

(6.42)

2. For ethylene, a two-step mechanism has been developed:

$$C_2H_4 + 2\ O_2 \longrightarrow 2\ CO + 2\ H_2O \tag{6.43}$$

$$CO + \frac{1}{2}\ O_2 \longleftrightarrow CO_2 \tag{6.44}$$

Both schemes account for fuel oxidation through an irreversible reaction at a rate q_1 while a second reaction accounts for the equilibrium between CO and CO_2 with a rate q_2:

$$q_1 = A_1 \left(\frac{\rho Y_F}{W_F}\right)^{n_1^F} \left(\frac{\rho Y_{O_2}}{W_{0_2}}\right)^{n_1^{O_2}} \exp\left(\frac{E_{a,1}}{RT}\right) \tag{6.45}$$

$$q_2 = A_2 \left[\left(\frac{\rho Y_{CO}}{W_{CO}}\right)^{n_2^{CO}} \left(\frac{\rho Y_{O_2}}{W_{0_2}}\right)^{n_2^{O_2}} - \frac{1}{K_e}\left(\frac{\rho Y_{CO_2}}{W_{CO_2}}\right)^{n_2^{CO_2}}\right] \exp\left(\frac{E_{a2}}{RT}\right) \tag{6.46}$$

where K_e is the equilibrium constant for the CO/CO_2 equilibrium and R the perfect-gas constant. While the reduced scheme for methane has already been validated in AVBP (Franzelli *et al.*, 2013), the validation of the C2H4_BFER scheme for ethylene versus a detailed scheme proposed by UCSD is presented in Tab. 6.2 (the Cantera code is used to compare these two chemical schemes). For a one-dimensional planar flame at $P_0 = 101325$ Pa and $T_0 = 300$ K, the reduced scheme reproduces accurately the laminar flame speed s_L and burnt gases adiabatic temperature T_{ad}, for the target equivalence ratio $\Phi = 0.85$ used for the LES simulations of the Dawson's experiment.

6.5 Governing equations for non-reactive LES

As previously discussed, the LES concept consists in applying a spatially localized time independent filter of given size Δ on the Navier-Stokes equations. This filtering introduces a separation between the large (greater than the filter size) and small (smaller than the filter size) scales. This operation also exhibits unclosed terms which must be modeled. These equations and the closure models are presented in this section. It is a close transposition of the AVBP handbook [1].

[1] AVBP handbook: http://www.cerfacs.fr/~avbp/AVBP_V6.X/HANDBOOK/AVBP/HTML2/main.html

6.5.1 The filtering operation

A low-pass (in wavenumber) filter, G_Δ, is applied to the Navier-Stokes equations Eqs. 6.1 - 6.4. Mathematically, it consists of a convolution of any quantity, f, with the filter function G_Δ.

$$\bar{f}(x) = \int f(x')G_\Delta(x - x')dx' \tag{6.47}$$

The resulting filtered quantity, $\bar{f}$, represents the large-scale structures of the flow (*ie.* resolved in the LES) whereas all the structures of size smaller than the filter length, Δ, are contained in the residual field, $f' = f - \bar{f}$. Contrary to RANS averaging, the filtered value of a LES perturbation is not zero: $\overline{f'} \neq 0$ and the double filtered values are not equal to the filtered values in general: $\overline{\overline{f}} \neq \overline{f}$. For variable density ρ, a mass-weighted Favre filtering is introduced according to:

$$\bar{\rho}\widetilde{f}(x) = \int \rho f(x')G_\Delta(x - x')dx' = \overline{\rho f} \tag{6.48}$$

Filtering the instantaneous balance equations (Eqs. 6.1 - 6.4) leads to the following equations:

$$\frac{\partial \overline{\rho}}{\partial t} + \frac{\partial}{\partial x_i}(\overline{\rho}\widetilde{u}_i) = 0 \tag{6.49}$$

$$\frac{\partial \overline{\rho}\widetilde{u}_j}{\partial t} + \frac{\partial}{\partial x_j}(\overline{\rho}\widetilde{u}_i\widetilde{u}_j) = -\frac{\partial}{\partial x_j}(\overline{P}\delta_{ij} - \overline{\tau}_{ij} - \overline{\tau}^t_{ij}) \tag{6.50}$$

$$\frac{\partial \overline{\rho}\widetilde{E}}{\partial t} + \frac{\partial}{\partial x_j}(\overline{\rho}E\widetilde{u}_j) = -\frac{\partial}{\partial x_j}[\overline{u_i(P\delta_{ij} - \tau_{ij})} + \overline{q}_j + \overline{q}^t_j] + \overline{\dot{\omega}}_T + \overline{Q}_r \tag{6.51}$$

$$\frac{\partial \overline{\rho}\widetilde{Y}_k}{\partial t} + \frac{\partial}{\partial x_j}(\overline{\rho}\widetilde{Y}_k\widetilde{u}_j) = -\frac{\partial}{\partial x_j}[\overline{J}_{j,k} + \overline{J}^t_{j,k}] + \overline{\dot{\omega}}_k \tag{6.52}$$

where $\widetilde{u}_j$, $\widetilde{E}$ and $\widetilde{Y}_k$ denote the filtered velocity vector, total energy per unit mass and species mass fractions, respectively. A repeated index implies summation over this index (Einstein's rule of summation). Note also that the index k is reserved for referring to the k^{th} species and does not follow the summation rule.

Writing the vector of the filtered conservative variables as follows: $\overline{\mathbf{w}} = (\bar{\rho}\widetilde{u}, \bar{\rho}\widetilde{v}, \bar{\rho}\widetilde{w}, \bar{\rho}\widetilde{E}, \bar{\rho}\widetilde{Y}_k)$, Eqs. 6.50 - 6.52, can be expressed as:

$$\frac{\partial \overline{\mathbf{w}}}{\partial t} + \nabla \cdot \overline{\mathbf{F}} = \overline{\mathbf{s}} \tag{6.53}$$

where $\overline{\mathbf{s}}$ is the filtered source term and $\overline{\mathbf{F}}$ is the flux tensor which can be divided in three parts:

$$\overline{\mathbf{F}} = \overline{\mathbf{F}}^I + \overline{\mathbf{F}}^V + \overline{\mathbf{F}}^t \tag{6.54}$$

where $\overline{\mathbf{F}}^I$ is the inviscid term, $\overline{\mathbf{F}}^V$ is the viscous term and $\overline{\mathbf{F}}^t$ is the turbulent subgrid-scale term.

6.5.1.a The inviscid term $\overline{\mathbf{F}}^I$

The three spatial components of the inviscid flux tensor are the same as in DNS but based on the filtered quantities:

$$\overline{\mathbf{F}}^I = \begin{pmatrix} \bar{\rho}\widetilde{u}_i\widetilde{u}_j + \overline{P}\delta_{ij} \\ \bar{\rho}\widetilde{E}\widetilde{u}_j + \overline{Pu_j}\delta_{ij} \\ \bar{\rho}_k\widetilde{u}_j \end{pmatrix} \tag{6.55}$$

6.5.1.b The viscous term $\overline{\mathbf{F}}^V$

The components of the viscous flux tensor take the form:

$$\overline{\mathbf{F}}^I = \begin{pmatrix} -\overline{\tau_{ij}} \\ -\left(\overline{u_i\tau_{ij}}\right) + \overline{q_j} \\ \overline{J_{j,k}} \end{pmatrix} \tag{6.56}$$

The filtered diffusion terms are:

- Laminar filtered stress tensor $\overline{\tau_{ij}}$ (for Newtonian fluids)

$$\overline{\tau_{ij}} = \overline{2\mu\left(S_{ij} - \frac{1}{3}\delta_{ij}S_{kk}\right)} \tag{6.57}$$

$$\text{approximation:} \quad \overline{\tau_{ij}} \simeq 2\bar{\mu}\left(\widetilde{S}_{ij} - \frac{1}{3}\delta_{ij}\widetilde{S}_{kk}\right) \tag{6.58}$$

$$\text{with:} \quad \widetilde{S}_{ij} = \frac{1}{2}\left(\frac{\partial\widetilde{u}_j}{\partial x_i} + \frac{\partial\widetilde{u}_i}{\partial x_j}\right) \tag{6.59}$$

$$\text{and:} \quad \bar{\mu} \simeq \mu(\widetilde{T}) \tag{6.60}$$

- Diffusive species flux vector $\overline{J_{i,k}}$

$$\overline{J_{i,k}} = -\overline{\rho\left(D_k\frac{W_k}{\overline{W}}\frac{\partial X_k}{\partial x_i} - Y_kV_i^c\right)} \tag{6.61}$$

$$\text{approximation:} \quad \overline{J_{i,k}} \simeq -\bar{\rho}\left(\overline{D}_k\frac{W_k}{\overline{W}}\frac{\partial\widetilde{X}_k}{\partial x_i} - \widetilde{Y}_k\widetilde{V}_i^c\right) \tag{6.62}$$

$$\text{with:} \quad \widetilde{V}_i^c = \sum_{k=1}^{N}\overline{D}_k\frac{W_k}{\overline{W}}\frac{\partial\widetilde{X}_k}{\partial x_i} \tag{6.63}$$

$$\text{and:} \quad \overline{D}_k \simeq \frac{\bar{\mu}}{\bar{\rho}Sc_k} \tag{6.64}$$

- Filtered heat flux $\overline{q_i}$

$$\overline{q_i} = -\overline{\lambda \frac{\partial T}{\partial x_i}} + \sum_{k=1}^{N} \overline{J_{i,k} h_{s,k}} \tag{6.65}$$

$$\text{approximation:} \quad \overline{q_i} \simeq -\bar{\lambda} \frac{\partial \widetilde{T}}{\partial x_i} + \sum_{k=1}^{N} \overline{J_{i,k}} \widetilde{h}_{s,k} \tag{6.66}$$

$$\text{with:} \quad \bar{\lambda} \simeq \frac{\bar{\mu} \overline{C}_p(\widetilde{T})}{Pr} \tag{6.67}$$

These forms assume that the spatial variations of molecular diffusion fluxes are negligible and can be modeled through simple gradient assumptions.

6.5.1.c The turbulent subgrid-scale term $\overline{\mathbf{F}}^t$

The components of the turbulent subgrid-scale flux take the form:

$$\overline{\mathbf{F}}^I = \begin{pmatrix} -\overline{\tau_{ij}}^t \\ \overline{q_j}^t \\ \overline{J_{j,k}}^t \end{pmatrix} \tag{6.68}$$

As highlighted above, filtering the transport equations leads to a closure problem evidenced by the so called "subgrid-scale" (SGS) turbulent fluxes. For the system to be solved numerically, closures need to be supplied. Details on the closures are:

- The Reynolds tensor $\overline{\tau_{ij}}^t$

$$\overline{\tau_{ij}}^t = -\bar{\rho} \left(\widetilde{u_i u_j} - \widetilde{u}_i \widetilde{u}_j \right) \tag{6.69}$$

$$\text{modeled as (Boussinesq, 1877}a\text{):} \quad \overline{\tau_{ij}}^t = 2\bar{\rho}\nu_t \left(\widetilde{S_{ij}} - \frac{1}{3}\delta_{ij}\widetilde{S_{kk}} \right) \tag{6.70}$$

$$\text{with:} \quad \widetilde{S}_{ij} = \frac{1}{2}\left(\frac{\partial \widetilde{u}_j}{\partial x_i} + \frac{\partial \widetilde{u}_i}{\partial x_j} \right) - \frac{1}{3}\frac{\partial \widetilde{u}_k}{\partial x_k}\delta_{ij} \tag{6.71}$$

In Eq. 6.70, $\overline{\tau_{ij}}^t$ is the SGS tensor, $\widetilde{S_{ij}}$ is the resolved rate tensor and ν_t is the SGS turbulent viscosity. The modeling of ν_t is explained in Sec. 6.5.2.

- The subgrid scale diffusive species flux vector $\overline{J_{j,k}}^t$

$$\overline{J_{i,k}}^t = -\bar{\rho} \left(\widetilde{u_i Y_k} - \widetilde{u}_i \widetilde{Y}_k \right) \tag{6.72}$$

$$\text{modeled as:} \quad \overline{J_{i,k}}^t = -\bar{\rho} \left(D_k^t \frac{W_k}{\overline{W}} \frac{\partial \widetilde{X}_k}{\partial x_i} - \widetilde{Y}_k \widetilde{V}_i^{c,t} \right) \tag{6.73}$$

$$\text{with:} \quad \widetilde{V}_i^{c,t} = \sum_{k=1}^{N} D_k^t \frac{W_k}{\overline{W}} \frac{\partial \widetilde{X}_k}{\partial x_i} \tag{6.74}$$

$$\text{and:} \quad D_k^t = \frac{\nu_t}{Sc_k^t} \tag{6.75}$$

The turbulent Schmidt number $Sc_k^t = 0.6$ is the same for all species. Note also that having one turbulent Schmidt number for all the species does not imply, $\widetilde{V}_i^{c,t} = 0$ because of the $W_k/\overline{W}$ term in Eq. 6.73.

- The subgrid scale heat flux vector $\overline{q_j}^t$

$$\overline{q_i}^t = -\bar{\rho}\left(\widetilde{u_i E} - \widetilde{u}_i \widetilde{E}\right) \tag{6.76}$$

$$\text{modeled as:} \quad \overline{q_i}^t = -\lambda_t \frac{\partial \widetilde{T}}{\partial x_i} + \sum_{k=1}^{N} \overline{J_{i,k}} \widetilde{h}_{s,k} \tag{6.77}$$

$$\text{with:} \quad \lambda_t = \frac{\mu_t \overline{C}_p}{Pr^t} \tag{6.78}$$

The turbulent Schmidt number is fixed at $Pr^t = 0.6$.

6.5.2 Models for the subgrid stress tensor

LES models for the subgrid stress tensor (see Eq. 6.70) are derived on the theoretical ground that the LES filter is spatially and temporally invariant. Variations in the filter size due to non-uniform meshes or moving meshes are not directly accounted for in the LES models. Change of cell topology is only accounted for through the use of the local cell volume, that is $\Delta = V_{cell}^{1/3}$.

The filtered compressible Navier-Stokes equations exhibit SGS tensors and vectors describing the interaction between the non-resolved and resolved motions. Generally, the influence of the SGS on the resolved motion is taken into account by a SGS model based on the introduction of a turbulent viscosity, ν_t (Boussinesq, 1877*b*). Such an approach assumes the effect of the SGS field on the resolved field to be purely dissipative. This hypothesis is essentially valid within the cascade theory of turbulence introduced by Kolmogorov (1941).

LES models for the subgrid stress tensor only differ through the estimation of ν_t. In this document, only the three models used during this PhD. thesis are presented: the Smagorinsky model, the WALE (Wall Adapting Local Eddy-viscosity), and the SIGMA model. For a better understanding of advantages and drawbacks of these different models, desirable properties required for a SGS viscosity model are given:

- **Prop A:** A positive quantity which involves only locally defined velocity gradients
- **Prop B:** A cubic behavior near walls
- **Prop C:** Be zero for any two-component or two-dimensional flows
- **Prop D:** Be zero for axisymmetric or isotropic expansion/contraction

While properties A and B are straightforward, properties C and D should be briefly discussed: 2D turbulence exist and has already been investigated experimentally and numerically. However, its nature is fundamentally different than the usual 3D turbulence because of the absence of vortex-stretching (if a vortex is stretched, matter is pulled towards the rotation axis of the vortex leading to a faster rotation because of the angular momentum conservation). Therefore, it is appropriate to consider **Prop C** to ensure that

the 3D SGS turbulence model phases out in two-dimensional cases. **Prop D** are related to axisymmetric case such as laminar round jet or spherical premixed flames (acting like acoustic monopole, one key acoustic generation which can lead to combustion instabilities) where turbulence effects should not be present.

- The Smagorinsky model

$$\nu_t = (C_S\Delta)^2\sqrt{2\widetilde{S}_{ij}\widetilde{S}_{ij}} \tag{6.79}$$

where Δ denotes the filter characteristic length (cube-root of the cell volume), C_S is the model constant set to 0.18 but can vary between 0.1 and 0.18 depending on the flow configuration. The Smagorinsky model (Smagorinsky, 1963) was developed in the sixties and heavily tested for multiple flow configurations. This closure has the particularity of supplying the right amount of dissipation of kinetic energy in homogeneous isotropic turbulent flows. Locality is however lost and only global quantities are maintained. It is known to be 'too dissipative and transitioning flows are not suited for its use (Sagaut, 2006). Moreover, this formulation is known for not vanishing in near-wall regions and therefore cannot be used when walls are treated as no-slip walls (as performed in this PhD. thesis).

- The WALE model

$$\nu_t = (C_w\Delta)^2\frac{\left(s^d_{ij}s^d_{ij}\right)^{3/2}}{\left(\widetilde{S}_{ij}\widetilde{S}_{ij}\right)^{5/2} + \left(s^d_{ij}s^d_{ij}\right)^{5/4}} \tag{6.80}$$

with:

$$s^d_{ij} = \frac{1}{2}\left(\widetilde{g}^2_{ij} + \widetilde{g}^2_{ji}\right) - \frac{1}{3}\widetilde{g}^2_{kk}\delta_{ij} \tag{6.81}$$

where Δ denotes the filter characteristic length (cube-root of the cell volume), $C_w = 0.4929$ is the model constant and $\tilde{g}_{ij}$ denotes the resolved velocity gradient. The WALE model (Ducros *et al.*, 1998) was developed for wall bounded flows in an attempt to recover the scaling laws of the wall. Similarly to the Smagorinsky model locality is lost and only global quantities are to be trusted.

- The SIGMA model

$$\mathcal{D}_s = \frac{\sigma_3(\sigma_1-\sigma_2)(\sigma_2-\sigma_3)}{\sigma_1^2} \quad \text{and} \quad \nu_t = (C_\sigma\Delta)^2\mathcal{D}_s \tag{6.82}$$

where C_σ is a constant: $C_\sigma = 1.35$.

The Smagorinsky and Wales SGS models have opposite behaviors: while the first one vanishes for pure rotation but not for pure shear, the other one (WALE) has the right near-wall behavior but not for pure rotation situations (**Prop C**). A new operator was

therefore constructed by Nicoud *et al.* (2011) based on singular values (σ_1, σ_2 and σ_3) of a tensor built using resolved velocity gradients ($G = g^t g$). Note that the singular values σ_i have the following near-wall behaviors:

$$\begin{cases} \sigma_1 = O(1) \\ \sigma_2 = O(y) \\ \sigma_3 = O(y^2) \end{cases} \tag{6.83}$$

where y is the normal coordinate to the wall surface and $O(y^p)$ denotes a term of the order of p, i.e. behaving like y^p when the distance to the solid boundary vanishes: $y \to 0$. It results that the SIGMA model behaves correctly near walls: $\nu_t = O(y^3)$.

6.5.3 Numerical schemes

To solve equations presented in Sec. 6.5.1, numerical schemes are needed. The AVBP solver is based on the finite volume method (Hirsch, 2007) with a cell-vertex discretization. Because they are less dissipative than non-centered schemes (up-wind or downwind), centered numerical schemes are implemented in AVBP. All numerical schemes developed in AVBP are presented in (Lamarque, 2007). The two numerical schemes used in this thesis are:

- The Lax-Wendroff (LW) scheme The LW scheme (Lax & Wendroff, 1960) is a finite volume centered scheme. This scheme uses an explicit time integration with a single Runge-Kutta step. Its accuracy in both space and time is of second order. The scheme is quite robust due to a stabilizing diffusive term. Furthermore, it is characterized by low computational cost and has been used during this PhD. thesis for initialization and ignition processor of the cold flow.

- The Two step Taylor-Galerkin 'C' scheme The TTGC scheme (Colin & Rudgyard, 2000) is a finite element centered scheme. Its accuracy in both space and time is of third order (4^{th} on regular grids (Moureau *et al.*, 2005)). It is characterized by very good properties regarding dissipation and dispersion making it well-suited for LES applications involving acoustics as combustion instabilities studied here. However, it is less robust than the LW scheme and is approximately 2.5 more expensive in terms of computational cost. This scheme is normally used after the flow has been stabilized using the *LW* scheme to accurately compute small vortices and acoustic waves.

6.5.4 Artificial viscosity

The numerical discretization methods in AVBP are spatially centered and prone to small-scale oscillations in the vicinity of steep solution variations. This is why it is common practice to add a so-called artificial viscosity (AV) term to the discrete equations, to control these spurious modes (also known as "wiggles"). These AV models are characterized by the "linear preserving" property which leaves unmodified a linear solution on

any type of element. The models are based on a combination of a "shock capturing" term (called 2^{nd} order AV) and a "background dissipation" term (called 4^{th} order AV). In AVBP, adding AV is done in two steps:

- first a sensor detects if AV is necessary, as a function of the flow characteristics,
- then a certain amount of 2^{nd} and 4^{th} AV is applied, depending on the sensor value and on user-defined parameters.

The 2^{nd} order AV acts just like a "classical" viscosity activated only in certain regions of the flow. It smoothes local gradients, and introduces artificial dissipation. The 4^{th} order AV is mainly used to control spurious high-frequency wiggles.

6.6 Combustion modeling

As described in Sec. 6.4, combustion is a process in which reactants are transformed into products. The domain where these transformations take place, called the flame front, is very small. Typically a flame thickness at atmospheric pressure for gasoline/air flames is around 0.1 to 0.5 mm. This raises a problem encountered for Large Eddy Simulation of reactive flows: the thickness δ_L^0 of a flame is generally smaller than the standard mesh size Δ used for LES. In order to resolve the flame front correctly, about 5 to 10 points are needed. This leads to very large grids, out of the capacity of the current calculators for large and complex industrial configurations.

Different models have been proposed to approximate the filtered species reaction rates $\overline{\dot{\omega}}_k$ (see Eq. 6.52) for turbulent premixed combustion using the LES approach. They may be separated into two main categories:

1. **Models assuming an infinitely thin reaction zone:** the turbulent premixed flame is modeled by fresh reactants and burnt products separated by an infinitely thin reaction zone. The local structure of the flame is assumed correspond to a laminar flame for which the inner structure is not affected by turbulence (flamelet assumption). The Bray-Moss-Libby (BML) models (Bray & Moss, 1977), the flame surface density models (Hawkes & Cant, 2000), and G-equation models (Moureau *et al.*, 2009) are some of the most common examples.
2. **Models describing the structure of the reaction zone thickness:** the turbulent premixed flame is characterized by a finite thin reaction zone that could interact with the turbulent flow and often behaves as a stretched laminar flame. Some examples are the Probability Density Function (PDF) models (Dopazo, 1994), the F-TACLES approach (the chemistry is tabulated as a function of a progress variable) developed by EM2C and the artificially Thickened Flame (TF) models (Colin *et al.*, 2000; Légier *et al.*, 2000).

Only the Thickened Flame model has been used in this thesis and therefore is described in more details in this document.

6.6.1 The Thickened Flame model for LES (TFLES)

An attractive solution to propagate a flame on a 'coarse' grid consists in artificially thickening this flame. This idea was first proposed by Butler & O'Rourke (1977). Figure 6.3 presents the concept of this approach. For sufficiently large values of the thickening factor F, the thickened flame front can be resolved explicitly on the grid nodes. Since the reaction rate is still expressed using Arrhenius law, various phenomena can be accounted for without requiring ad-hoc submodels (ignition, flame/wall interactions, heat losses at boundaries).

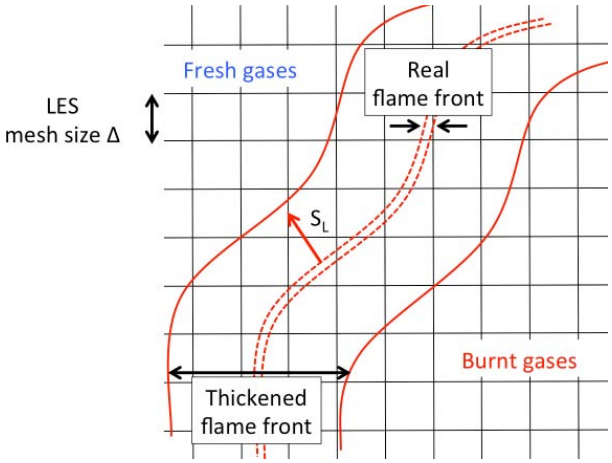

Figure 6.3: Thickened flame approach. The flame is artificially thickened but its flame speed is conserved.

Following simple theories of laminar premixed flames (Williams, 1985; Kuo, 2005), the flame speed s_L and the flame thickness δ_L^0 may be expressed as:

$$s_L \propto \sqrt{D_{th} B} \quad ; \quad \delta_L^0 \propto \frac{D_{th}}{s_L} = \sqrt{\frac{D_{th}}{B}} \tag{6.84}$$

where D_{th} is the thermal diffusivity and B the pre-exponential constant. If the thermal diffusivity is multiplied by a factor F while the pre-exponential constant is divided by F, the flame thickness δ_L^0 is multiplied by a factor F but the flame speed s_L is conserved: the flame propagates at the right speed on the computational domain.

When the flame is thickened by a factor F, the interaction between the flame and the turbulence is modified: the flame becomes less sensitive to turbulent motions and vortex may affect the reaction zone. This interaction is characterized by the Damköhler number D_a which compares turbulent τ_t to chemical τ_c time scales (for large values of D_a, turbulence is not able to affect the inner flame structure which remains close to a laminar flame wrinkled by turbulence motions):

$$D_a = \frac{\tau_t}{\tau_c} = \frac{l_t}{u'} \frac{s_L}{\delta_L^0} \tag{6.85}$$

It is straightforward to show that increasing the flame thickness by a factor F decreases the D_a number by the same factor F ($D_a^{thick} = D_a/F$). This point has been investigated using DNS by Angelberger *et al.* (1998) and Colin *et al.* (2000) (see Figure 6.4). To account for this unwanted effect, an efficiency function $\mathcal{E}_f$, corresponding to a subgrid scale wrinkling factor has been derived. This efficiency function depends on velocity (u'/s_L) and length scale ($\Delta/F\delta_L^0$) ratios.

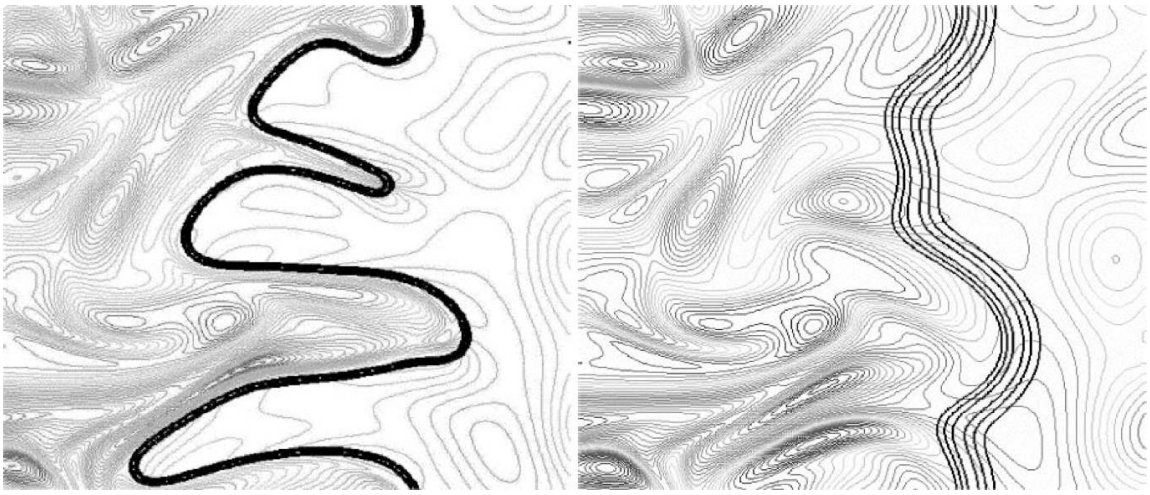

Figure 6.4: DNS of flame turbulence interactions. Reaction rate and vorticity fields are superimposed. Left: Reference flame ; Right: flame artificially thickened by a factor $F = 5$ (Poinsot & Veynante, 2011).

In practice, the thickened flame approach is implemented by changing the thermal diffusivity and the reaction rate according to:

$$\begin{array}{rccccc} \text{Diffusivity:} & D_{th} & \Rightarrow & FD_{th} & \Rightarrow & \mathcal{E}_f F D_{th} \\ \text{Pre-exponential constant:} & B & \Rightarrow & B/F & \Rightarrow & \mathcal{E}_f B/F \\ & & \text{thickening} & & \text{wrinkling} & \end{array}$$

According to Eq. 6.84, the flame speed s_L and the flame thickness δ_L^0 become respectively:

$$s_T = \mathcal{E}_f s_L \quad ; \quad \delta_T = F\delta_L^0 \tag{6.86}$$

In this thesis, two different efficiency functions $\mathcal{E}_f$ valid when equilibrium between the turbulent motions and the flame surface is reached, have been used and are briefly described:

- **Colin model:** Colin *et al.* (2000) have proposed an efficiency function $\mathcal{E}_{f,colin}$ which compares the flame wrinkling with and without thickening, called the wrinkling factor Ξ:

$$\Xi(\delta_l^0) = 1 + \alpha\Gamma\left(\frac{\delta_\Delta}{\delta_L^0}, \frac{u'_\Delta}{s_L^0}\right)\frac{u'_\Delta}{s_L^0} \tag{6.87}$$

where α is a constant and Γ is a function taking into account the subgrid strain rate depending on the fluctuating subgrid velocity u'_Δ and the filter size Δ.
The turbulent flame velocity is therefore obtained in the LES as a function of this efficiency function:

$$\frac{s_T}{s_L} = \frac{\Xi(F\delta_l^0)}{\Xi(\delta_l^0)} = \mathcal{E}_{f,colin} \tag{6.88}$$

Finally, this combustion model is closed by approximating the subgrid scale turbulent velocity u'_Δ with an operator based on the rotational of he velocity field to remove the dilatation part of the velocity and by estimating the constant α using HIT (Homogeneous Isotropic Turbulence) simulations (Angelberger *et al.*, 1998).

- **Charlette and Meneveau model:** Charlette *et al.* (2002) have proposed a power-law model for the wrinkling factor which extendes the Colin model proposed in Eq. 6.87:

$$\Xi(\delta_l^0) = \left(1 + \min\left[\max\left(\frac{\delta_\Delta}{\delta_l^0} - 1\right), \Gamma\left(\frac{\delta_\Delta}{\delta_L^0}, \frac{u'_\Delta}{s_L^0}, Re_\Delta\right)\frac{u'_\Delta}{s_L^0}\right]\right)^\beta \tag{6.89}$$

where the efficiency function Γ describes the ability of vortices to effectively wrinkle the flame front and is therefore related to the fractal dimension of the flame front, β is the model parameter and $Re_\Delta = \frac{u'_\Delta \delta_\Delta}{\nu}$ is the subgrid scale turbulent Reynolds number (ν being the fresh gas kinematic viscosity).

This TFLES model has been first developed for perfectly premixed combustion. But applying a uniform thickening in the whole domain accelerates diffusion in non reactive zones, where thickening is not necessary. In other words, the TF model can remain unchanged in the flame zone but must be adapted outside the flame region. So a dynamic thickening procedure (Légier *et al.*, 2000) (called D-TFLES) depending on the flame position and the local resolution has been developed and is therefore preferred.

The thickening factor F is not a constant any more but it goes to F_{max} in flame zones and decreases to unity in non reactive zones. This is obtained by writing:

$$F = F_{max}\mathcal{S} \tag{6.90}$$

with:

$$F_{max} = \frac{N_c}{\Delta}\delta_L^0 \tag{6.91}$$

N_c being the number of cells used to resolve the flame front (typically $N_c = 5$ guarantees a good behavior). $\mathcal{S}$ is a sensor depending on the local temperature and mass fractions:

$$\mathcal{S} = \tanh\left(\beta'\frac{\Omega}{\Omega_0}\right) \tag{6.92}$$

where β' is a constant equal to 500, Ω is a sensor function detecting the presence of a reaction front and Ω_0 corresponds to its maximum value. One possible method to construct Ω is to use the kinetic parameters of the fuel breakdown reaction:

$$\Omega = {Y_F}^{n_F}{Y_O}^{n_O}\exp\left(-\Gamma\frac{E_a}{RT}\right) \tag{6.93}$$

Ω_0 can be found running a 1D premixed non-thickened flame and measuring Ω_0 on it. Γ is used to start the thickening before the reaction, that is why $\Gamma < 1$ (usually $\Gamma = 0.5$).

Note that TFLES is not a "filtered" model: equations are first thickened so that LES filtering is not needed. In that sense, the "thickening" of species and temperature used in TFLES is not following the "filtering" operator used for density and velocity. Constructing thickened flames by rigorously filtering all equations is the path followed for example by the EM2C group in the FTACLES series of models (Fiorina *et al.*, 2010; Auzillon *et al.*, 2012). On the long term, FTACLES type models are promising methods but they were not tested here because this work focused on thermo-acoustics and not turbulent combustion.

The main advantages of the TFLES model are its simplicity and its performances for premixed and stratified flames. It has been used successfully in multiple configurations (Colin *et al.*, 2000; Légier *et al.*, 2002; Selle *et al.*, 2004*a*; Wolf *et al.*, 2010; Enaux *et al.*, 2011) and is also integrated now in commercial softwares such as Fluent or Charles (from Cascade Technologies). The effect of the combustion models on FTF results will be characterized by a sensitivity analysis developed in Chapter 7 by changing the mesh refinement (computations are performed on a coarse mesh using 5 millions cells and a fine mesh with 30 millions cells) and efficiency functions (Colin and Charlette efficiency functions).

6.7 Few words about the AVBP code

Historically, the AVBP code was started at CERFACS in January 1993 as an initiative of Michael Rudgyard and Thilo Schönfeld. The aim of this project was to build an efficient code handling unstructured grids of any cell type. Nowadays, AVBP is a parallel CFD code that solves the laminar and turbulent compressible reactive (or non-reactive) Navier-Stokes equations in two and three space dimensions[2]. It is also the baseline code of the ERC (European Research Council) advanced grant won by IMFT in 2013 on thermoacoustics (http://intecocis.inp-toulouse.fr).

The important development of the physical models done at CERFACS is completed by academics studies carried out at the IFP Energies Nouvelles, the EM2C lab of Ecole Centrale Paris (ECP) and the Institut de Mécanique des Fluides de Toulouse (IMFT). The ownership of AVBP is shared with IFP-Energies Nouvelles (IFP-EN), following an agreement of joint code development oriented towards piston engine applications. Important links with industry have been established with Safran Group (Snecma, Snecma DMS, Herakles, Turbomeca), Air Liquide, Gaz de France as well as with Alstom, Ansaldo, Honeywell and Siemens Power Generation.

[2]More details on AVBP here: http://www.cerfacs.fr/4-26334-The-AVBP-code.php.

Chapter 7

Sensitivity of FTF for turbulent swirled flames and impact on the stability of azimuthal modes

Contents

7.1 Introduction 166

7.2 Target configuration: annular combustor of Cambridge (Worth & Dawson, 2013*b*) 167

7.3 Numerical models 169

7.3.1 Large Eddy Simulations 169

7.3.2 Helmholtz simulations of the full annular combustor 174

7.4 Unforced flow fields 175

7.5 Phase-averaged forced flow fields 176

7.6 Rayleigh criterion 178

7.7 FTF sensitivity study 181

7.8 Effect of FTF uncertainties on stability of azimuthal modes 182

7.9 Conclusion 184

Part I has shown the first-order importance of FTF (Flame Transfer Function) on thermoacoustic codes results. We now address the problem of FTF prediction using LES. This chapter describes a preliminary numerical study of azimuthal unstable modes in the annular combustor of Cambridge before computing the full 360° *configuration. LES is used to compute a Flame Transfer Function (FTF) and a Helmholtz solver to predict the overall stability of the combustor. FTF quantifies the interaction between acoustics and the turbulent swirled flames. They must be known with precision because instabilities are very sensitive to small changes (see Chapter 5). The effects of azimuthal confinement (corresponding to the annular combustor equipped with* 12 *or* 18 *burners), thermal boundary conditions and fuel type (methane or ethylene) on FTFs are simulated here using LES of a single* 20 *degree (*$N = 18$*) or* 30 *degree (*$N = 12$*) sector. A double-sector LES is also computed to investigate flame / flame interactions. These LES-based FTFs are then used as inputs for a Helmholtz solver and results show that 1) subgrid-scale LES models lead to marginal effects on the Flame Transfer Function while 2) azimuthal confinement, thermal conditions and fuel type strongly affect the flame response to acoustics and therefore control the stability of the azimuthal mode. Computations reveal that the annular experiment performed with methane should be stable while ethylene should lead to azimuthal unstable modes as observed experimentally. From this sensitivity analysis, an operating point (ethylene, adiabatic,* $N = 18$ *burners) is extracted and will be computed using a full annular* 360° *configuration in the next chapter.*

7.1 Introduction

Studying experimentally an unsteady combustion is a daunting task and most experimentalists have to choose between providing very detailed space and time resolved measurements (velocity, species and temperature fields like for example in the Preccinsta burner (Franzelli *et al.*, 2013; Meier *et al.*, 2007)) or performing flame transfer function measurements. Therefore in practice, when FTFs measurements are available, almost no other experimental data is usually given to check the LES quality. Moreover, measuring any physical quantities in a self-excited combustor becomes an insuperable task since probes must cope with an extreme environment facing strong pressure oscillations. Here the Cambridge rig of Worth & Dawson (2013*b*) was used to compute FTF and predict mode stability. This rig belongs to the second category: information on thermo-acoustics is available but not much more so that the few experimental data available (no mean velocity profiles, FDF or FTF measurements etc.) raise the question of quality and accuracy of the full 360° LES which will be performed in the next chapter. Observations from Worth & Dawson (2013*b*,*a*) on the stability and frequencies of the experimental combustor in multiple conditions (fuels, wall materials, number of burners etc.) can be used to assess the validity of the LES and its underlying models (turbulence, combustion, chemistry etc.). Therefore, this chapter intends to first evaluate the robustness of the LES strategy to capture the flame/acoustic interaction and consequently to predict the

stability of the annular configuration by computing one or two sectors only.

Because of their extreme costs, computations of full 360° configurations are still out of reach today to study effects of number of burners N, mesh refinements, turbulence and combustion models as well as operating points on the predicted azimuthal mode. In this chapter, a reduced strategy is used: 1) A Flame Transfer Function (FTF, Crocco, 1951) or Flame Describing Functions (FDF, Noiray *et al.*, 2008) can be evaluated numerically to link the flame response to acoustics. To do so, only one sector with periodic and non-reflecting boundary conditions is computed using LES since capturing a self-excited azimuthal mode is not required (Giauque *et al.*, 2005; Kaess *et al.*, 2008) to obtain FTF or FDF. 2) The acoustic/flame model (FTF) is then introduced as a source term in a full annular acoustic solver, much cheaper than LES, to study the azimuthal acoustic mode in the complete 360° configuration. Although successful in determining the stability of real burners (Nicoud *et al.*, 2007) such coupled approaches are known to be sensitive to multiple parameters (Duchaine *et al.*, 2011). This last question is also addressed in this chapter by evaluating which parameters control the flame/acoustics interactions measured by the FTF models. Finally, this chapter addresses two crucial points:

1) Provide LES best practices and guidelines for turbulence models, combustion models and thermal boundary conditions to be followed when computing the whole 360° configuration of Cambridge.
2) Choose the operating point to be used to compute the full annular rig and verify its consistency with experimental observations performed by Worth & Dawson (2013*b*,*a*).

First, Section 7.2 describes the annular rig of Cambridge. In Section 7.3, the numerical strategy and the various cases used to evaluate the FTF (Section 10.2.2) and stability (Section 7.3.2) are defined. Results on mean and phase-averaged flow fields for unforced and forced cases are discussed and compared to experiment in Sections 7.4 and 7.5. Section 7.7 focuses on the FTF sensitivity to various LES sub models as well as key phenomena (azimuthal confinement, thermal conditions and fuel type) affecting the flow dynamics and flame shape as observed in previous sections. Finally, Section 7.8 gives the stability map of the 360° configuration. The impact of azimuthal confinement, thermal conditions and fuels on the stability is assessed: the annular rig is found to be stable when using methane while ethylene leads to azimuthal instabilities as observed in the annular experiment (Worth & Dawson, 2013*b*,*a*).

7.2 Target configuration: annular combustor of Cambridge (Worth & Dawson, 2013*b*)

The target experiment is the annular combustor of Cambridge studied by Worth & Dawson (2013*b*) (Fig. 7.1) The stainless steel rig can include $N = 12$, 15, or 18 equally spaced flames around a circumferential diameter of 170 mm which modifies the flame-flame interactions as shown in Fig. 7.2: for $N = 12$ burners, the distance between burners is large and flames are isolated but for $N = 18$ burners, the distance between burners is reduced leading to a strong flame merging between neighboring sectors. Note also that

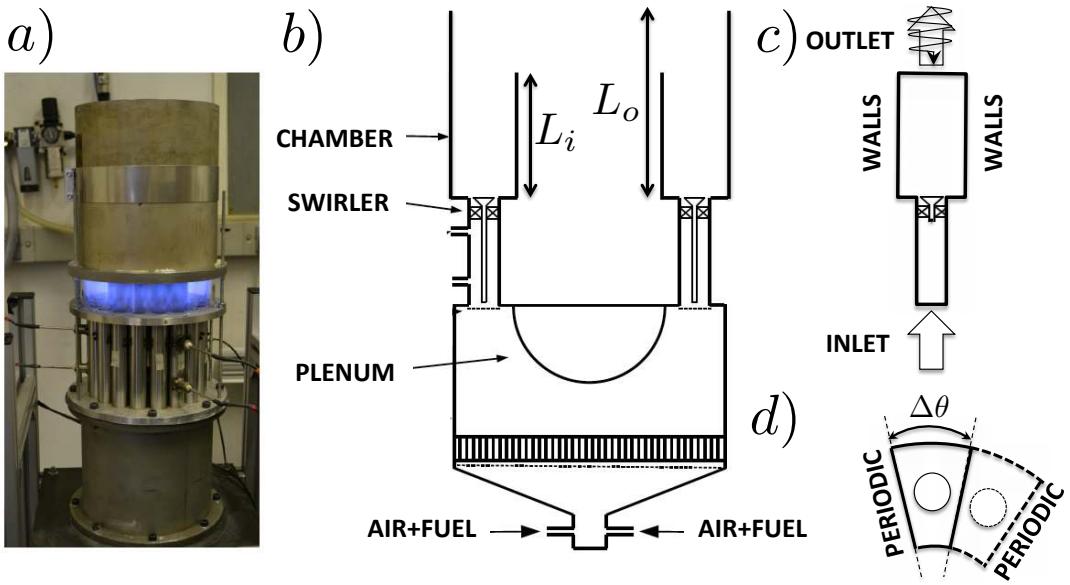

Figure 7.1: Photograph (a) and schematic (b) of the annular experiment with $L_i = 130\ mm$ and $L_o = 300\ mm$ complemented by a longitudinal (c) and a transverse (d) cut of the single (——) and double (- - -) sector computation domain.

isolated and merged flames react differently to heat-loss: the outer shear branch of the V-flame is weaker and even disappears for isolated flames, but no heat-loss effect is observed when flame merging occurs. Premixed reactants are supplied by a plenum which includes grids and flow straighteners for flow conditioning and acoustic damping. For all configurations, mass flow controllers are used to maintain a constant bulk velocity of $U = 18\ m.s^{-1}$ at the exit of each bluff body. This ensures that any change in the flame structure and dynamics is the result of azimuthal confinement (flame spacing). The rig is instrumented with microphones to characterize the instability modes and a high-speed intensified camera is used to measure the OH^* chemiluminescence of the whole annulus.

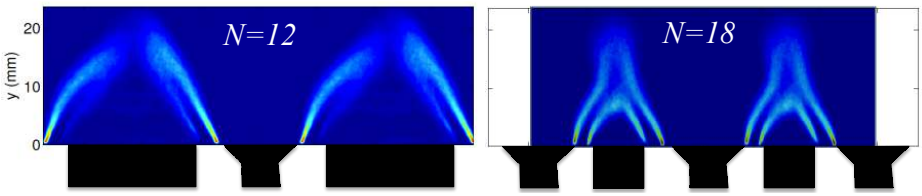

Figure 7.2: Flame visualization of two neighboring flames in the experiment for $N = 12$ burners (left) and $N = 18$ burners (right).

To find a set of conditions that give rise to self-excited azimuthal modes, the inner (L_i) and outer (L_o) lengths of the combustor walls, azimuthal confinement, and two fuel types (CH_4 and C_2H_4) were varied in the experiment (Worth & Dawson, 2013*b*,*a*): strong self-excited azimuthal modes at the frequency $f = 1800\ Hz$ (Fig. 7.3) only occurred for C_2H_4-air mixtures and when different inner and outer tube lengths $L_i = 130$ mm and $L_o = 300$ mm were used. Bourgouin *et al.* (2013) also found that L_i and L_o must

be different to excite azimuthal modes. The occurrence of self-excited azimuthal modes did not depend on azimuthal confinement but the limit-cycle amplitude and the flame structure did. Only longitudinal modes were observed for CH_4-air mixtures.

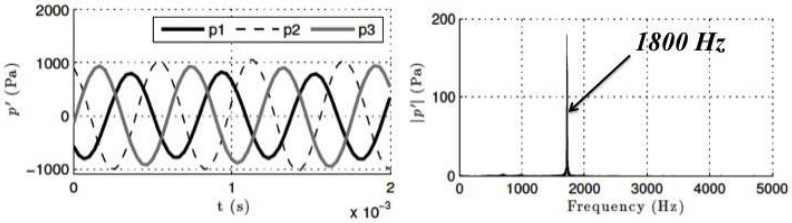

Figure 7.3: Acoustic pressure oscillations varying with time (left) and its Fourier transform (right) showing a strong instabilities at $f = 1800\ Hz$ corresponding to an azimuthal mode.

7.3 Numerical models

7.3.1 Large Eddy Simulations

Large Eddy Simulation (LES) of compressible flow (detailed in Chapter 6) is widely recognized as an accurate method (Poinsot & Veynante, 2011) to study combustion instabilities in complex configurations (Wolf *et al.*, 2012; Sengissen *et al.*, 2007; Fureby, 2010; Kuenne *et al.*, 2011) but the impact of subgrid scale models on LES results for instabilities is rarely discussed. As shown by the UQ study of Chapter 5, any uncertainty on FTF input data will have a strong effect on stability predictions. Quantifying uncertainties due to LES on FTF results is a mandatory step. This includes effects of the subgrid models, combustion models, chemistry and grid refinement on FTF outputs (n, τ). The effect of these numerical parameters will be compared to the effect of physical parameters such as the fuel, potential heat losses at walls or the number of sectors, hoping that the physical parameters introduce larger changes in n and τ than the numerical parameters do.

To study the impact of models on FTF computations, AVBP is used in this chapter to solve the filtered multi-species 3D Navier-Stokes equations with realistic thermochemistry on unstructured meshes (Schønfeld & Poinsot, 1999; Roux *et al.*, 2005). Numerics is based on a two-step Taylor-Galerkin finite element scheme of third-order in space and time (TTGC, Moureau *et al.*, 2005) to accurately propagate acoustic waves. Boundary conditions use the NSCBC approach (Poinsot *et al.*, 1992) and ensure non-reflecting conditions (Selle *et al.*, 2004*b*) as well as the proper introduction of acoustic waves in the LES domain for FTF computations. This computational domain corresponds to one single sector of the annular combustor of Cambridge equipped with $N = 18$ burners (Fig. 7.4). A swirler with 6 blades mounted with a bluff-body is installed at the burner/chamber junction (Fig. 7.5) to stabilize the flame.

Since the plenum contains dampers and grids, this cavity has been removed from the computational domain and therefore the inlet of the LES domain is located at the burner inlet, assuming that no aerodynamic perturbations from the plenum (e.g. vortex shedding due to the inflow jet impinging the plenum curbed walls) can affect the downstream

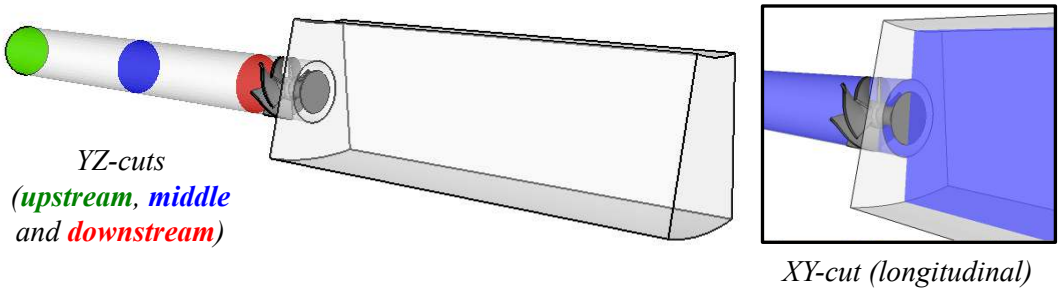

Figure 7.4: 3D view of the SHORT configuration (no plenum) corresponding to one sector of the annular combustor equipped with $N = 18$ burners. The upstream (green), middle (blue) and downstream (red) transverse YZ-cuts in the burner (left) and the longitudinal XY-cut (blue, right) are also displayed.

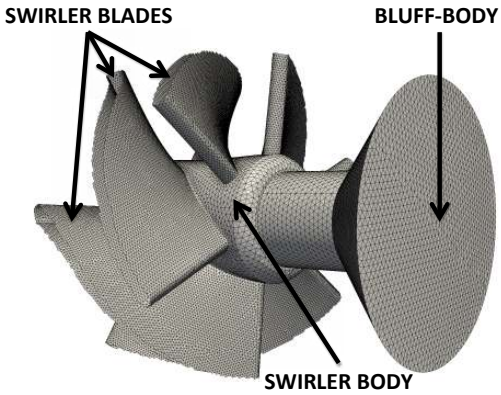

Figure 7.5: 3D view of the swirler and the associated surface mesh.

dynamics of the system. To validate this choice, two different non-reactive stabilized (i.e. no acoustic forcing) configurations with (called LONG) and without (called SHORT) plenum cavity have been computed by LES to analyze the effect of the plenum removal on the system dynamics. Especially, the velocity profile at the burner inlet is resolved in the LONG case while it is imposed in the SHORT case with a Poiseuille's profile: a comparison between the mean velocity profiles and spectra is required to ensure that no perturbation coming from the plenum can modify the mean flow topology (recirculation zones, jet opening at the swirler exit etc.) or excite the flame dynamics at 1800 Hz.

First, pressure (not shown here) and axial velocity signals in the burner and the chamber are analyzed in Fig. 7.6 and show that only the broadband noise, but not aerodynamics oscillations at specific frequencies, is affected by the plenum. Peaks observed in the pressure/velocity spectra come from aerodynamics perturbations generated by the swirlers. This validation is comforted by the mean (and RMS, not shown here) flow field in the chamber and at several longitudinal positions in the burners. This study highlights no particular differences between the LONG (top) and SHORT (bottom) cases (Fig. 7.7). This is due to the particular curved shape of the plenum/burner junction which reduces aerodynamics instabilities and lets acoustic waves leave the burners toward the plenum without reflections: experimental and numerical reflection coefficients at the plenum/burners junction are close to $R = 0.1$, i.e. the junction is almost non-reflecting.

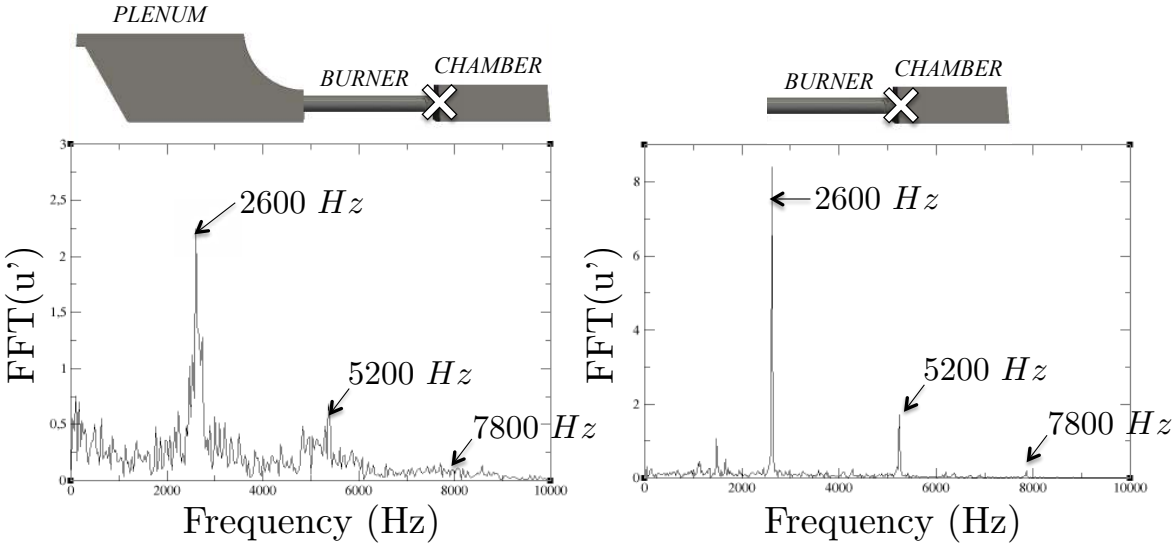

Figure 7.6: Fluctuation axial velocity u' spectra in the single sector configuration of the annular chamber for a stabilized non-reactive case with (LONG, left) and without (SHORT, right) plenum cavity. Only the broadband noise, but not the aerodynamics peaks, is affected by the plenum removal. The probe is located at the burner/chamber junction (white cross).

Moreover, aerodynamics noise and heterogeneities generated in the plenum are phased out in the long burners as observed in Fig. 7.7.

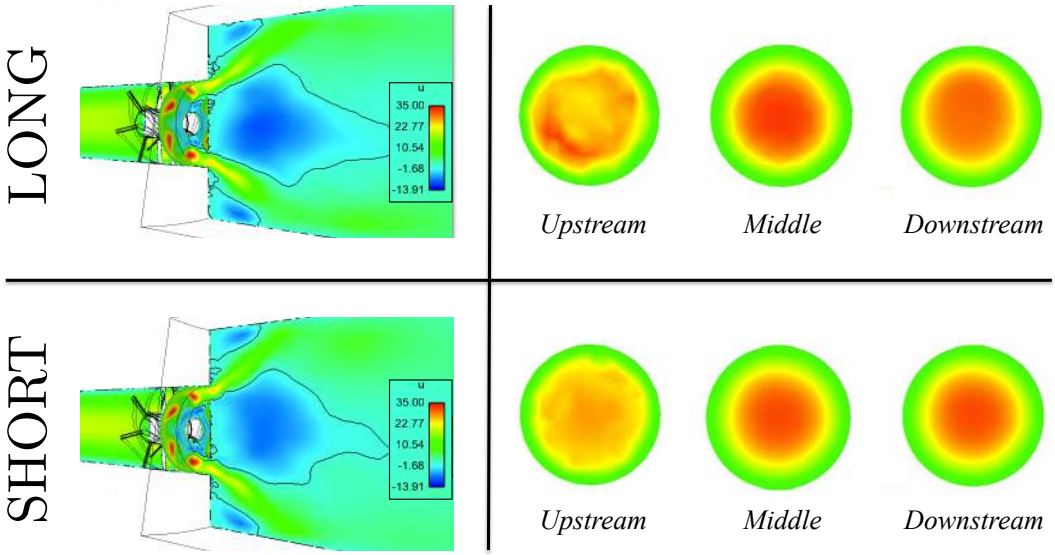

Figure 7.7: Mean axial flow field in the chamber (left) and at several positions in the burners described in Fig. 7.4 (right) for the LONG (top) and SHORT (bottom) configurations.

Finally, all computational domains computed in this thesis have no plenum but include the complete burner with an axial swirler composed of six blades mounted on a bluff-body (Figs. 7.5 and 7.8). Although FTF estimations can be obtained from an acoustically isolated single sector of a real configuration, flow confinement is known to play a role on

flame shape and stability. The effect of confinement and flame/flame interactions was tested here by comparing single and double sector LES (Fig. 7.1, d).

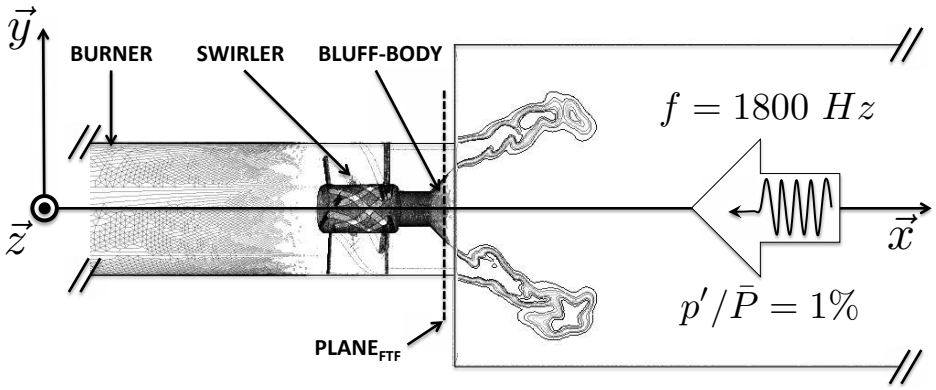

Figure 7.8: XY-cut of the single-sector configuration with iso-contours of heat release. Acoustic waves, needed for FTF evaluation in the LES, are introduced by pulsating the outlet pressure.

The sensitivity of FTF predictions to different sub-grid stress models is tested using the classical Dynamics Smagorinsky model (Smagorinsky, 1963) and both Wale (Nicoud & Ducros, 1999) and Sigma (Nicoud *et al.*, 2011) models (Section 6.5.2). Turbulent-flame interactions are addressed using the dynamic Thickened Flame (TF) approach with two different efficiency functions as a performance test: the Colin model (Colin *et al.*, 2000) and the Charlette-Meneveau model (Charlette *et al.*, 2002) described in Section 6.6.1. These combustion models are closed by approximating the subgrid scale turbulent velocity u'_Δ with an operator based on the rotational of the velocity field to remove the dilatation part of the velocity.

Since the overall number of injectors N also varies, different angles, $\Delta\theta = 30°$ or $20°$, are considered for the single-sector cases, corresponding respectively to the annular rig equipped with $N = 12$ or $N = 18$ burners (Fig. 7.1). All meshes are fully unstructured and contain 4.2 millions cells (for the case $\Delta\theta = 20°$) or 5.5 million cells (for $\Delta\theta = 30°$) per sector for the coarse cases while the refined case contains 31 million cells. This results in typical thickening factors of 3 to 5 in the flame zone to guarantee $5 - 10$ points in the flame. Cells lengths are typically $80\mu m$ near swirler walls and $150\mu m$ in the swirler passages.

Axial acoustic forcing is performed in the LES to compute FTFs since the main mechanism leading to azimuthal combustion instabilities is the modulation of the axial mass flow rate through the injectors. Transverse acoustic forcing by strong transverse velocity fluctuations (O'Connor & T.Lieuwen, 2012*c*; Lespinasse *et al.*, 2013) is not considered here since it occurs only for flames located at a pressure node which do not contribute to the stability of the system[1]. The forcing frequency corresponds to the azimuthal mode observed experimentally (Worth & Dawson, 2013*b*) ($f \simeq 1800\ Hz$) and is introduced in the LES by pulsating (with the NSCBC approach) the outlet ingoing acoustic wave of the

[1]The Rayleigh criterion is proportional to $\|\hat{p}\|\|\hat{q}\|$ thus flames at pressure nodes ($\|\hat{p}\| = 0$) lead to a null Rayleigh term and therefore do not contribute to the stability of the system.

sector (Figs. 7.1 and 7.8). No data on the forcing amplitude is reported since the experiment is self-excited ($p'/\bar{p} \simeq 1\%$): in the LES, various low amplitudes (from $p'/\bar{p} = 0.1\%$ to 1%) of the forcing wave have been tested and no impact on the FTF was observed. FTFs are constructed by recording the global heat release rate $\dot{Q}_i'(t)$ and the reference acoustic velocity $u'_{REF}(t)$ (Crocco, 1951). This velocity is obtained by averaging the axial fluctuating velocity over a plane ($\text{Plane}_{\text{FTF}}$ in Fig. 7.8).

Based on the experiments (Worth & Dawson, 2013*b*), a perfectly premixed air-fuel mixture (methane or ethylene) at equivalence ratio $\phi = 0.85$ is injected in the inlet (plenum/burner section). Worth & Dawson (2013*b*) mention that using ethylene (C_2H_4) leads to azimuthal instabilities while only longitudinal modes appear with methane (CH_4). These two fuels are investigated here with LES. Reaction rates are modeled with reduced kinetic schemes, which have been proved to accurately reproduce low frequency flame dynamics (Kedia *et al.*, 2011): 1 reaction, 4 species for CH_4 and 2 reactions, 6 species for C_2H_4. Adiabatic temperatures and laminar flame speeds have been compared to GRIMECH (Frenklach *et al.*, 1995) for methane and UCSD full schemes (UCSD, 2013) for ethylene (Lecocq *et al.*, 2013; Franzelli *et al.*, 2010; Goodwin, 2009).

Thermal effects also modify FTFs (Duchaine *et al.*, 2011; Tay-Wo-Chong & Polifke, 2012; Mejia *et al.*, 2014): here, adiabatic as well as heat-loss formulations were applied on the chamber walls. For the heat loss formulation, the heat flux imposed on a wall is locally expressed as $\Phi = (T - T_\infty)/R_w$ where the temperature T_∞ is set to 600 K and the thermal resistance is $R_w = 10^{-4}(Km^2)/W$. For these values, the chamber walls typically reach 1000 K.

For all computed cases (Table 7.1), as in the experiment, the mean axial velocity at the burner/chamber junction is conserved: 18 $m.s^{-1}$.

	CASE	COMB.	TURB.	N	MESH	THERM.	$\Delta\theta$	FUEL
	REF	Charlette	Wale	1	Coarse	Adiabatic	20	CH_4
Numerical	**COLIN**	***Colin***	Wale	1	Coarse	Adiabatic	20	CH_4
	SMAGO	Charlette	***Smago***	1	Coarse	Adiabatic	20	CH_4
	SIGMA	Charlette	***Sigma***	1	Coarse	Adiabatic	20	CH_4
	DOUBLE	Charlette	Wale	***2***	Coarse	Adiabatic	20	CH_4
	FINE	Charlette	Wale	1	***Fine***	Adiabatic	20	CH_4
Physical	**CH4-HL-20**	Charlette	Wale	1	Coarse	***Heat-loss***	20	CH_4
	C2H4-ADIA-20	Charlette	Wale	1	Coarse	Adiabatic	20	$\boldsymbol{C_2H_4}$
	CH4-ADIA-30	Charlette	Wale	1	Coarse	Adiabatic	***30***	CH_4
	CH4-HL-30	Charlette	Wale	1	Coarse	***Heat-loss***	***30***	CH_4
	C2H4-ADIA-30	Charlette	Wale	1	Coarse	Adiabatic	***30***	$\boldsymbol{C_2H_4}$

Table 7.1: LES simulations performed to investigate the FTF sensitivity to numerical and physical parameters.

7.3.2 Helmholtz simulations of the full annular combustor

In addition to evaluating uncertainties on input data such as (n, τ), it is also interesting to actually see what these changes lead to in terms of modes when they are injected in a Helmholtz solver. In the UQ study of Chapter 5, ATACAMAC was used to optimize speed but here we will favor precision and run a full 3D Helmholtz solver: the 3D acoustic solver called AVSP (Nicoud *et al.*, 2007) will be used to predict the effect of the FTF on the stability of the azimuthal mode observed experimentally at $f \simeq 1800\ Hz$. AVSP solves the eigenvalues problem issued from a discretization on unstructured meshes (with 3.6 millions cells) of the wave equation where the source term due to combustion is expressed using FTFs (Crocco, 1951). The local reaction term $\widehat{\dot{Q}_i'}$ is expressed for each burner i as:

$$\widehat{\dot{Q}_i'} = n_{u,i}\, e^{j\omega\tau_i}\, \widehat{u'}(\mathbf{x}_{ref,i}) \tag{7.1}$$

where $\widehat{u'}(\mathbf{x}_{ref,i})$ is the Fourier transform of the axial acoustic velocity component at the location $\mathbf{x}_{ref,i}$. The interaction index $n_{u,i}$ is constant for each sector i in the flame zone (Fig. 7.9) and its value is chosen to recover the global value of unsteady heat release (Nicoud *et al.*, 2007) computed by LES. It is set to zero outside of the flame zone.

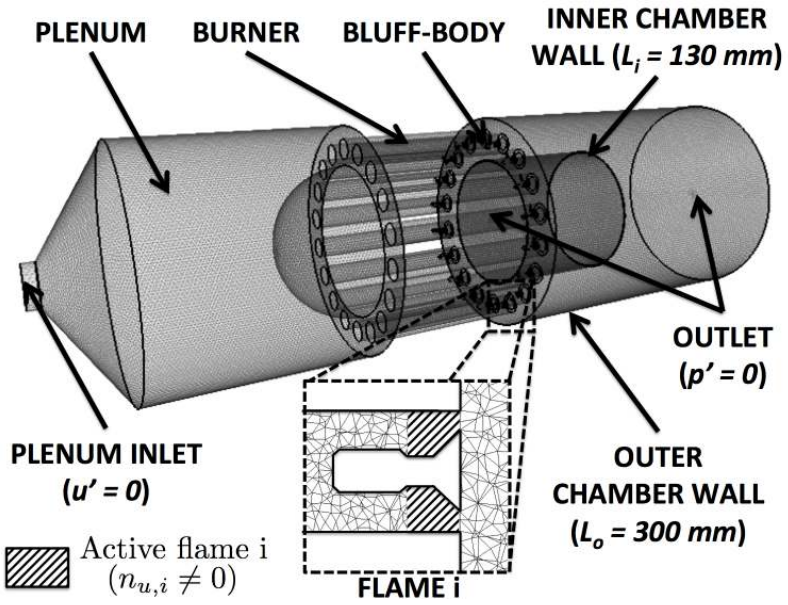

Figure 7.9: 3D view to the 360° acoustic domain with $N = 18$ burners and zoom on the i^{th} flame zone.

The acoustic domain computed with AVSP is the 360° configuration with $N = 12$ or 18 burners connected to the plenum (Fig. 7.9). Different lengths are used for the inner and outer chamber walls ($L_i = 130$ mm and $L_o = 300\ mm$) (Worth & Dawson, 2013*a*; Bourgouin *et al.*, 2013). Infinite impedances (corresponding to $u' = 0$) are applied on walls or plenum inlet and a pressure node ($p' = 0$) is applied at the outlet. Mean density and sound speed are extracted from LES simulations of the single-sector and replicated azimuthally for all sectors.

7.4 Unforced flow fields

A first indication of the effects of parameter changes on LES results is provided by unforced reactive LES predictions on a single-sector (or double sector in the DOUBLE case, Tab. 7.1) of the annular rig. Streamlines from the averaged flow fields are visualized by Line Integral Convolution (LIC, Cabral & Leedom, 1993) in Fig. 7.10 for the $\Delta\theta = 20°$ (right) and 30° (left) cases. They confirm that the distance between neighboring sectors deeply affects the aerodynamics, especially the central recirculation zone (CRZ in Fig. 7.10), and therefore the flame shape. More importantly, the neighboring azimuthal motions induced by the swirlers interact when burners are close to each other which modifies the jet-opening angle in the XZ-plane but not in the XY-plane: the axi-symmetry of the swirl motion is broken.

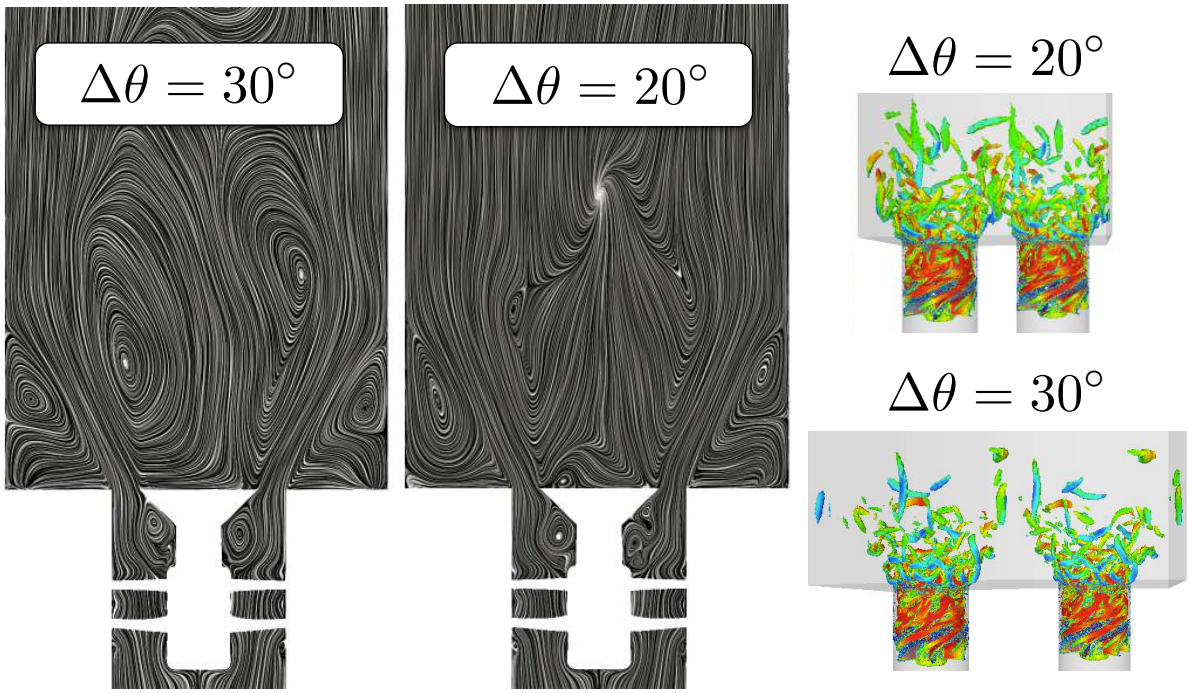

Figure 7.10: LES results: averaged streamlines visualized by Line Integral Convolution (LIC) (Cabral & Leedom, 1993) on the XY-plane (left) and the 3D Q-criterion (right) for the CH4-ADIA-30 ($\Delta\theta = 30°$) and REF ($\Delta\theta = 20°$) cases with no forcing.

On the contrary, taking heat losses into account or changing fuel only has a minor impact on aerodynamics. However, the flame anchoring point is slightly lifted (Fig. 7.11-a, middle) when heat losses are taken into account and the local heat release increases when methane is replaced by ethylene (Fig. 7.11-a, right).

The flame shapes obtained by LES (heat-release fields and iso-contours 20 mm downstream of the bluff-body, Fig. 7.11-b top) with $\Delta\theta = 20°$ and $\Delta\theta = 30°$ are compared to the experimental integrated chemiluminescence results provided by Worth & Dawson (2013*b*) (Fig. 7.11-b, bottom). LES and experiment are in good agreement: the inner flame wrinkling and the outer flame merging are observed in both LES and experiment

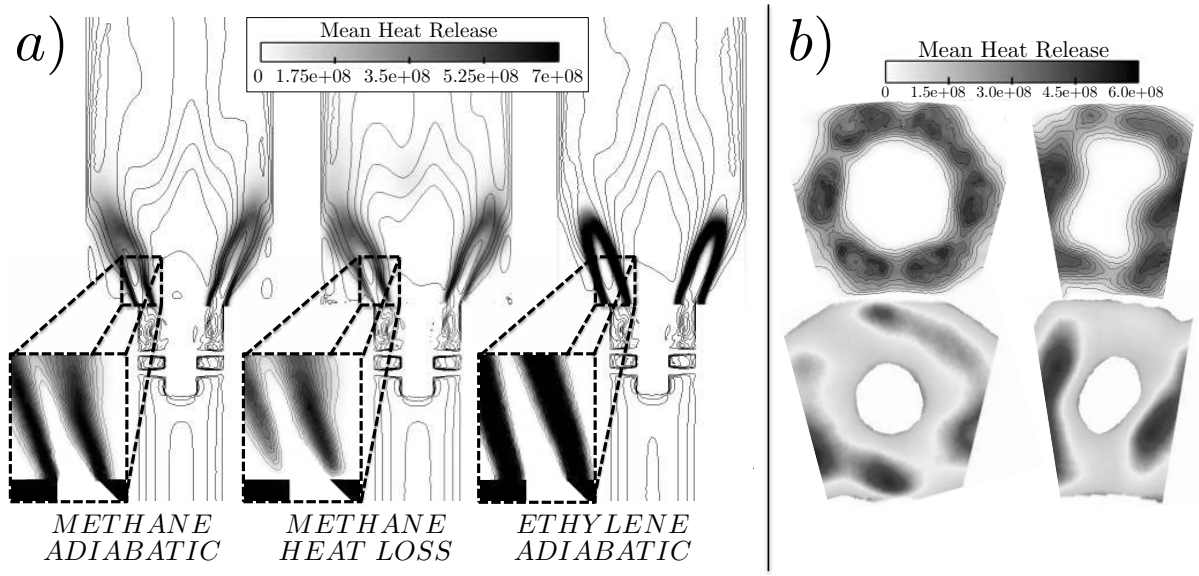

Figure 7.11: a) LES results: XY-cuts of the mean heat release with iso-contours of mean axial velocity for the REF case (left), CH4-HL-20 case (middle) and C2H4-ADIA-20 case (right). Zoom on heat release fields for each flame is provided to highlight the flame anchoring point. b) Comparison between LES heat-release 20 mm downstream of the bluff-body (top) and integrated OH^* measurements (experiment, Worth & Dawson, 2013*b*, bottom) for the case with $N = 12$ (left) and $N = 18$ (right) burners.

in the $\Delta\theta = 20°$ case. Burner/burner interactions clearly appear for $\Delta\theta = 20°$ where the flames are not axisymmetric.

7.5 Phase-averaged forced flow fields

The response of the forced flames at 1800 Hz can be first visualized by the averaged heat release rate at different phase angles of the pressure oscillation: 0° and 180° correspond to a zero acoustic pressure variation at the outflow while 90° and 270° correspond to the maximum and minimum pressure levels respectively. To focus on flame/flame interaction, the visualization domain differs from the single-sector computational domain (Fig. 7.12). As evidenced by Fig. 7.13, flame merging is the main consequence of external forcing for both cases. LES was used to compute the flame response at a frequency $f = 1800\ Hz$. Note that the forcing frequency is fixed and corresponds to the azimuthal frequency observed experimentally. Additional frequencies (1700 Hz and 1900 Hz), upstream/downstream forcing, as well as wave amplitudes (from 0.1% to 1% of the mean pressure) were also investigated and give similar results.

Figure 7.14 shows that the introduction of a model for heat losses strongly modifies the flame shape. Contrarily to adiabatic cases, the flame is lifted, has a weaker outer shear layer flame (Tay-Wo-Chong & Polifke, 2012) and its base oscillates near the injector tip as already evidenced for laminar premixed flames (Kedia *et al.*, 2011). The outer branch oscillates in the axial direction while the inner branch located nearby the bluff-body moves from left to right (—— in Fig. 7.14 displays the minimum and maximum flame

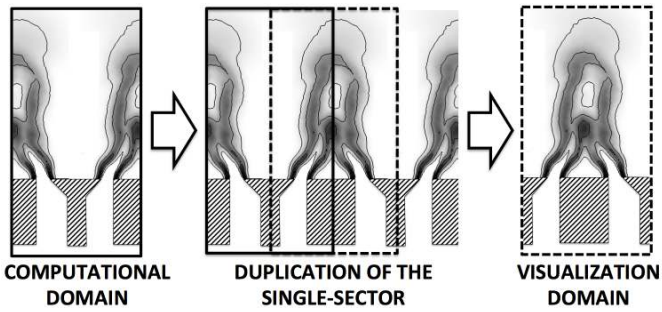

Figure 7.12: Computation domain (left) and visualization domain (right) used to study flame-flame interactions.

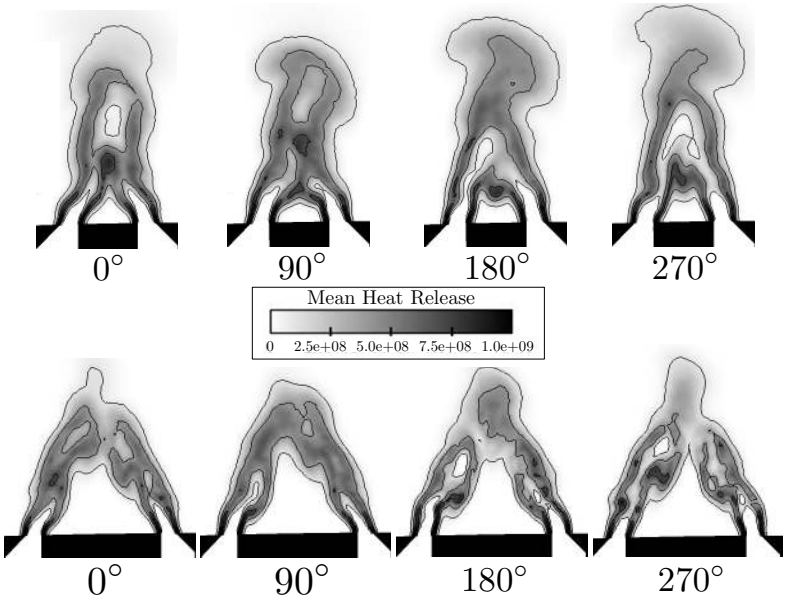

Figure 7.13: XZ-cuts of phase averaged heat release in two consecutive mid injector planes: REF case ($\Delta\theta = 20°$, top) and CH4-ADIA-30 case ($\Delta\theta = 30°$, bottom).

position over the acoustic period).

Replacing methane by ethylene (Tab. 7.1) impacts the flame dynamics (Fig. 7.15). For ethylene (runs C2H4-ADIA-20 and C2H4-ADIA-30), the laminar flame speed ($s^0_{l,\ C_2H_4} \simeq 0.56\ m/s$) and the heat release (as well as the adiabatic temperature $T^{ad}_{C_2H_4} \simeq 2232\ K$) are higher compared to methane ($s^0_{l,\ CH_4} \simeq 0.33\ m/s$ and $T^{ad}_{CH_4} \simeq 2070\ K$) leading to a shorter and more intense flame (Fig. 7.13 for methane and Fig. 7.15 for ethylene). Because of a smaller flame length, ethylene flame merging between neighboring injectors occurs only in the $\Delta\theta = 20°$ case and disappears for $\Delta\theta = 30°$ which is consistent with experimental observations (Worth & Dawson, 2013*b*) (while merging was only weaker for methane with $\Delta\theta = 30°$ compared to $\Delta\theta = 20°$). Note also that due to a higher laminar flame speed, the ethylene flame is less affected by the turbulence than the methane flame, as shown by the resolved wrinkling observed in Figs. 7.13 and 7.15.

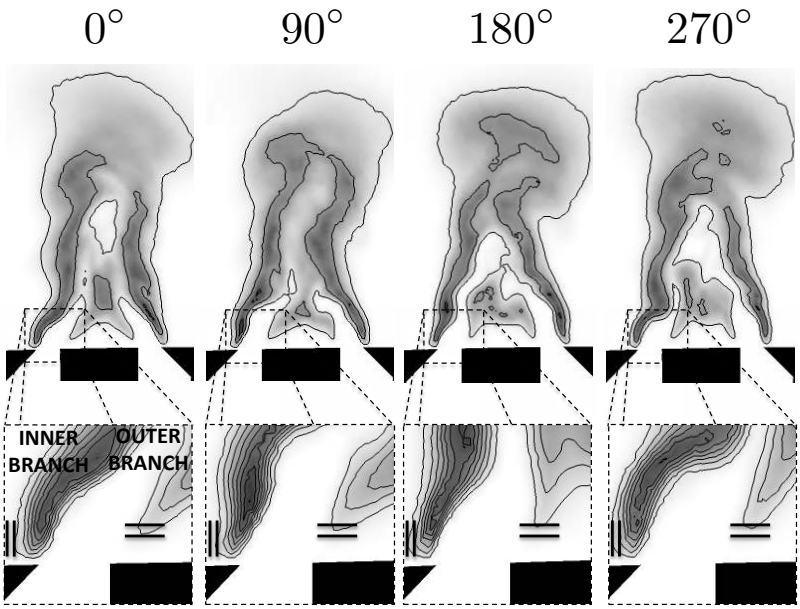

Figure 7.14: XZ-cuts of the phase averaged heat release (same color levels as in Fig. 7.13) for the CH4-HL-20 case (top) complemented by a zoom on the flame base oscillation (bottom). Lines: Minimum/maximum position of the inner and outer flame base.

7.6 Rayleigh criterion

Usually, simple interpretations are proposed to assess the stability of flames. For instance, it is well known that the time-delay of the Flame Transfer Function is crucial to predict combustion instabilities. However, its link with flame quantities is not straightforward. In particular, a direct correlation between the time-delay and the laminar flame speed may be too simple to understand underlying phenomena controlling the stability (heat loss, confinement or even turbulence effects), especially for turbulent non-adiabatic flames affected by flame merging. Therefore, a local criterion should be used to understand which phenomenon is driving the instability. Stability is analyzed here using the Rayleigh criterion to compare methane and ethylene cases. The Rayleigh criterion (R_S) over any surface S is computed from the complex fluctuating pressure ($\hat{p}$) and heat release ($\hat{q}$):

$$R_S = \frac{1}{S}\int_S \|\hat{p}\|\|\hat{q}\|\cos(\Phi_p - \Phi_q)dS \tag{7.2}$$

where $\|\hat{p}\|$ and $\|\hat{q}\|$ are the modulus of the pressure and heat release oscillations and Φ_p and Φ_q are their respective phases. The fluctuating quantities are obtained at the forcing frequency thanks to a Dynamic Mode Decomposition (DMD, Schmid, 2010) of 110 3D snapshots spaced by $\Delta t = 27\mu s$ (corresponding to five periods and a Nyquist cutoff frequency $f_n = 37\ kHz$). Figure 7.16 shows the Rayleigh criterion for the adiabatic methane (top) and ethylene (bottom) cases with $\Delta\theta = 20°$ over three different surfaces. These fields display regions where acoustic-flame interactions occur (grey zones correspond to regions where no flame-acoustic interaction takes place). The modulation of this interaction, from black (negative) to white (positive) is due to the phase between the fluctuating

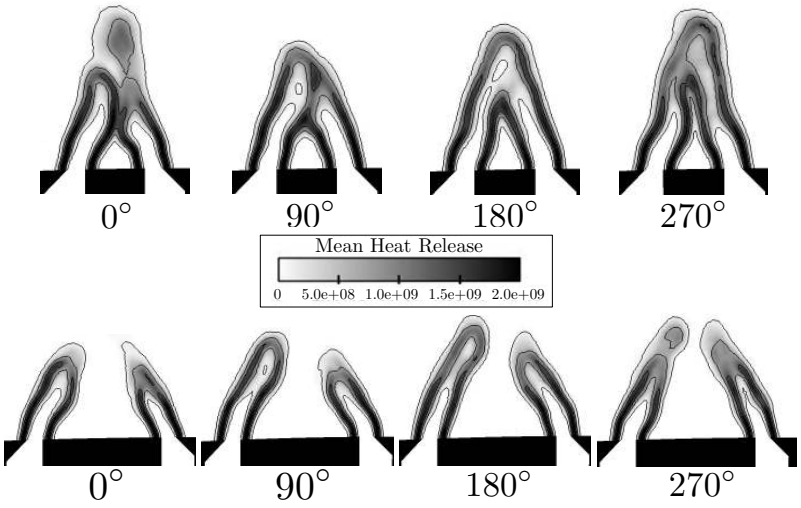

Figure 7.15: XZ-cuts of the phase averaging of the heat release in the C2H4-ADIA-20 case (top) and C2H4-ADIA-30 case (bottom).

pressure and heat release $[\phi_p - \phi_q](\vec{x})$. It clearly shows that even if the flame is compact with respect to the acoustic wavelength (i.e. $\phi_p(\vec{x})$ is almost constant), the local heat release phase $\phi_q(\vec{x})$ (or equivalently the local time-delay $\tau(\vec{x})$) varies strongly due to its convective nature. Consequently, a global criterion based on the volume-averaged time-delay τ is required and sufficient to compute the stability but local phase or time-delays quantities $\tau(\vec{x})$ are necessary to understand which phenomenon is driving the combustion instabilities.

In particular, the YZ-cut (right) highlights the swirler (with 6 blades) effect on stability with a 6^{th}-order azimuthal pattern while the XY and XZ-cuts display the flame-wall (left) and flame-flame (middle) interactions effect. The Rayleigh criterion expressed in Eq. (7.2) corresponds to a volume source (if positive) or sink (if negative) term for the acoustic energy: white zones in Fig. 7.16 promote combustion instabilities while black zones damp them. This local criterion can be integrated: (1) over the whole domain to obtain a global criterion as usually performed when computed a global time-delay or (2) over a small part of the domain to highlight its effect on combustion instabilities: in this work, the Rayleigh criterion is integrated over the XY-cut (left) to focus on flame-wall interaction and over the XZ-cut to focus on flame merging. Results are given in Tab. 7.2 for both methane (top) and ethylene (bottom) cases and show that:

- **Methane case (top):** Integrations of the Rayleigh criterion on both the XY and XZ-cuts of the methane case (top) are negative indicating that regions of flame merging and flame-wall interactions damp the acoustic mode at 1800 Hz.
- **Ethylene case (bottom):** The region of flame merging (along the XZ-cut) is also a sink term for the acoustic energy when using ethylene. However, due to a higher laminar flame speed, the ethylene flame is shorter than the methane flame. In particular, flames do not interact with side walls as observed in Fig. 7.16 (bottom left). The Rayleigh criterion integrated over this direction is positive: compared to the methane case where flame-wall interactions lead to a damping mechanism

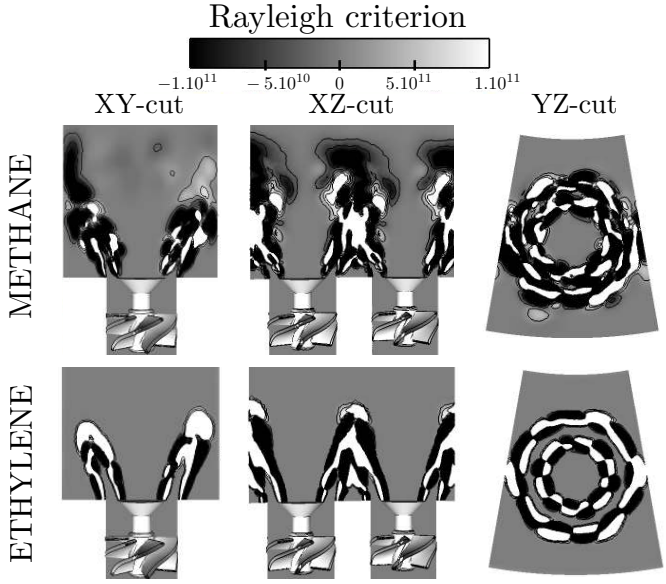

Figure 7.16: Rayleigh criterion constructed from DMD results at 1800 Hz (Eq. (7.2)) over three different surfaces for the adiabatic $\Delta\theta = 20°$ case with methane (top) and ethylene (bottom).

(negative criterion), here the shorter flames avoid flame-wall interaction and are associated to a driving mechanism (positive criterion).

This study shows that local time-delay and Rayleigh criteria are required to describe precisely the local damping or driving mechanisms. Here, the main difference observed between the methane and ethylene cases in both Fig. 7.16 and Tab. 7.2 is the presence or absence of flame-wall interactions along the XY-cut, the only direction in which the Rayleigh criterion goes from negative (damping, methane case) to positive (driving, ethylene case). It suggests that the driving mechanism leading to instabilities when using ethylene is the suppression of flame-wall interaction and not the flame merging. This analysis is in good agreement with experimental observations where changing the flame merging (by changing the azimuthal confinement $\Delta\theta$) had not significant impact on the azimuthal mode occurrence.

CASE	**XY-CUT**	**XZ-CUT**
Methane	$-3270\ W$	$-621\ W$
Ethylene	$+5315\ W$	$-1268\ W$

Table 7.2: Rayleigh criterion (Eq. (7.2)) for the adiabatic $\Delta\theta = 20°$ cases with methane and ethylene over two different surfaces: XY-cut where flame-wall interaction occurs and XZ-cut where flame merging is observed.

7.7 FTF sensitivity study

The sensitivity of FTFs to models (turbulence and combustion) as well as to numerical setups (single/double sectors and coarse/fine meshes) is first evaluated for adiabatic cases with methane and $\Delta\theta = 20°$ (REF, DOUBLE, COLIN, SIGMA and FINE cases in Tab. 7.1, Fig. 7.17). Hatched zones in Fig. 7.17 correspond to the minimum and maximum values of n and τ for these 5 cases. It is a rough indicator of the uncertainty on n and τ due to purely numerical or modeling parameters. Results depend only weakly on modeling parameters for amplitudes n and time-delays τ of the FTF (five first cases in Fig. 7.17): the amplitude n changes from 0.175 to 0.29 while τ varies between 0.29 ms and 0.34 ms.

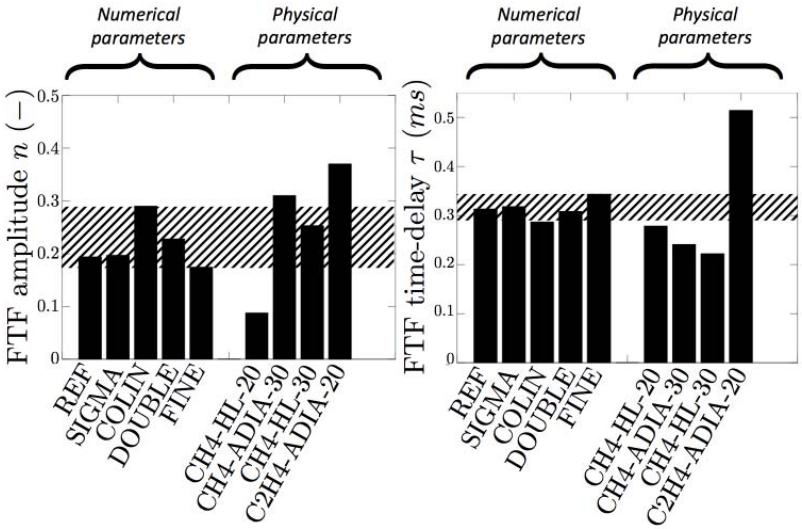

Figure 7.17: FTF amplitudes n and time-delays τ computed by LES for cases of Tab. 7.1.

Thermal, azimuthal confinement ($\Delta\theta = 20°$ or $30°$) and fuel effects were found to have strong impact on unforced (Section 7.4) and forced (Section 7.5) flames. For FTFs, the CH4-HL-20, CH4-ADIA-30, CH4-HL-30 and C2H4-ADIA-20 results (Fig. 7.17) confirm that confinement, thermal and fuel effects are significant compared to uncertainties coming from LES sub-models (hatched zones in Fig. 7.17):

- **Azimuthal confinement:** Using $\Delta\theta = 30°$ instead of 20° modifies the flow topology (Fig. 7.10) and affects flame merging (Fig. 7.13) which leads to a significant amplification of the acoustic/combustion interactions (the amplitude of the FTF n increases) and a shorter flame response (the time-delay τ decreases).
- **Thermal effect:** Including heat-losses modifies the flame shape and introduces flame base oscillations (Fig. 7.14) which are not present for adiabatic LES: both the FTF amplitude n and time-delay τ decrease. This behavior is consistent with other studies on longitudinal configurations (Tay-Wo-Chong & Polifke, 2012; Mejia *et al.*, 2014).
- **Fuel effect:** Methane and ethylene lead to completely different flame responses. The delay with C_2H_4 increases to 0.51 ms compared to about 0.3 ms for CH_4, everything else being equal. It is interesting to see that ethylene flame has a

longer time-delay even though it has a higher laminar flame speed. This shows that kinetics is not the only important factor here: flame-wall interactions, flame merging, heat losses or turbulent combustion effects are more important.

In conclusion, results of Fig. 7.17 allows to: (1) evaluate uncertainties due to numerical and physical parameters on n and τ to be used for UQ studies (Chapter 5) and (2) show that the effects of changes such as fuel or heat release are larger than the effects introduced by uncertainties on numerical parameters.

7.8 Effect of FTF uncertainties on stability of azimuthal modes

Variabilities in FTF numerical estimations have been clearly identified but their impact on the burner stability predictions is not yet evidenced. Helmholtz simulations are now performed using computed FTF to investigate the global stability of the 360° configuration (Fig. 7.9). Stability maps relying on the growth rate $Im(f)$ function of the time-delay τ (varying from 0 to $\tau_c^0 = 1/1800 \simeq 0.55\ ms$) are first computed for two baseline cases corresponding to the annular rig equipped with $N = 12$ burners ($\Delta\theta = 30°$) or 18 burners ($\Delta\theta = 20°$) and using $n = 0.25$ (estimation of an adiabatic case with methane, Fig. 7.17).

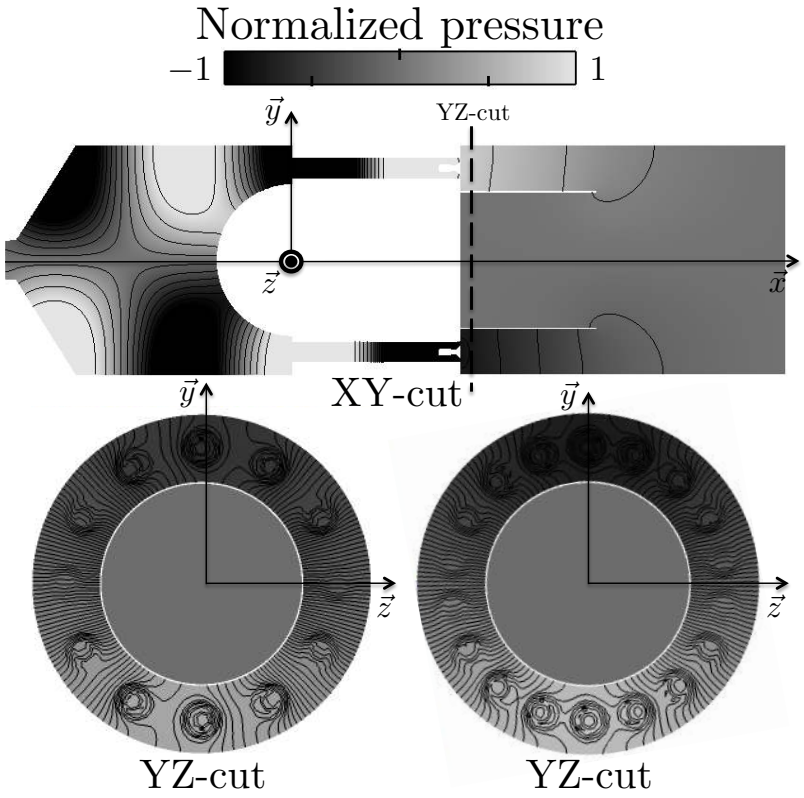

Figure 7.18: Mode structure (here $\|p'\|\cos(\phi)$) of the azimuthal mode at $f \simeq 1800$ Hz: XY-cut (top) and YZ-cuts (bottom) for both the $N = 12$ (left) and $N = 18$ (right) configurations.

The mode structure (*i.e.* $\|p'\|\cos(\phi)$ where $\phi = arg(p')$) of the azimuthal mode at $f \simeq 1800\ Hz$ obtained with AVSP (Fig. 7.18, top) involves both the annular plenum as well as the annular chamber. A longitudinal acoustic component is observed in the chamber because of pressure fluctuations are zero at the chamber outlet. YZ-cuts of the $N = 12$ and 18 burner cases (Fig. 7.9, bottom) underline the differences introduced in the acoustic mode due to the number of burners as well as to the FTF.

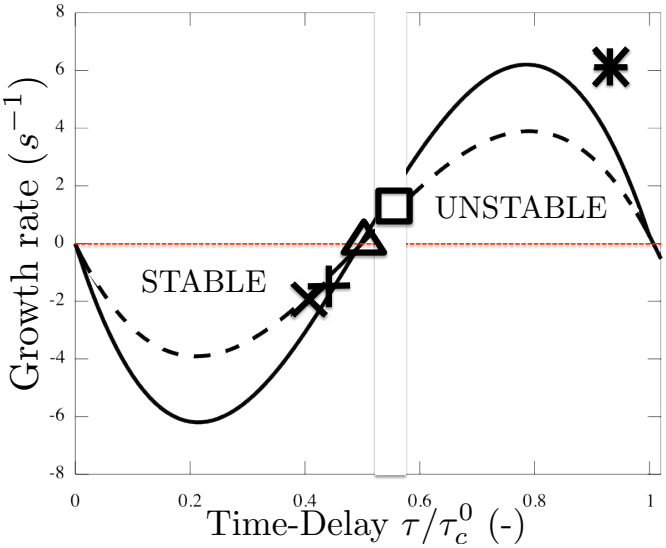

Figure 7.19: Stability maps of the $N = 12$ (---) and $N = 18$ (——) configurations obtained with the FTF amplitude $n = 0.25$ and a time-delay varying from 0 ms to $\tau_c^0 = 0.55$ ms. Growth rates of specific cases are also displayed: □: REF case, △: CH4-HL-20, +: CH4-ADIA-30, ×: CH4-HL-30 and ⋆: C2H4-ADIA-20. The hatched zone corresponds to the uncertainty on the time-delay due to LES sub models (Fig. 7.17)

Figure 7.19 shows the stability maps of the two baseline cases (--- : $N = 12$ and —— : $N = 18$ burner configurations) versus FTF time-delay τ, computed first with $n = 0.25$ (corresponding to an adiabatic case with methane). Results confirm that the azimuthal confinement modifies the acoustic domain leading to different growth rates, everything else being equal: using the same burner characteristics and FTF inputs, the 12 burner case generates lower flame/acoustic perturbations than the 18 burner case (Fig. 7.18 bottom).

Finally, the growth rate of the five distinct cases of interest are displayed on the stability map of Fig. 7.19 (□: REF case, △: CH4-HL-18, +: CH4-ADIA-12, ×: CH4-HL-12 and ⋆: C2H4-ADIA-18): thermal and fuel effects have a significant impact on the overall stability compared to uncertainties due to LES sub-models (hatched zone in Fig. 7.19). Results demonstrate the LES capability to predict FTF accurately and to provide useful results when FTFs are injected in Helmholtz codes: based on the FTFs of Fig. 7.17, the Helmholtz solver predicts correctly that almost all methane cases are stable and adding heat-losses stabilizes (in these cases) the annular rig. Using ethylene leads to a positive growth corresponding also to an unstable configuration. These results are consistent with experimental observations where methane leads only to longitudinal

instabilities while ethylene produces azimuthal instabilities (Worth & Dawson, 2013*b*).

7.9 Conclusion

This chapter describes a sensitivity analysis of the stability of a full annular academic configuration installed in Cambridge. It is based on forced compressible LES of a single (or double) sector computing FTFs which quantify the interaction between acoustics and the turbulent swirled flames. First, effects of different azimuthal confinements (corresponding to the annular chamber equipped with 12 or 18 burners), thermal boundary conditions (adiabatic or with heat losses) or fuels (methane or ethylene) have been investigated and compared to uncertainties on the FTF introduced by LES sub models. Phase-averaged heat release fields and FTF computations show that confinement, thermal and fuel effects are essential and affect the flame shape as well as their dynamics. The local Rayleigh criterion is obtained via a Dynamic Mode Decomposition highlighting which phenomenon is driving the instability: flame-flame (or flame merging) is not the key feature leading to instabilities, but flame-wall interaction does modify the FTF significantly. Then global FTFs computed by LES are used as inputs for an acoustic solver to evaluate the effect of FTF uncertainties on the stability of azimuthal modes in the 360° configuration. Results show that modeling issues inherent to LES models lead to marginal uncertainties on FTF while azimuthal confinement, thermal conditions and fuel type strongly affect the flame response to acoustics and control the stability of the azimuthal mode. In particular, Helmholtz computations show that the annular configuration performed with methane should be stable while ethylene should lead to unstable modes as observed in the real experiment. Thus, an operating point (ethylene, $N = 18$, adiabatic) is chosen to be computed on the full 360° configuration to obtain a self-excited azimuthal mode as discussed in the next chapter.

Chapter 8

LES of self-excited azimuthal modes in a full 360° configuration

Contents

8.1 Introduction 186

8.2 Numerical setup 187

8.3 Growth of a self-excited azimuthal mode 188

8.3.1 Validation of the mean flame shape 188

8.3.2 A self-excited azimuthal mode at 1800 Hz 188

8.4 Structure of the thermo-acoustic modes during the initial phase 193

8.4.1 Fluctuating pressure fields analysis 193

8.4.2 Mode structure and dynamics 195

8.5 Conclusion 197

This chapter focuses on the LES of the full 360° configuration of the experiment of Worth & Dawson (2013b). An operating point (ethylene, N=18 burners, adiabatic) is chosen according to the sensitivity analysis in Chapter 7. Here, a self-excited mode appears and is compared to experimental results provided by Cambridge. Experimental and numerical data have been post-processed during this PhD with the same post-processing methods to ensure a proper comparison. Results show that LES is able to capture a self-excited azimuthal mode at 1800 Hz as in the experiment. However, due to the long establishment of the mode and the extreme cost of 360° LES, only the growth phase is computed while the experiment is able to characterize the limit cycle reached after thousands periods. The numerical study of the establishment of the self-excited mode reveals that it is accompanied, as in the experiment, by longitudinal modes which are due to the start-up procedure and then decrease in time, while the self-excited azimuthal mode is emerging.

8.1 Introduction

Improvement of numerical techniques and the access to powerful supercomputer have allowed the first LES of a thermoacoustic mode of a full 360° industrial combustion chamber in 2010 (Wolf *et al.*, 2010). However, a comparison between 360° simulation and experiment as well as the study of how such a mode appears and grows until its limit cycle is still missing and is the topic of this chapter. While Chapter 7 focused on forced-modes using single or double sector LES with non-reflecting boundary conditions, this chapter targets the full annular rig with realistic inlet/outlet impedances. The annular configuration equipped with $N = 18$ burners, an annular chamber and a large atmosphere exhaust zone is computed by LES in Section 8.3. First, the experimental 360° mean flame shape measurement is compared to integrated heat-release pictures showing a very good agreement. In particular, flame merging already observed in Chapter 7 when $N = 18$ burners are distributed in the chamber leads to specific patterns on the 360° mean flame shape in both experiment and numerical results. A self-excited azimuthal mode appears in the LES at 1800 Hz as in the experiment but accompanied with a 500 Hz mode due to the start-up procedure. For a better comparison, both experimental and numerical data are analyzed with the same post-processing tool and show good agreement. The construction of the experimental spectrogram allows the analysis of the time-evolution of the longitudinal and azimuthal modes. Then the mode structure is characterized in Section 8.4.1 using both FFT (Fast-Fourier Transform) and DMD (Dynamic Mode Decomposition), the two different tools showing that the computed self-excited mode is globally standing. Section 8.4.2 presents a method called JAWA (Joint probability distribution for Azimuthal Waves Analysis) to study time-evolution and probability of azimuthal mode structures in LES. This tool shows that the azimuthal mode in the LES is highly perturbed although mainly standing during the growth phase. Experimental data are investigated using the same methodology showing that the azimuthal mode is mainly standing during the start-up phase before switching to a clockwise spinning mode in the

limit cycle. This analysis shows a good agreement between numerical and experimental data for the start-up phase. It proves that LES is a promising tool to investigate the growth, nature and dynamics of azimuthal modes, a necessary step to understand how they arise and how to control them.

8.2 Numerical setup

In this chapter, the full 360° configuration of the Cambridge experiment detailed in Chapter 7 is investigated. The computational domain includes $N = 18$ burners with an axial swirler composed of six blades mounted on a bluff-body (Fig. 8.1). Combustion takes place in the annular chamber with different wall lengths as in the experiment and a large atmosphere is added to impose properly the outlet impedance of the combustor. The mesh is fully unstructured and contain 110 millions cells, corresponding to a duplication of the "coarse" mesh used in the previous chapter which was proved to accurately predict FTFs. This results in typical thickening factors of 3 to 5 in the flame zone to guarantee $5 - 10$ points in the flame. Cells lengths are typically $150\mu m$ near swirler walls and $150\mu m - 300\mu m$ in the swirler passages.

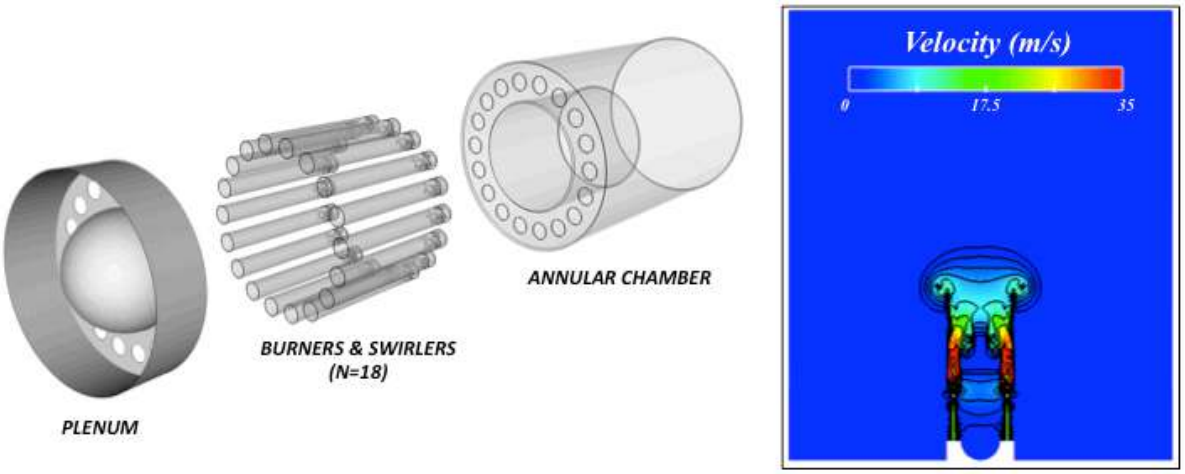

Figure 8.1: 360° LES configuration with the plenum exit, the $N = 18$ burners and the annular chamber with different wall lengths (left). The annular rig is displayed in the large atmosphere exhaust zone (right).

AVBP (Chapter 6) is used here to solve the filtered multi-species 3D Navier-Stokes equations with realistic thermochemistry on the configuration of Fig. 8.1. Based on the experiments (Worth & Dawson, 2013*b*) and the sensitivity analysis performed in Chapter 7, azimuthal modes are expected to be unstable only when using ethylene. Consequently, a perfectly premixed air-ethylene mixture at the equivalence ratio $\phi = 0.85$ is injected at the inlet (plenum/burner section). Reaction rates are modeled with a reduced kinetic scheme containing 2 steps and 6 species (Eq. (8.1)), which have been proved to accurately

reproduce low frequency flame dynamics (Kedia *et al.*, 2011):

$$\begin{cases} C_2H_4 + 2O_2 \Rightarrow 2CO_2 + 2H_2O \\ CO + \frac{1}{2}O_2 \Leftrightarrow CO_2 \end{cases} \tag{8.1}$$

Transport properties (constant Prandtl and Schmidt numbers) have been validated in Chapter 6 using Cantera and AVBP to compute DNS of 1D laminar ethylene/air flames. Numerics is based on a two-step Taylor-Galerkin finite element scheme of third-order in space and time (TTGC, Moureau *et al.*, 2005) to accurately propagate acoustic waves. Chapter 7 shows that, for this configuration, turbulent and combustion models yield minor uncertainties on the flame-acoustics interaction. For this study, the Wale (Nicoud & Ducros, 1999) model has been used and turbulent-flame interactions are addressed using the dynamic Thickened Flame (TF) approach with the efficiency function described by Charlette et al. (Charlette *et al.*, 2002). Boundary conditions use the NSCBC approach (Poinsot *et al.*, 1992). As in the previous section, the plenum cavity has been replaced by an equivalent reflection coefficient measured experimentally ($R \simeq 0.1$ corresponding almost to a non-reflecting condition) and adjusted using the relax coefficient of the NSCBC boundary condition (Selle *et al.*, 2004*b*). Adiabatic temperatures ($T_{ad} \approx 2230K$) and laminar flame speeds ($s_L^0 \approx 0.56\ ms^{-1}$) have been compared to the UCSD full scheme (UCSD, 2013) and show a good agreement. Thermal effects have been neglected (Chapter 7) and walls are treated as non-slip and adiabatic.

8.3 Growth of a self-excited azimuthal mode

8.3.1 Validation of the mean flame shape

Chapter 7 has proved that single sector LES was able to reproduce experimental behavior such as the flame length, the effect of fuel on the stability of azimuthal modes as well as flame merging between neighboring burners. Before analyzing acoustic modes present in the LES, an additional validation of the 360° computation is provided in Fig. 8.2. The flame merging mechanisms observed experimentally between neighboring burners yields a specific pattern on the experimental integrated OH^* measurements, where the rotating symmetry of the flame is broken which enhances combustion between burners (Fig. 8.2, left). The full 360° LES simulation has been post-processed by integrating the mean heat-release in the axial direction (Fig. 8.2, right) and shows a similar pattern. This proves that qualitative experimental results are well reproduced by the full 360° LES even though detailed velocity or species measurements would clearly be required to pursue this comparison.

8.3.2 A self-excited azimuthal mode at 1800 Hz

Self-excited pressure oscillations appear in the annular combustor in both LES and experiment (Worth & Dawson, 2013*b*,*a*) and can be compared. This chapter focuses on

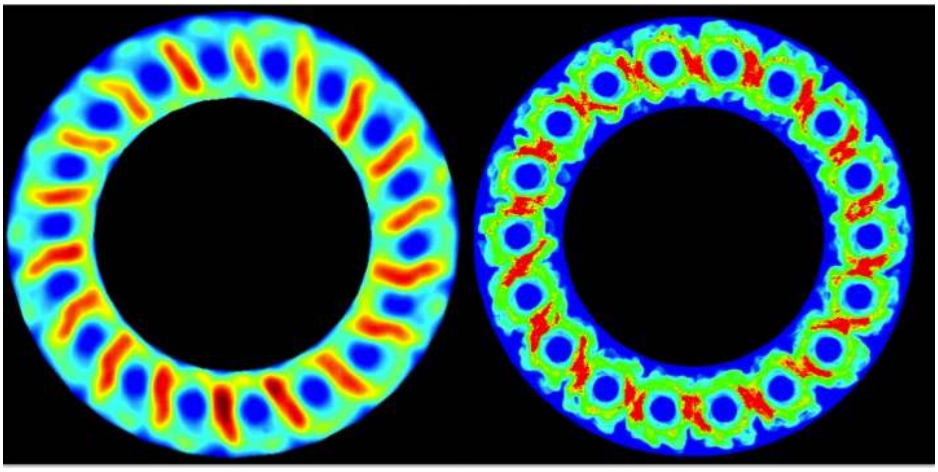

Figure 8.2: Comparison of the integrated mean OH^* in the experiment (left) and heat-release in the LES (right). Typical patterns due to the flame merging are observed both in experiment and simulation.

the start-up phase in which the azimuthal mode is growing. Note however that the experiment and LES are ignited differently:

- **Experiment:** First, the cold reactant flow rate is set to 18 m/s at the bluff body exit with $\Phi = 0.60$ and then is ignited giving a stable flames. The equivalence ratio is then switched to $\Phi = 0.85$ to obtain an unstable azimuthal mode.
- **LES:** A reacting stabilized single-sector simulation (with non-reflecting boundary conditions) is duplicated to obtain a 360° configuration and initial solution. Then a large atmosphere is brutally added to the configuration to impose a pressure node at the chamber outlet and trigger instabilities.

First, the experimental time-series and spectra of the fluctuating pressure (in the chamber) are displayed in Fig. 8.3 for three different signal durations $\Delta t = 800\ ms$ (top), 100 ms (middle) and 10 ms (bottom). The long signal (top) shows that a pure azimuthal limit cycle at 1800 Hz is established after hundred milliseconds. Zooming on the same pressure signal (middle and bottom images) reveals that the azimuthal growth phase is accompanied by longitudinal modes at 500 Hz, 1000 Hz and 1500 Hz which are decreasing in time. They are probably due to the experimental ignition procedure. It also suggests that LES, limited to short signals because of its cost, cannot easily predict the limit cycle of this configuration occurring after hundreds milliseconds. However LES can be used to investigate the growth phase which is the main topic of this chapter. A new methodology called AMT will be presented in Chapter 9 to study limit cycles using 360° LES.

Experimental time-series and spectra are compared to LES predictions in Fig. 8.4. Experimental data provided by Worth & Dawson (2013*b*) are sampled at 30 kHz giving $262,144$ samples over a duration of $10s$. On the other hand LES provides short pressure signals ($25ms$ long) sampled at 40 kHz and requiring a bandpass filtering around 1800 Hz. Consequently for a proper comparison between experiment and LES, the same filtering is applied on the experimental data provided in Fig. 8.3 with the same signal duration ($\Delta t = 25\ ms$ leading to $\Delta f = 40\ Hz$). The resulting filtered pressure signals and

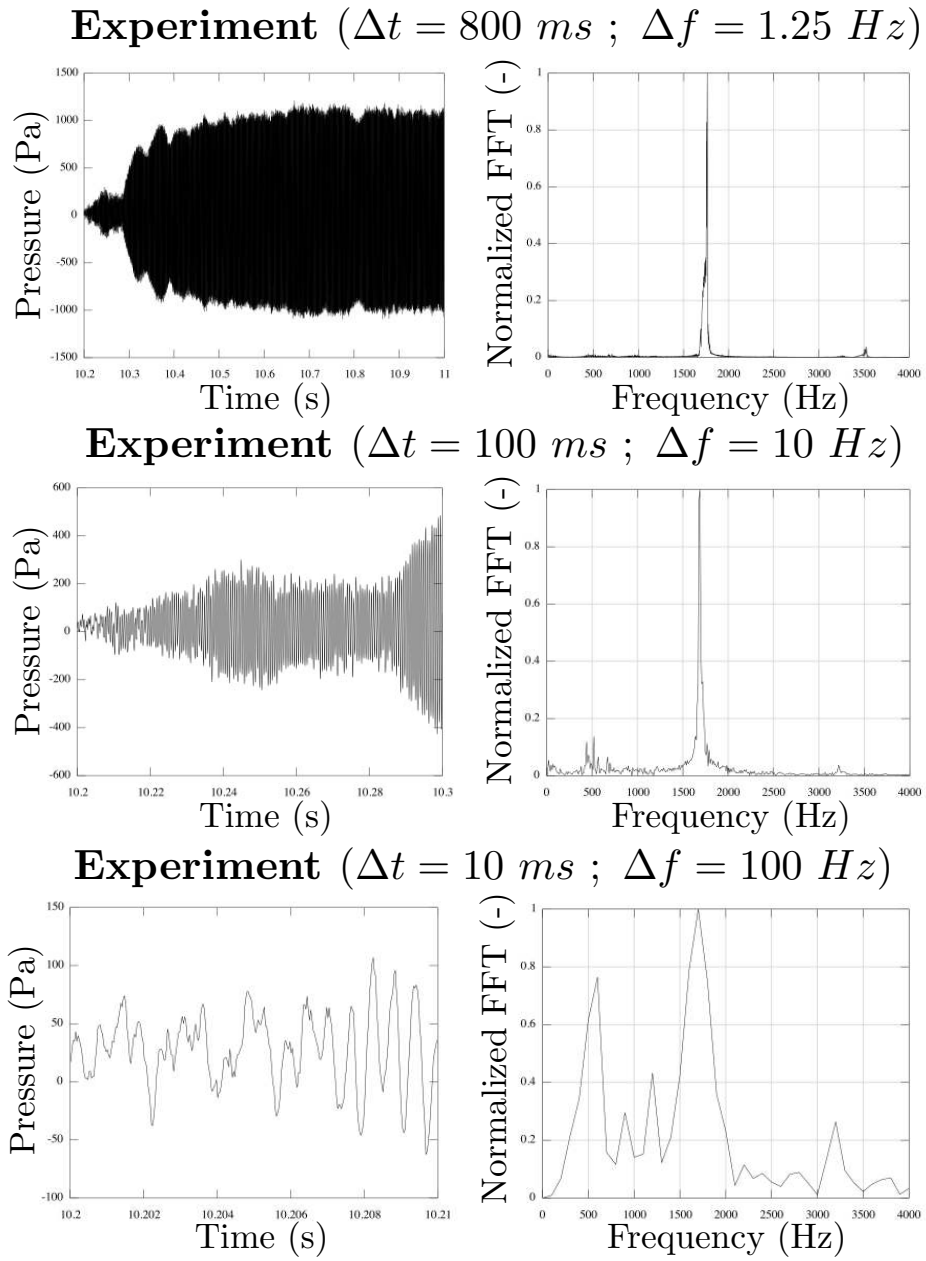

Figure 8.3: Time-series (left) and FFT (right) of experimental measurements provided by Worth & Dawson (2013*b*) from the start-up ($t = t_0$) to $t = t_0 + \Delta t$ where $\Delta t = 800\ ms$ (top), $100\ ms$ (middle) and $10\ ms$ (bottom) with the associated frequency resolution Δf.

spectra are shown in Fig. 8.4 showing that both experiment and LES are unstable. As observed previously, the unstable mode at $f = 1800\ Hz$ in the experiment is accompanied by a strong mode at $500\ Hz$ and a weaker harmonic at $3600\ Hz$. In the LES the mode at $f = 1800\ Hz$ is weaker compared to the other modes although its amplitude (a plateau at about $\pm 200\ Pa$) is larger than the experimental one ($\pm 100\ Pa$ at $t = t_0 + 25\ ms$). A similar plateau at $200\ Pa$ is observed in the experiment (Fig. 8.3, top and middle) but latter after the ignition procedure (from $t = t_0 + 40\ ms$ to $t = t_0 + 90\ ms$). This delay

can be due to the difference between the LES and experiment start-up procedures or by too low numerical acoustic dissipations (no volume viscosity, no heat losses, etc.).

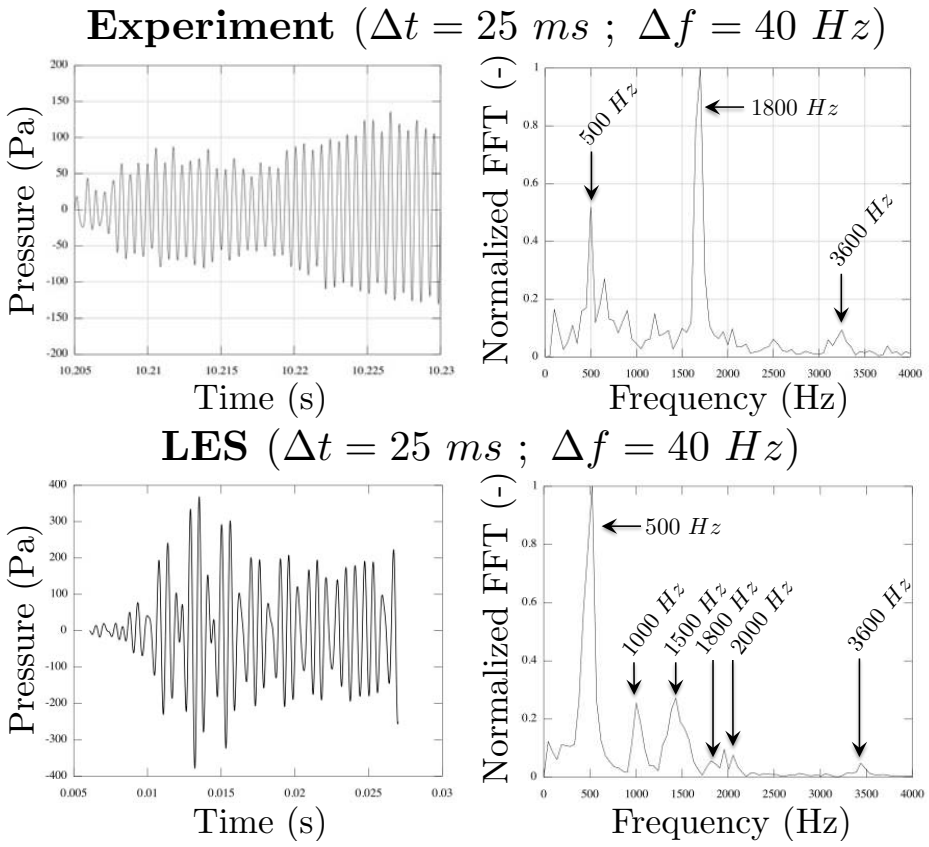

Figure 8.4: Filtered time-series around 1800 Hz (left) and FFT before the filtering (right) of pressure in the chamber from experimental measurements (top) and LES (bottom).

A summary of the time-evolution of the acoustic modes identified in Figs. 8.3 and 8.4 is given by the experimental spectrogram of Fig. 8.5 obtained using multiple FFTs with a resolution $\Delta f = 29\ Hz$ and $\Delta t = 8\ ms$. It shows the evolution of the three main modes observed in Fig. 8.3: the longitudinal mode at 500 Hz and the azimuthal mode at 1800 Hz and 3600 Hz. Dotted lines correspond to the LES and experiment start-up, the end of the transient phase (TP) and the end of the experiment respectively. The end of the LES is displayed by the dashed line, only $\Delta t = 25\ ms$ after the start-up showing that short LES cannot investigate the limit cycle in this case. It is also interesting to note that the 500 Hz and the 1800 Hz modes first appear, as in the LES (Fig. 8.4, bottom). The linear frequency drift observed on the azimuthal mode is due to the temperature increase induced by the combustion ignition. The longitudinal mode at 500 Hz is progressively phased-out while the azimuthal mode is growing. The second order azimuthal mode at 3600 Hz appears one second after the start-up either because (1) it requires a high temperature to exist or (2) because it is non-linearly triggered by the first order azimuthal mode at 1800 Hz or (3) because the combustion chamber is not a pure harmonic oscillator and therefore the 3600 Hz component is a non-linear harmonic

of the first azimuthal mode.

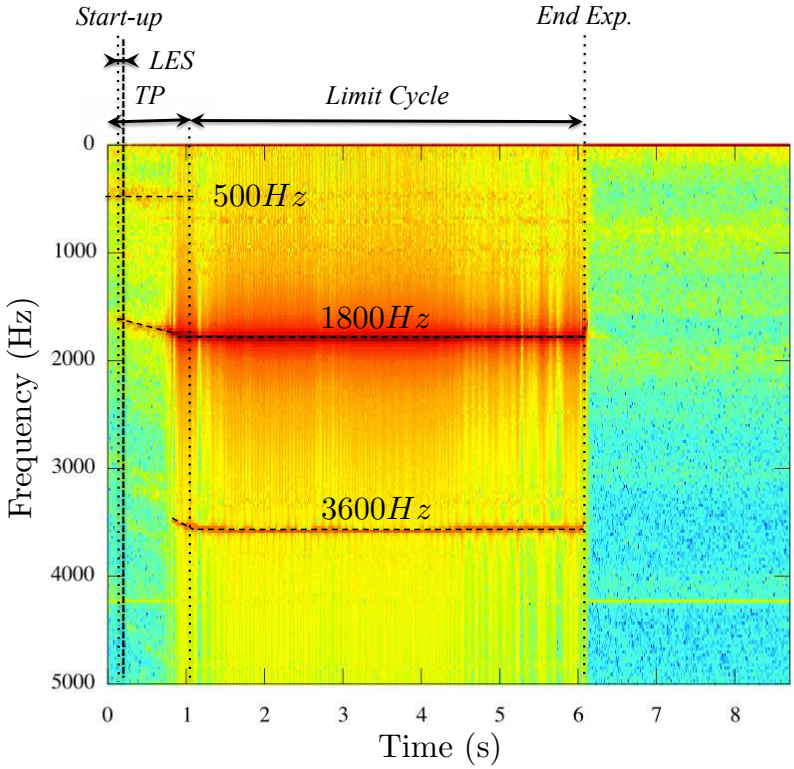

Figure 8.5: Experimental spectrogram obtained from multiple FFTs with a resolution $\Delta f = 29\ Hz$ and $\Delta t = 8\ ms$. It shows the evolution of the three main modes observed in Fig. 8.3: the longitudinal mode at 500 Hz and the azimuthal mode at 1800 Hz and 3600 Hz. Dotted lines correspond to the LES and experiment start-up, the end of the transient phase (TP) and the end of the experiment. The end of the LES is shown by the dashed line, only $\Delta t = 25\ ms$ after the start-up.

Finally, Fig. 8.6 shows several cuts of the instantaneous LES pressure field in the chamber at $\Delta t = 20\ ms$ after the start-up as well as iso-surface of heat release highlighting the flame merging between neighboring sectors. It shows the instantenous azimuthal structure of the acoustic mode observed at 1800 Hz and demonstrates that for the first time LES is able to capture azimuthal thermo-acoustic modes in an academic configuration with an open atmosphere, a complex boundary condition which requires the computation of a large atmosphere (Fig. 8.1, right). This 25ms-long LES has cost $1,500,000$ CPu hours on the GENCI supercomputer Turing with $8,196$ processors. Computing the full initialization phase ($1s$) would cost 60 millions CPu hours. Even though this is feasible today on Prace or Incite machine, an alternative solution to study limit cycles will be proposed in Chapter 9.

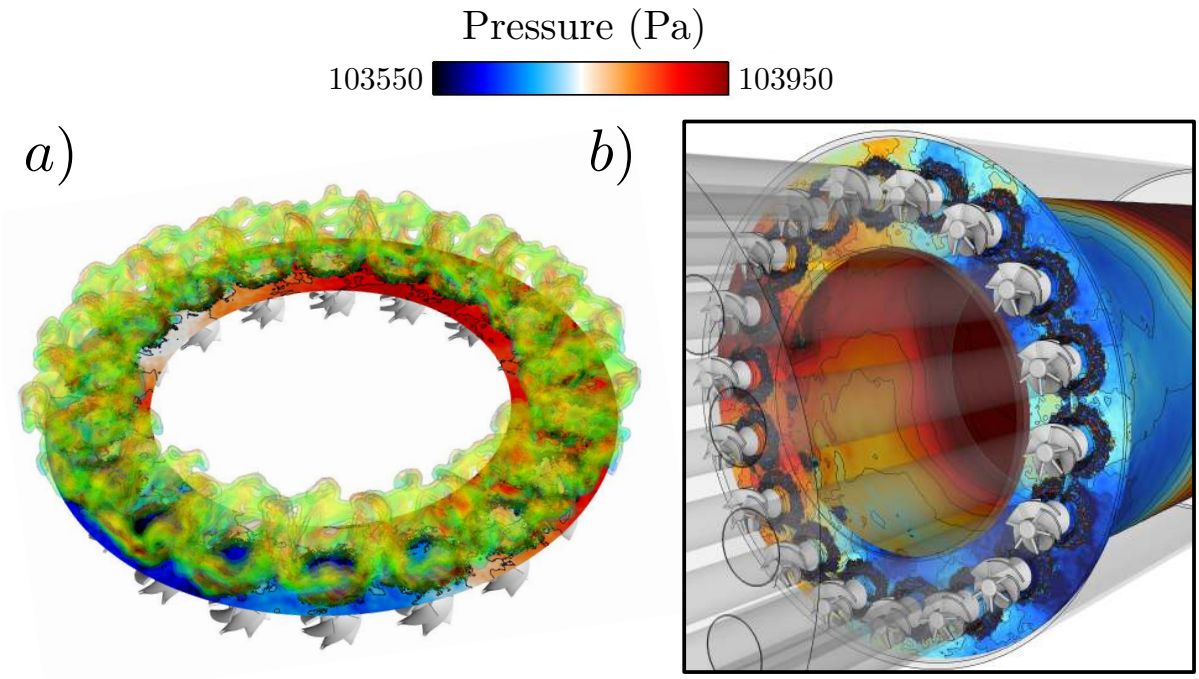

Figure 8.6: a) Transverse cut of the full 360° configuration highlighting the azimuthal pressure and iso-surfaces of heat release showing the flame merging between neighboring burners. b) Transverse and cylinder cuts showing the azimuthal and longitudinal components of the acoustic mode at $f = 1800\ Hz$.

8.4 Structure of the thermo-acoustic modes during the initial phase

8.4.1 Fluctuating pressure fields analysis

To investigate the inner structure and frequency associated to the azimuthal pressure fluctuations observed numerically and experimentally, post-processing tools are performed using Fast Fourier Transform (Fig 8.7, right) on each node of the computational domain and Dynamic Mode Decomposition (Fig 8.7, left) recently proposed by Schmid (2010). These tools provide the modulus $\|\hat{p}\|$ and the phase $\arg(\hat{p})$ of all modes which are then reconstructed:

$$p' = \|\hat{p}\| \cos(\arg(\hat{p}) \tag{8.2}$$

Here, the phase is constant ($\arg(\hat{p}) = 0$ or π, not shown here) which reveals that the mode is standing. As expected, the FFT suffers from a low frequency resolution ($\Delta f = \frac{1}{\Delta t} = 100\ Hz$) because of the limited computational time available: only $\Delta t = 10\ ms$ of simulation has been used here to concentrate on the plateau at $\pm 200\ Pa$. On the other hand DMD provides an accurate estimation of the frequency $f = 1800\ Hz$ as observed in the experiment (Fig. 8.3). Therefore, DMD has been also applied to the other modes present in LES as shown in the pressure signal analysis of Fig. 8.4: a longitudinal mode at 500 Hz and the second azimuthal mode combined with a half-wave longitudinal mode at 3600 Hz.

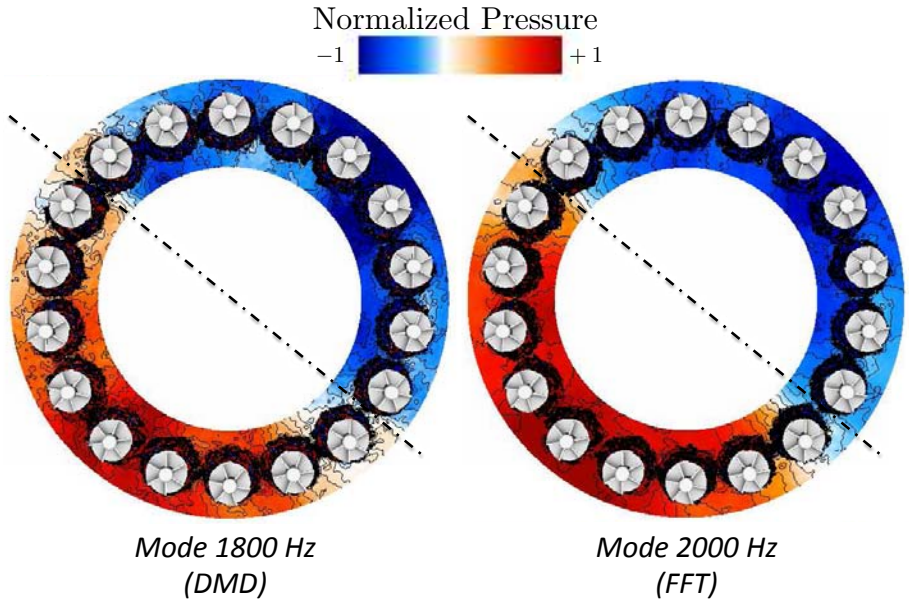

Figure 8.7: Comparison between the azimuthal mode obtained by the Dynamic Mode Decomposition (DMD, left) and Fast Fourier Transform (FFT, right) of the pressure field. the FFT suffers from a low frequency resolution due to the limited time of the LES.

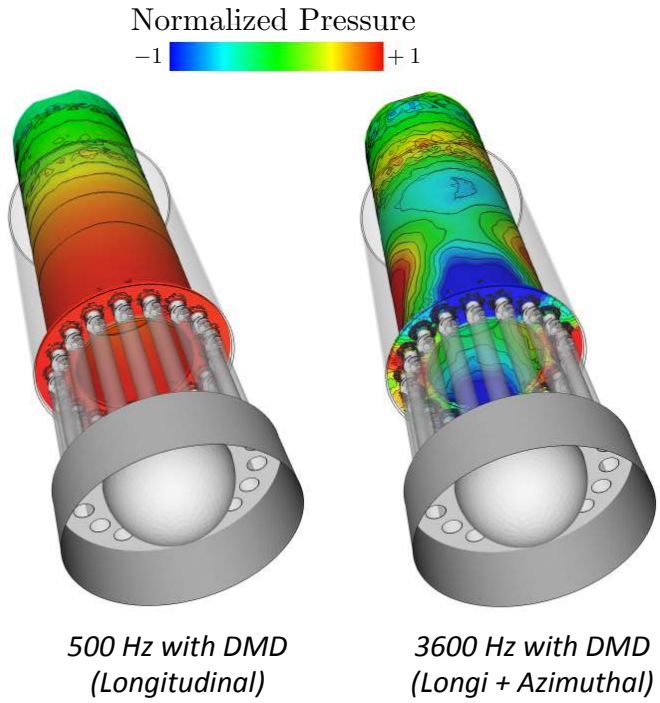

Figure 8.8: The two modes obtained by the Dynamics Mode Decomposition of the pressure field in the full annular LES: the longitudinal 500 Hz mode and the second azimuthal mode combined with a half-wave longitudinal mode at 3600 Hz.

8.4.2 Mode structure and dynamics

The previous section has shown mode structures obtained by FFT or DMD highlighting the global characteristics of the acoustic modes observed in the pressure signal analysis. An additional result of the FTF and DMD tools are the pressure phase which reveals the mode nature: here, the phase is constant ($\arg(\hat{p}) = 0$ or π, not shown here) which implies that the mode is standing. However, such diagnosis is not able to provide information on the mode dynamics and the evolution of its nature (standing, spinning or mixed) with time. Consequently, a five-step methodology is proposed here, called JAWA (Joint probability distribution for Azimuthal Waves Analysis), to analyze simultaneously both the dynamics and the structure evolution of the azimuthal modes:

- **Step 1:** The fluctuating pressure (p') and azimuthal velocity (u'_θ) are extracted from LES results at 4 different locations (Fig. 8.9). These fluctuations are then filtered around 1800 Hz to retain only the first azimuthal mode of the configuration.
- **Step 2:** The two propagating waves are constructed: $q^{\pm}(t) = p'(t) \pm \rho_0 c_0 u'_\theta(t) = A^{\pm}\cos(\omega t)$.
- **Step 3:** The envelopes of these two waves are obtained using the Hilbert transform[1] which gives their respective amplitude called A^+ and A^- (with a low frequency filtering to remove spurious oscillations).
- **Step 4:** The ratio of these amplitude waves A^+/A^-, or more conveniently the index $\alpha(t) = \frac{A^+ - A^-}{A^+ + A^-}$ proposed by EM2C group (Bourgouin, 2014) is computed.
- **Step 5:** Probability density function of $\alpha(t)$ can be computed. Moreover, a 3D shape of the Joint Probability Distribution (A^+, A^-) can be also extracted highlighting the evolution of both the growth and the nature of the acoustic mode. The joint probability distribution (JPD) is computed using a KDE technique (Kernel Density Estimation, detailed in Appendix G) to obtain highly resolved maps from short LES signals[2] of the mode structure in the plane (A^+, A^-).

The JAWA methodology is applied on the four probes P_1 to P_4 displayed in Fig. 8.9 (left) and provides the PDF of the spin ratio α (Bourgouin, 2014) (Fig. 8.9, right). Results show that, as obtained using the FFT and DMD tools, the mode is mainly standing (the mean spin ratio being $\mu_a = 0.03$) during the growth phase computed by LES. An Additional information is however provided compared to the previous tools. In particular, even if the mean state is standing, results show that the acoustic mode is not purely standing but mixed ($\|\alpha\| \simeq 0.5$ with $\sigma_a = 0.20$). However, no pure spinning azimuthal modes ($\|\alpha\| \simeq 1$) are observed.

The PDF of the spin ratio generated by the JAWA methodology is a useful information to analyze the azimuthal mode nature since it provides not only the mean state but its complete distribution (Fig. 8.9, right). In the LES, the azimuthal mode is mainly standing (the mean value of the spin ratio is μ_α) but with high perturbations (the standard

[1] Consider a signal $s(t)$ varying in time. The Hilbert transform of s is $\mathcal{H}(s) = \frac{1}{\pi t} \star s(t)$, where $\star$ designates the convolution product. The signal envelop is then defined as $\mathcal{E}_s(t) = \sqrt{s(t)^2 + \mathcal{H}(s)(t)^2}$.

[2] Unlike classical histograms, KDE provides a resolution which is independent of the number of samples. When the number of samples is limited, as in data extracted from short LES, this technique makes high resolved PDF or JPD possible. More detailed about KDE are given in Appendix G.

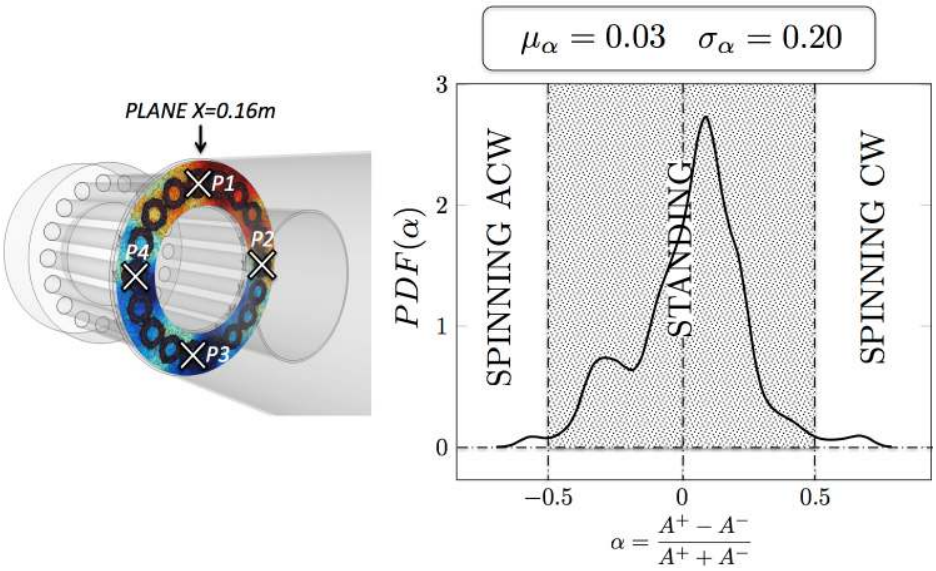

Figure 8.9: The four probes locations where acoustic pressure and velocity are extracted (left) and PDF estimation of the spin ratio α (Bourgouin, 2014) produced by JAWA. It shows that the azimuthal mode is mainly standing (mean value $\mu_\alpha = 0.03$) but with high perturbations (start deviation $\sigma_\alpha = 0.20$) and that no pure spinning modes occur during the growth phase computed by LES.

deviation is $\sigma_\alpha = 0.20$) as shown in Fig. 8.10 (right). The dynamic evolution of the mode structure with time is provided in Fig. 8.10 (left), the question to be answered being: how does the mode structure evolve during the transient phase ? The results show that the standing mode predicted by FFT and DMD tools is not steady but varies dynamically in time (Fig. 8.10, left). An additional information is obtained from the joint probability distribution (A^+, A^-). Indeed, the amplitude of the two waves A^+ and A^- are retained, while in the spin ratio only their respective strength is measured. Figure 8.10 (right) shows iso-contours of the Joint Probability Distribution computed by JAWA. This result indicates that the azimuthal mode is mainly standing during its growth phase but is also highly perturbed, from a standing to a mixed mode. No pure spinning modes occur in this case but the mode structure is slightly growing on the clockwise side (also observed in Fig. 8.9), suggesting that rotating modes might appear in the limit cycle as mentioned by Noiray *et al.* (2011) or can be due to a swirler effect (Worth & Dawson, 2013*b*).

The experimental data given in Fig. 8.3 are post-processed using the same JAWA methodology (the wave amplitudes are however extracted by a routine provided by Worth & Dawson (2013*b*)) to validate LES observations. Figure 8.11 shows the wave amplitudes A^+ (blue, $\times$), A^- (red, $+$) and $A^+ + A^-$ (black, $\square$) (left), the Joint Probability Function $[A^+, A^-]$ (middle) and the Probability Density Function of the normalized wave ratio $\alpha = \frac{A^+ - A^-}{A^+ + A^-}$ (right). These results are compared with numerical data displayed in Figs. 8.9 and 8.10.

Usually, experimentalists have access to long signals and focus on the limit cycle, disregarding the growth phase. This kind of treatment is displayed in 8.11 (top) for experimental data from the start-up ($t = t_0$) to $t = t_0 + \Delta t$ where $\Delta t = 800\ ms$, showing both the start-up phase and the limit cycle. Note that data are missing in the transient

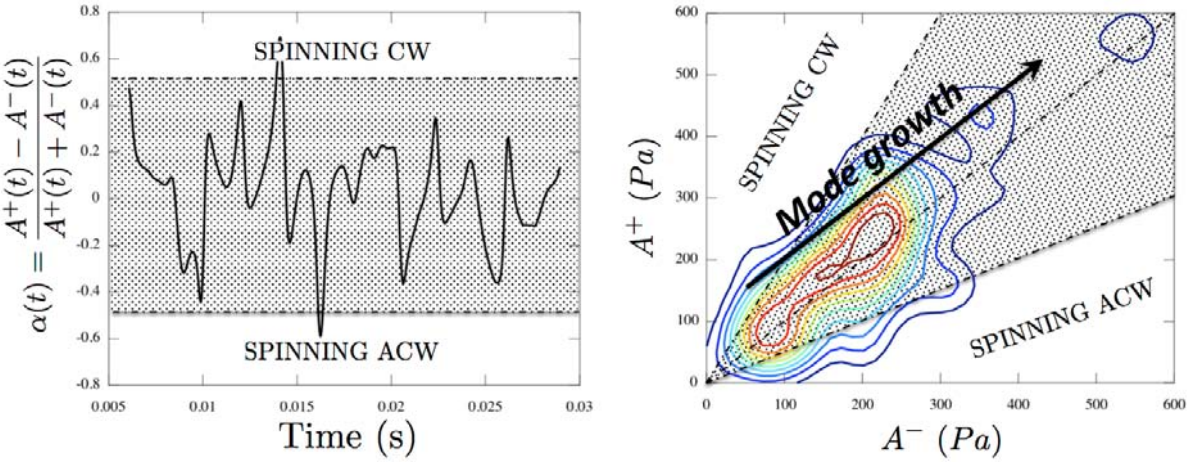

Figure 8.10: Time-evolution of $\alpha(t)$ (left) and isco-contours (right) of the joint probability distribution of (A^+, A^-) obtained by the JAWA methodology. Results show that the azimuthal mode, mainly standing during the growth phase, is also highly perturbed changing from standing to mixed. However, no pure spinning modes are found in this case.

phase (denoted NL-phase in Fig. 8.11) because of difficulties in the wave amplitudes extraction, probably due to the high non-linearities controlling this phase. The Joint Probability Function and Probability Density Function shows that the azimuthal mode nature fluctuates from a standing mode to a clockwise spinning mode, as already observed by Worth & Dawson (2013*b*,*a*) for this configuration. The mode nature during the linear growth phase is also displayed and is further studied in Fig. 8.11 (middle, $\Delta = 100\ ms$): this phase is mainly controlled by dynamic effects with large perturbations on the mode nature. Zooming on the start-up phase (the first $\Delta t = 20\ ms$), which corresponds to the LES computation, reveals that, as in the LES, the mode is initially standing (main peak around $\alpha = 0.03$ in LES and $\alpha = -0.03$ in the experiment) with a second small peak corresponding to an anti-clockwise spinning mode (peak around $\alpha = -0.3$ in the LES and -0.2 in the experiment) also appears. Compared to LES, the mode nature is less perturbed in the experiment with a standard deviation $\sigma(\alpha) = 0.06$ in the experimental start-up phase and $\sigma(\alpha) = 0.20$ in the LES, a point not fully understood yet. This behavior has been encountered in all the 10 independent experimental results provided by Worth & Dawson (2013*b*): the mode is always standing during the start-up phase and then becomes mostly spinning in the clockwise direction. These results shows that the growth, nature and dynamics of the azimuthal mode is globally well captured by LES. It proves that Large Eddy Simulation is a promising tool to investigate the growth of azimuthal modes, a necessary step to understand how these modes arise and how to control them.

8.5 Conclusion

This Chapter describes an LES of the full annular configuration of Cambridge. An operating point (ethylene, $N = 18$ burners, adiabatic) is chosen according to the sensitivity

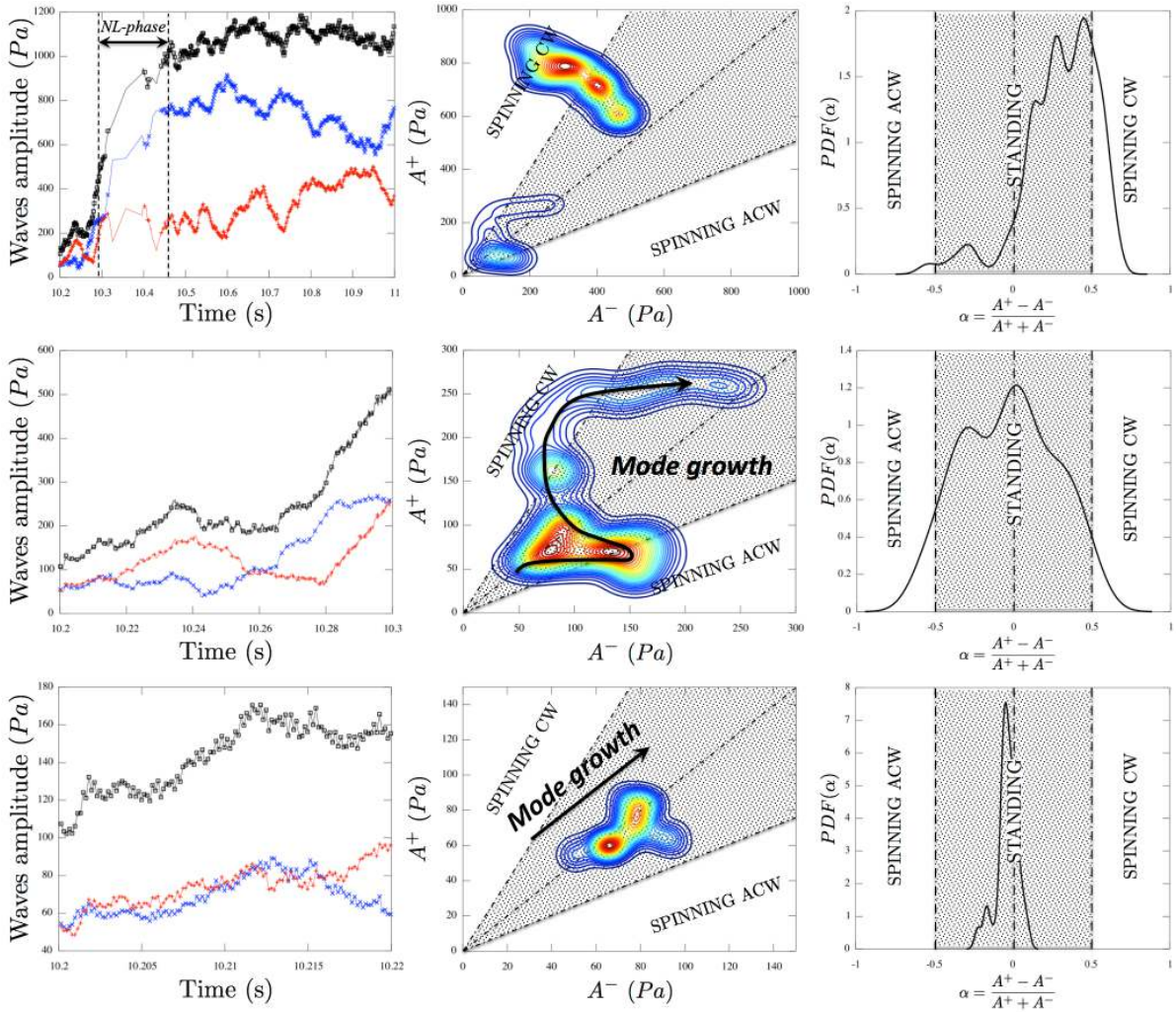

Figure 8.11: Mode structure analysis of experimental data provided by Worth & Dawson (2013*b*) for three different signal durations corresponding to Fig. 8.3: from the start-up ($t = t_0$) to $t = t_0 + \Delta t$ where $\Delta t = 800\ ms$ (top), $100\ ms$ (middle) and $20\ ms$ (bottom). The Jawa methodology is applied to obtained the waves amplitudes A^+ (blue, $\times$), A^- (red, $+$) and $A^+ + A^-$ (black, $\square$) (left), the Joint Probability Function (middle) and the PDF of the normalized waves ratio α (right).

analysis performed on previous forced-LES. First, mean azimuthal flame patterns obtained by integrating the LES heat release are compared to mean OH* measurements and show a good agreement. Then, the self-excited mode which appears in the LES is compared to experimental results provided by Cambridge. Experimental and numerical data have been post-processed with the same treatment to ensure a proper comparison. Results show that LES is able to capture a self-excited mode at 1800 Hz as in the experiment. However, due to the long establishment of the mode and the extreme cost of 360° LES, only the growth phase is computed while the experiment is able to fully capture the limit cycle. The study of the establishment of the self-excited mode reveals that it is accompanied, in both LES and experiment, by longitudinal modes which are due to the start-up procedure. Moreover, the azimuthal mode structure, which is predicted as

standing by classical tool (FFT, DMD), is in fact complex and highly perturbed. these numerical results are compared to experimental data post-processed with the same tool showing a good agreement for the start-up phase. Nevertheless, the complexity of the actual configuration and the limited data available by classic LES because of its cost make the study of symmetry breaking in such a complex configuration difficult. Consequently, a new methodology called AMT is proposed in the next chapter to investigated limit cycles and mode structure using LES at low cost.

Part III

Acoustic Mode Triggering: from low-order models to Large Eddy Simulations

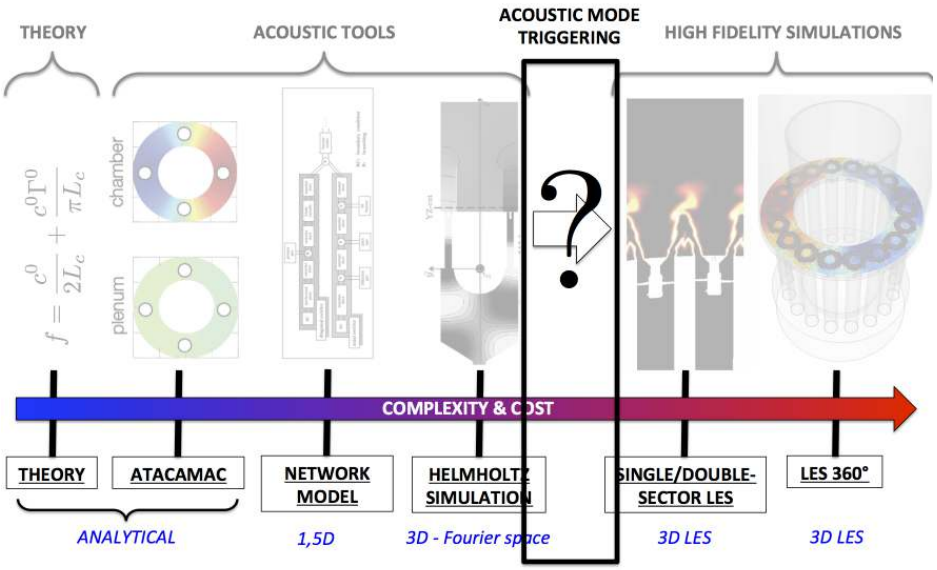

This part has lead to the following publication:

1) M. Bauerheim, F. Nicoud and T. Poinsot, *'Study of acoustic mode dynamics in simplified annular configurations using DNS and an Acoustic Mode Triggering (AMT) approach'* (**in preparation**)

Chapter 9

Study of acoustic mode dynamics using Acoustic Mode Triggering (AMT): validation on longitudinal configurations

Contents

9.1 Introduction 204

9.2 Acoustic Mode Triggering (AMT) methodology 206

9.3 AMT validation on a longitudinal configuration 209

9.3.1 Objectives and longitudinal setup 209

9.3.2 AMT results on the laminar configuration 209

9.4 AMT validation on a turbulent configuration 211

9.5 Conclusion 214

The previous chapter has revealed that LES studies of thermo-acoustic modes in turbulent annular configurations are a complex task mainly because of the numerical short signals which can be obtained on present machines. Moreover, the limitations of linear methods to study instabilities in combustion systems are a usual controversial question: this chapter presents a method to verify the quality of linear predictions and theories for combustion instabilities presented in Part I of this thesis by using them as initial solutions of a LES or DNS solver. This approach (called AMT for Acoustic Mode Triggering) uses the results of a Helmholtz solver (at zero Mach number) or of theory (at zero or non-zero Mach number) as an initial condition of a LES to focus on this single mode growth. Such an approach provides the numerical estimation of the damping/growth rate of the injected mode and its limit cycle as well. In this chapter, the methodology is validated on longitudinal laminar configurations with various mean flows. An additional test case is presented where turbulence is injected to study its impact on the acoustic mode which is still an open topic today and is assumed to play a role in mode switching in certain theories (Noiray et al., 2011). Results show that AMT is able to reproduce non-linear behaviors such as acoustics at non-null Mach numbers. When turbulence is injected, non-linear interactions between the acoustic mode and the turbulence are observed leading to harmonics generation, which may explain why azimuthal modes may change nature in turbulent flames.

9.1 Introduction

The usual approaches to study combustion instabilities are (1) Large Eddy Simulations (High fidelity simulations, Fig. 9.1, right), (2) Helmholtz simulations assuming a zero Mach number flow (Pankiewitz & Sattelmayer, 2003; Nicoud *et al.*, 2007; Evesque & Polifke, 2002) (acoustic tools, Fig. 9.1, middle) and (3) theory on idealized configurations where only key phenomena are retained (Fig. 9.1, left). All these approaches have limitations:

- LES remains a very expensive approach as shown in Chapter 8. Moreover it usually features all modes appearing in a combustor and does not allow to isolate them unless specific treatments and advanced post-processing are introduced.
- Helmholtz solvers are much more efficient in terms of CPU time but since they assume a zero Mach number flow, they obviously miss convective effects. For most combustion chambers where the Mach number is small, convective mechanisms do not modify frequencies significantly but they do affect growth rates (Nicoud & Wieczorek, 2009; Dowling, 1995). Since growth rates control stability and are the most important output of such studies, the zero-Mach number hypothesis remains a major drawback and limitation.
- The flame response modeling used in Helmholtz solvers is usually approximate: Flame Transfer Function (FTF) approaches (Poinsot & Veynante, 2011; Paschereit *et al.*, 2002; Polifke *et al.*, 2001*b*) are the most common method and rely on multiple assumptions (linearity, flame response controlled only by the axial acoustic velocity

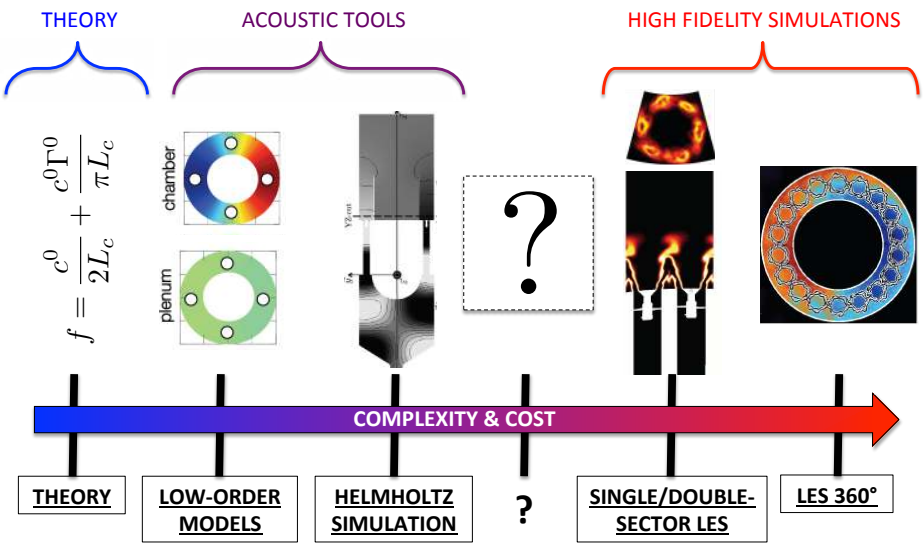

Figure 9.1: Tools developed to study acoustic and combustion instabilities: theory, low-order models, Helmholtz simulations and Large Eddy Simulations. A tool is missing between acoustic tools and high fidelity simulations.

fluctuations etc.).

- Theory allows to identify key phenomena involved in combustion instabilities but non-linear and mean flow effects as well as damping are still difficult to study analytically.

Usually LES and Helmholtz solvers are used separately although they already complement each other. LES information is indeed useful for the Helmholtz solver: for example, the Helmholtz solver requires a sound speed field and a model to take into account the unsteady combustion which can be obtained from a forced LES (Kaufmann *et al.*, 2002; Tay Wo Chong *et al.*, 2010; Kedia *et al.*, 2011; Duchaine & Poinsot, 2011). The main idea of the AMT (Acoustic Mode Triggering) methodology is to feed information in the other direction: from the Helmholtz solver to the LES code. This is done by using the Helmholtz eigenmodes to construct an initial solution fed to the LES solver. This is an approach which is similar to injecting Orr-Sommerfeld linear modes (Orr, 1907*a*,*b*) into CFD solvers to initialize these modes in a time-domain simulation and study hydrodynamic instabilities. The AMT approach has multiple advantages:

- The first advantage of AMT is its ability to use a single mode obtained by linear analysis (e.g. with a Helmholtz solver) and see in the LES how this mode grows and reaches a limit cycle (or not). This is a classical controversial issue in thermoacoustics where the usefulness of linear analysis is often questioned.
- AMT allows to relax the zero-Mach number assumption used in the Helmholtz solver: once a mode is identified in the Helmholtz solver, its exact growth rate can be determined by LES rapidly, taking into account all convective effects and damping phenomena.
- AMT provides an initial field which contains a single and well identified theoretically unstable mode which can be then analyzed in time and space more easily than for a

LES initialized randomly where multiple modes can grow and interact. Chapter 8 showed that the growth phase of a mode can be very long to capture with LES: being able to directly initiate an LES with the proper mode is an attractive path.

- AMT allows to control the initial mode structure: nature and pressure level. For annular configurations, a spinning, standing or mixed mode can be injected. Therefore effects of the mode structure on growth rate or limit cycles can be easily investigated.

The principle of AMT is described in Fig. 9.2: starting from a mean LES field (1), an acoustic tool (Helmholtz solver assuming zero Mach number or theory accounting for mean flow effects) identifies the unstable frequencies and the associated acoustic eigenmodes (2). One of these eigenmodes is reconstructed at a given time (3) and injected onto a three-dimensional initial condition for the LES (4). The LES solver then locks on this mode and predicts its time evolution accounting for all effects (non zero Mach number, realistic flame response and damping phenoma). An implicit assumption here is that the LES code will indeed adjust to the mode injected obtained using a Helmholtz solver, even though this mode does not include all effects that LES captures. As shown below, this seems to be the case in all the tests done here.

AMT is valid for any combustor but this Chapter focuses on its validation on simple longitudinal configurations while the next chapter emphasizes on annular combustors and symmetry breaking effects. These cases are studied with no combustion to highlight that non-linear flame behavior is not necessarily the only feature controlling the mode structures, as evidenced from experiments (Worth & Dawson, 2013*b*,*a*) and recent theories (Bauerheim *et al.*, 2014*e*).

This chapter describes the AMT (Acoustic Mode Triggering) approach in Section 9.2 where an acoustic mode computed by a Helmholtz solver or given by theory is imposed as an initial condition for LES, avoiding the computation of transient time required to reach limit cycles and allowing the numerical estimation of the damping/growth rate of the injected mode. AMT is evaluated on simple longitudinal configurations where multiple Mach numbers are tested. The injected mode is taken from: 1) a Helmholtz simulation assuming a zero-Mach number or 2) 1D theory accounting for an axial mean flow. Results show that at low-Mach number, both the Helmholtz and analytical solutions are properly injected into the LES domain. An additional test case is provided by adding turbulence to the baseline flow to investigate its impact on the acoustic mode. It shows that a non-linear interaction between acoustics and turbulence arises and triggers several modes. Mode structures of these generated modes are analyzed using FFT and DMD and compared to acoustic mode of the system: they correspond to harmonics of the injected mode that the interaction between acoustics and turbulence has triggered.

9.2 Acoustic Mode Triggering (AMT) methodology

Acoustic Mode Triggering (AMT, Fig. 9.2) methods use the output of an acoustic tool (Helmholtz solver or theory) as an initial condition for the LES solver (Fig. 9.2) which avoids computing the transient time required to reach the limit cycle and also allows to

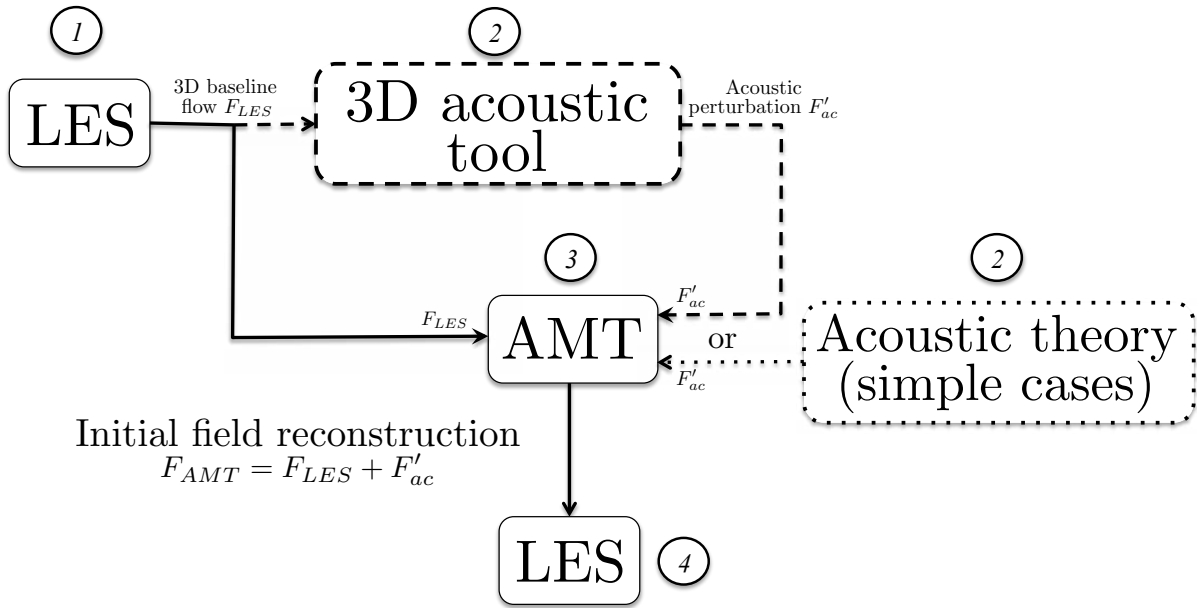

Figure 9.2: Principle of the AMT methodology: 1) An LES is performed and used as a baseline flow 2) A 3D acoustic solver (- - -) or theory (·····) provides the acoustic mode of the configuration 3) The acoustic mode is then added to the baseline flow into the LES domain 4) The limit cycle or the numerical estimation of the damping/growth rate of the injected mode are obtained using an LES at low cost. AMT can also be used with DNS.

focus on a single mode. This is done as follows.

First, acoustic quantities (subscript ac) are extracted from a Helmholtz simulation or theory. In longitudinal configurations only one acoustic component (subscript 1) is required while azimuthal modes investigated in the next chapter need to combine two different solutions (subscripts 1 and 2) to recover standing, spinning or mixed modes:

$$\begin{cases} P_{ac} = \alpha_1 \|\hat{P}_1\| \cos(\phi_{p,1}) + \alpha_2 \|\hat{P}_2\| \cos(\phi_{p,2}) \\ \overrightarrow{V_{ac}} = \alpha_1 \|\overrightarrow{\hat{V}_1}\| \cos(\phi_{v,1}) + \alpha_2 \|\overrightarrow{\hat{V}_2}\| \cos(\phi_{v,2}) \end{cases} \tag{9.1}$$

where $\|\hat{P}_i\|$ and $\|\overrightarrow{\hat{V}_i}\|$ are the pressure and velocity modulus while $\phi_{p,i}$ and $\phi_{v,i}$ are the pressure and velocity phases of the i^{th} component of the acoustic mode computed by the Helmholtz solver. Since this chapter focuses on longitudinal cases for validation, α_2 can be set to zero in the following.

The acoustic density and temperature are obtained using the isentropic relation and read:

$$\rho_{ac} = \frac{P_{ac}}{c^2_{LES}} = \frac{\alpha_1}{c^2_{LES}} \|\hat{P}_1\| \cos(\phi_{p,1}) + \frac{\alpha_2}{c^2_{LES}} \|\hat{P}_2\| \cos(\phi_{p,2}) \tag{9.2}$$

$$T_{ac} = \frac{P_{ac}}{\rho_{LES} C_p} = \frac{\alpha_1 \rho_{LES}}{C_p} \|\hat{P}_1\| \cos(\phi_{p,1}) + \frac{\alpha_2 \rho_{LES}}{C_p} \|\hat{P}_2\| \cos(\phi_{p,2}) \tag{9.3}$$

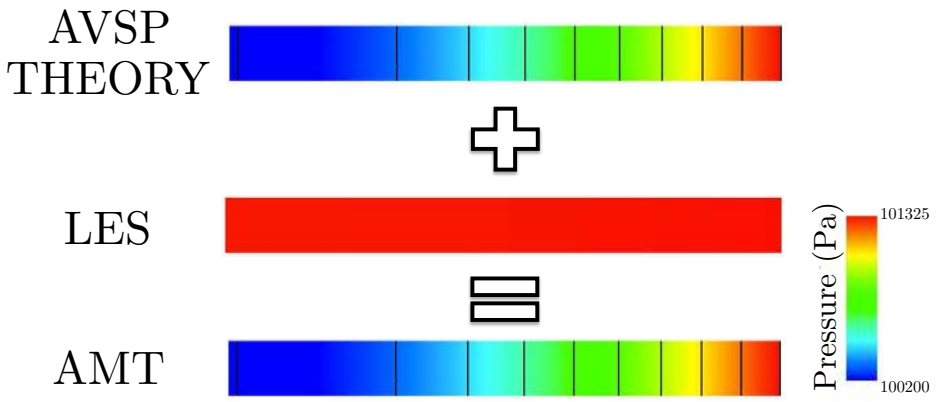

Figure 9.3: AMT methodology: a Helmholtz solution of a longitudinal 3D pipe (top) is combined with a 3D instantaneous LES solution (middle) as a new initial condition for the LES solver (bottom). Here the LES solution is trivial: homogeneous flow.

where c_{LES} and ρ_{LES} are the sound speed and density in the LES simulation around which acoustic linearization has been performed. Then acoustic quantities are added to the LES pressure, temperature, density and conservative velocity and species[1]:

$$\begin{cases} P_{AMT} = P_{LES} + P_{ac} \\ T_{AMT} = T_{LES} + T_{ac} \\ \rho_{AMT} = \rho_{LES} + \rho_{ac} \\ \rho\overrightarrow{V_{AMT}} = \rho\overrightarrow{V_{LES}} + \rho_{LES}\overrightarrow{V_{ac}} \\ \rho Y^k_{AMT} = \rho Y^k_{LES} + \frac{\rho_{ac}}{\rho_{LES}}\rho Y^k_{LES} = \frac{\rho_{AMT}}{\rho_{LES}} Y^k_{LES} \quad \text{for species} \quad k = 1 \text{ to } N_{sp} \end{cases} \tag{9.4}$$

The total energy is finally reconstructed from Eq. (9.4) and reads:

$$\rho E_{AMT} = \rho E_s + \frac{1}{2}\left(\rho u^2 + \rho v^2 + \rho w^2\right) \tag{9.5}$$

where the conservative sensible+chemical energy ρE_s and kinetic energy ρu^2, ρv^2 and ρw^2 are defined as follows:

$$\rho E_s = \int_{T_0}^{T_{AMT}} C_v dT - \frac{RT_0}{W} + \frac{1}{\rho_{AMT}} \sum_{k=1}^{N_{sp}} \Delta h^0_{f,k} \rho Y^k_{AMT} \tag{9.6}$$

$$\rho u^2 = \frac{1}{\rho_{AMT}} \left(\rho u_{AMT}\right)^2 \quad , \quad \rho v^2 = \frac{1}{\rho_{AMT}} \left(\rho v_{AMT}\right)^2 \quad , \quad \rho w^2 = \frac{1}{\rho_{AMT}} \left(\rho w_{AMT}\right)^2 \tag{9.7}$$

where T_0 is a reference temperature, C_v is the heat capacity at constant volume of the mixture, W is the mean molecular weight of the mixture, $R = 8.314\ J\text{mole}^{-1}K^{-1}$ is the perfect gas constant and $\Delta h^0_{f,k}$ is the formation enthalpy of species k. Hence, Eqs. (9.4) and (9.5) provide suitable conservative variables (ρ_{AMT}, $\rho\overrightarrow{V_{AMT}}$, ρY^k_{AMT} and ρE_{AMT}) close to 3D Navier-Stokes solutions to generate proper acoustic mode triggering without additional spurious perturbations.

[1]The conservative species are changed due to the acoustic perturbations acting on the density.

9.3 AMT validation on a longitudinal configuration

9.3.1 Objectives and longitudinal setup

First the AMT methodology is evaluated on a simple longitudinal configuration described in Fig. 9.4. This problem corresponds to a 3D pipe where zero velocity fluctuation is imposed at the inlet ($u' = 0$) and zero pressure fluctuation at the outlet ($p' = 0$). A mean homogeneous axial flow is added (Fig. 9.5), characterized by its axial Mach number M ($M = 0$, $M = 0.05$ and $M = 0.1$). Two different injected modes are tested:

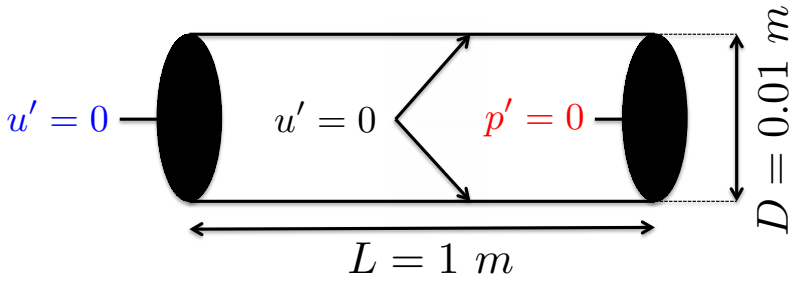

Figure 9.4: 3D longitudinal configuration.

- **from AVSP:** the acoustic mode is constructed from a Helmholtz simulation performed with the code AVSP, assuming a zero Mach number.
- **from analytical theory:** the acoustic mode is computed using a 1D theory taking into account the axial mean flow. Taking into account the boundary conditions $u' = 0$ at $x = 0$ and $p' = 0$ at $x = L$, the pressure and velocity fluctuations read at the initial time $t = 0$:

$$p'(x, t = 0) = P_0 \cos\left(\frac{\pi x}{2L}\right) \cos\left(\frac{\pi x M}{2L}\right) \tag{9.8}$$

$$u(x, t = 0) = \frac{P_0}{\rho_0 c_0} \sin\left(\frac{\pi x}{2L}\right) \sin\left(\frac{\pi x M}{2L}\right) \tag{9.9}$$

  which correspond to an acoustic mode satisfying $\hat{u}(x = 0) = 0$ and $\hat{p}(x = L) = 0$ with a frequency $Re(f) = \frac{c_0}{4L}(1 - M^2) \approx 86\ Hz$ and $Im(f) = 0$ (see H for details about longitudinal modes with a constant mean flow).

An additional test case is provided in Section 9.4 (Fig. 9.5 - d) to further study the impact of convective effects on the injected acoustic mode, in particular by adding turbulence naturally present in LES of complex industrial gas turbines.

9.3.2 AMT results on the laminar configuration

First the AMT methodology is applied to cases $M0$, $M0.05$ and $M0.1$ (Fig. 9.4) with the two mode injection types: i.e. the acoustic mode is obtained by a Helmholtz solver (AVSP) or by a 1D theory at non-null Mach number and is injected with an initial amplitude of 800 Pa (i.e. $p'/\bar{p}_0 < 1\%$ to satisfy the linear acoustic assumption). Figure 9.6

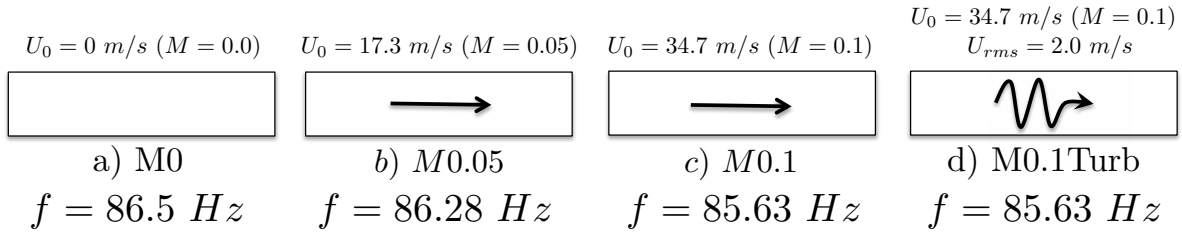

Figure 9.5: Longitudinal test cases: a) no mean flow, b) and c) mean flow with $M = 0.05$ and $M = 0.1$ and d) mean flow $M = 0.1$ with turbulent injection ($U_{rms} = 2\ m/s$). The theoretical frequency of each case is also indicated (expressions are given in Tab. H.1).

displays Fourier transforms of the pressure signal at the center point of the pipe ($x = 0.5\ m$). For low Mach numbers tested in this work ($M = 0$ and $M = 0.05$), the two injection types create initial modes which are close to the true solution: the LES exhibits only one mode. However for higher Mach numbers ($M = 0.1$), the solution at zero Mach number provided by AVSP is too far from the true solution and small spurious modes appear as shown in the spectrum (Fig. 9.6, right). For simple cases, this drawback can be avoided by injecting an acoustic mode closer to the Mach-dependent solution, for instance a 1D theory at non-zero Mach number (Eqs. (9.8) and (9.9)). In this case, the acoustic mode is correctly injected with no spurious mode (Fig. 9.6, `---`).

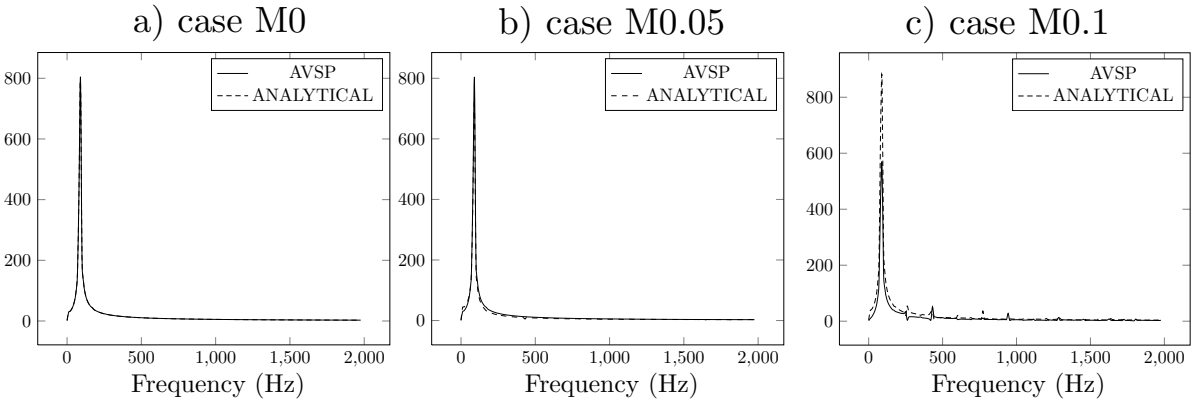

Figure 9.6: FFT of the pressure signal at the location $x = 0.5\ m$ for the three cases with $M = 0$ (left), $M = 0.1$ (middle) and $M = 0.2$ (right). Two different modes have been injected: —— : AVSP (solution at zero Mach number) and `---` : 1D theory taking into account the axial mean flow (Eqs. 9.8) and 9.9).

To further validate AMT results, frequencies and growth rates associated to each case are extracted. Dynamic Mode Decomposition (Schmid, 2010) is used here since FFT suffers from a low frequency resolution (here $\Delta f = 10\ Hz$ for the 100 ms-long pressure signals) compared to the subtle Mach effects on frequency (1 Hz at $M = 0.1$). Analytical expressions for frequency and growth rate at non-null Mach number are provided in Appendix H (Tab. H.1): the growth rate is null for all Mach numbers and the frequency depends on the square of the Mach number. Table 9.1 summarizes the comparison between the analytical and AMT frequencies and growth rates with the two different initialization: an acoustic mode computed by AVSP (null-Mach number assumption) or

by theory.

	Frequencies		
	$M = 0$	$M = 0.05$	$M = 0.1$
Theory	86.5 Hz	86.28 Hz	85.63 Hz
AMT-Theory	86.46 Hz	86.33 Hz	85.65 Hz
AMT-AVSP	86.46 Hz	86.25 Hz	85.65 Hz

	Growth rates		
	$M = 0$	$M = 0.05$	$M = 0.1$
Theory	0 s^{-1}	0 s^{-1}	0 s^{-1}
AMT-Theory	8.10^{-2} s^{-1}	-6.10^{-3} s^{-1}	-9.10^{-3} s^{-1}
AMT-AVSP	6.10^{-2} s^{-1}	-2.10^{-2} s^{-1}	-5.10^{-5} s^{-1}

Table 9.1: Comparison of frequencies (top) and growth rates (bottom) obtained by theory (Appendix H) and AMT initialized by theory or AVSP, showing an absolute error of 10^{-2} on both frequencies and growth rates.

These three test cases prove the AMT capability to impose an acoustic mode as an initial condition for the LES solver. On simple longitudinal laminar configurations, AMT provides estimation of frequencies and growth rates with an absolute error of the order of 10^{-2} Hz. Thus, solutions provided by zero Mach-number codes like Helmholtz solvers are properly injected for low mean flows, i.e. $M < 0.1$, which corresponds to many applications encountered in modern gas turbines.

9.4 AMT validation on a turbulent configuration

In addition to the laminar cases investigated previously where an acoustic mode was added to a laminar flow (Fig. 9.5), a spatially decaying turbulent test case is studied in this section. Turbulence is naturally present in LES of complex industrial annular chambers. Up to now, sound propagation in a turbulent pipe was investigated either by forcing an acoustic wave at the inlet or by pulsating the solid boundaries (Comte *et al.*, 2006; Agarwal & Bull, 1989). AMT allows a third method which is to superimpose an acoustic cavity mode (here the first longitudinal mode at 86.5 Hz) on the baseline turbulent flow to investigate two reciprocal effects: (1) Turbulence can interact with the acoustic mode and trigger higher harmonics and (2) Acoustic can affect the turbulence production and consequently impact the energy turbulence spectrum. For this case (Fig. 9.7), the acoustic boundary conditions for the channel correspond to $u' = 0$ at the inlet and (imposed velocity) and $p' = 0$ at the outlet (imposed pressure).

In this chapter, a fine mesh is used containing 5.5 million cells (compared to 362,000 for the laminar case) which corresponds to a cell size $\Delta x = 1$ mm and ensure $\lambda_e \gg \Delta x$. Turbulence is injected at the duct inlet to study its interaction with the acoustic mode: a Passot-Pouquet spectrum (Passot & Pouquet, 1987) is injected via the inlet boundary

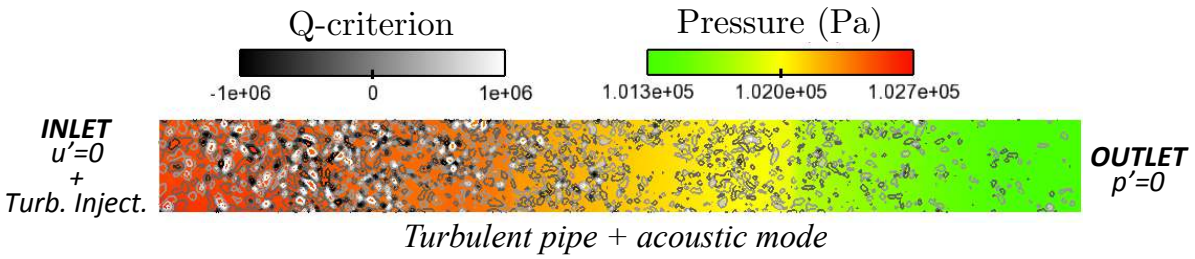

Figure 9.7: 3D Turbulent pipe with an acoustic mode injected by AMT. Boundary conditions are imposing a velocity node at the inlet ($u' = 0$) and a pressure node ($p' = 0$) at the outlet.

condition using the Kraichnan-Celik methodology (Smirnov *et al.*, 2001) and the NSCBC approach (Guezennec & Poinsot, 2009):

$$E(k) = 16\frac{U_p^2}{k_e}\left(\frac{k}{k_e}\right)^4 e^{-2\left(\frac{k}{k_e}\right)^2} \tag{9.10}$$

where E is the energy spectrum, k is the wavenumber, $k_e = 2\pi/\lambda_e$ is the most energetic wavenumber. The most energetic wavelength is $\lambda_e = D/3 \approx 0.03\ m$ and $U_p = U_{rms} \sim 2.0\ m/s$ is the turbulent velocity. For the Kraichnan-Celik methodology, $N = 1000$ modes are used and a cut-off length corresponding to twice the size of the largest cell edge on the inlet patch ($L_c = 2\max(\Delta x)$) is imposed to enforce the Shannon theorem.

Two-points correlation functions (longitudinal $f(r)$ and transverse $g(r)$ where r is the distance between two points) are extracted from the simulation[2] before AMT (i.e. no acoustic mode) and compared to the theory ($f_{th}(r)$ and $g_{th}(r)$) to check the turbulence injection:

$$\begin{aligned} f_{th}(r) &= e^{-\frac{1}{8}(k_e r)^2} \\ g_{th}(r) &= \left(1 - \frac{(k_e r)^2}{8}\right) e^{-\frac{1}{8}(k_e r)^2} \end{aligned} \tag{9.11}$$

Figure 9.8 shows that correlations functions in the LES (——) are close to theory (---). The oscillations for larger length scale are due to statistical convergence. The ratio of the longitudinal and transverse Taylor micro-scales $\lambda_f/\lambda_g \approx 1.409$ is in good agreement with the theoretical value $\lambda_f/\lambda_g = \sqrt{2} \approx 1.414$. Turbulence in the case M0.1Turb is visualized in Fig. 9.9 using the Q-criterion (blue: negative and red: positive): it illustrates the injected vortices decaying in the longitudinal direction.

After $t_0 = 100\ ms$ of simulation, an acoustic quarter-wave mode at 86.5 Hz is injected using AMT in the turbulent flow. Figure 9.10 shows the Fourier transform of the pressure signal at $x = 0.5\ m$ of the case $M01Turb$ compared to the laminar case (case $M0.1$, Fig. 9.5). Compared to the laminar case, two eigenmodes at 430 Hz and 770 Hz are triggered due to the interaction between acoustics and turbulent flow. Time-evolution of pressure (Fig. 9.10, right) reveals the initial acoustic mode ($t \approx t_0$) is only weakly

[2]Correlation functions are extracted using a probe at a location x which gives temporal velocity variations $\vec{u'}(t)$. Therefore, these correlation functions rely on the Taylor assumption: $\frac{\partial}{\partial t} \approx -u_0 \frac{\partial}{\partial r}$

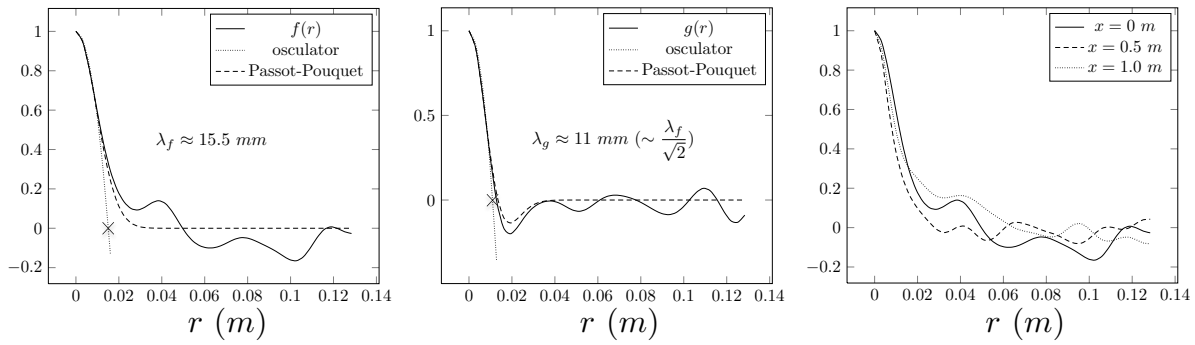

Figure 9.8: Longitudinal (left) and transverse (middle) correlations functions extracted from LES without AMT (i.e. no acoustic mode) at $x = 0m$ (inlet) and comparison with the Passot-Pouquet spectrum (Eq. 9.11, `---`). The intersection of the osculator parabola (⋯⋯) with the abscissa gives an estimation of the Taylor micro-scale λ_f and λ_g ($\times$). Correlation function at several longitudinal locations are also displayed (right).

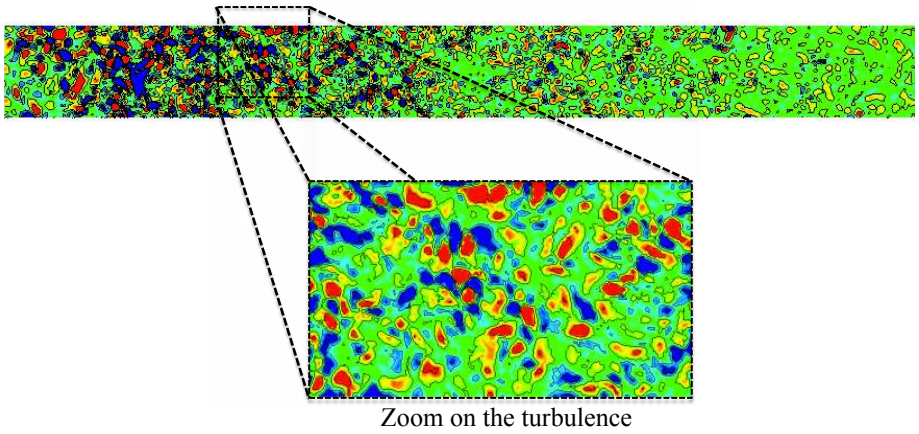

Figure 9.9: Longitudinal cut and zoom on turbulence displayed by Q-criterion in the case M0.1Turb with no acoustic mode.

affected by turbulence. However, after a few milliseconds ($t \gg t_0$), other modes with higher frequencies appear in the pressure signal which suggests that turbulent motion can trigger acoustic modes.

The triggered eigenmodes observed in the Fourier transform of pressure for the case $M0.1Turb$ are post-processed (Fig. 9.12, right) using both energy spectrum (Fig. 9.11) Fast Fourier Transform (FFT) and Dynamic Mode Decomposition (DMD). First, the energy spectra based on the axial velocity fluctuations u' are displayed for the case without mode injection (left) at three different locations: the inlet (—— , $x = 0\ m$), just after the inlet (`---` , $x = 0.2\ m$) and at the outlet (⋯⋯ , $x = 1\ m$). They show that turbulence is properly injected in the computational domain at the inlet. Turbulent vortices are then convected downstream. As expected, the energy level observed at $x = 0.2\ m$ is similar to the energy injected at the inlet because of the large turbulent Reynolds number ($Re_t = 15,000$ based on $L_{11} \simeq 0.4\lambda_e$ and $u_{rms} = U_p = 2\ m/s$). However, at the outlet ($x = 1\ m$), turbulent dissipation has decreased the energy level of one order of magnitude

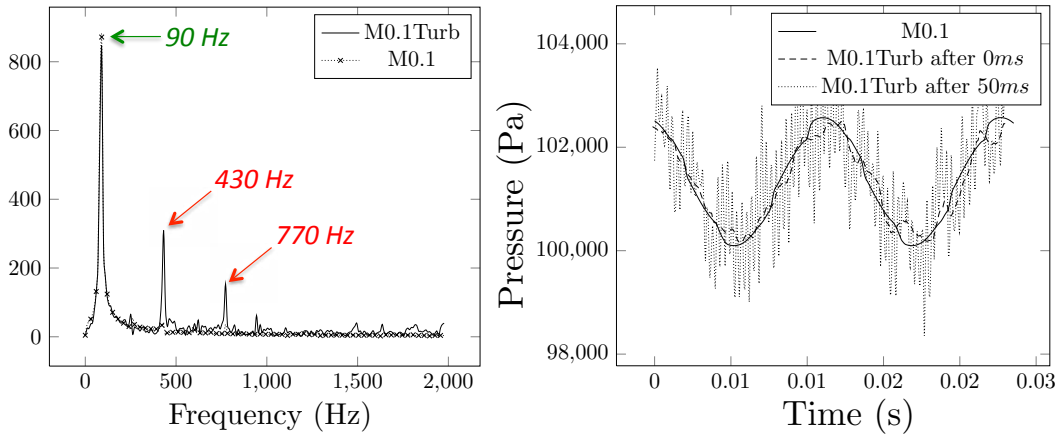

Figure 9.10: Fourier transform (left) and time-evolution (right) of the pressure signal at $x = 0.5m$ in the case $M0.1Turb$ compared to the laminar case $M0.1$. Initially turbulence weakly affects the acoustic mode (1- ▬▬ , just after AMT at $t - t_0 = 0ms$) but after a few milliseconds (2- ····· for $t - t_0 \approx 50\ ms$) turbulence triggers higher frequency modes.

as shown in Fig. 9.9. Then, the same post-processing tool is applied on the turbulent case with the injected acoustic mode at 86 Hz. It is interesting to notice that the inlet spectrum is not modified which is normal since the boundary condition $u'_{ac} = 0$ imposes no acoustic velocity fluctuations. It also suggests that no spurious oscillations are generated at the inlet. However, downstream of the inlet, the turbulence spectra are highly perturbed: (1) the acoustic mode at 90 Hz is observed (The FFT frequency resolution is $\Delta f = 10\ Hz$: the injected mode at 86 Hz is therefore captured at 90 Hz) and is maximal at the outlet because of the half-wave structure of the mode and (2) the classic turbulent dissipation at large frequencies is altered. These results reveal that the acoustic energy of the longitudinal mode at 86 Hz feeds the turbulence motion.

To further analyze these non-linear behavior, the pressure LES fields are also post-processed to identify modes triggered observed in Fig. 9.10. FFT and DMD results (9.12, right) are compared with the acoustic eigenmodes of the system computed by a Helmholtz solver (no mean flow and no turbulence): Fig. 9.12 (left) shows that modes observed at 86 Hz, 430 Hz and 770 Hz in Fig. 9.10 are acoustic eigenmodes of the configuration: a non-linear interaction between the longitudinal mode and the turbulence has triggered other eigenmodes of the system.

Even though this was not presented here, this example shows that AMT can be an efficient technique to study mechanisms through which turbulent fluctuations redistribute acoustic energy from one mode to others as suggested for example by Noiray *et al.* (2011) to explain mode switching in annular chambers.

9.5 Conclusion

Limitations of linear methods to study instabilities in combustion systems are a usual controversial question: this chapter presents a method to verify the quality of linear

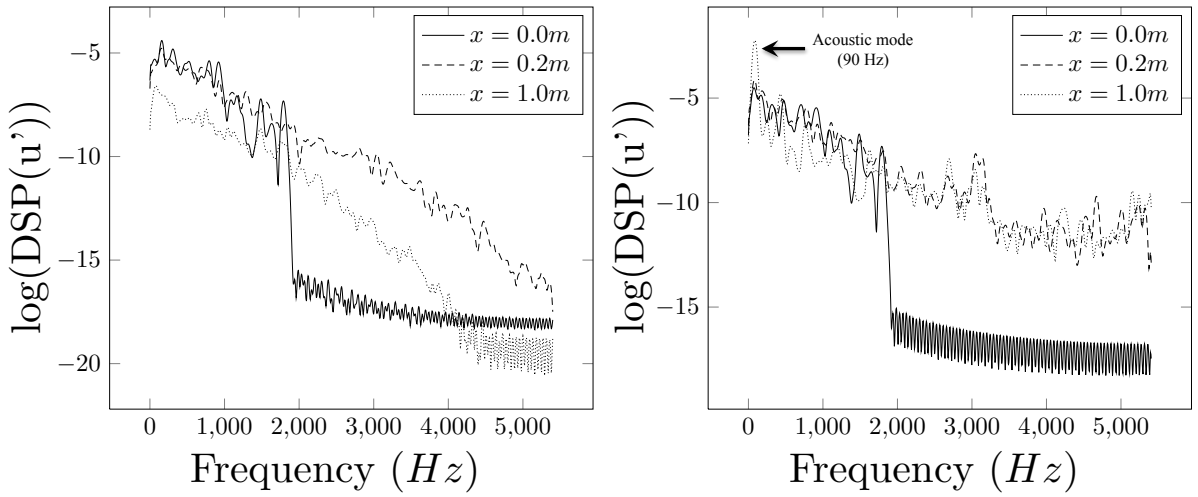

Figure 9.11: Energy spectrum on the axial velocity fluctuations u' for the turbulence case $M0.1TURB$ without (left) and with (right) an acoustic mode at 90 Hz injected by AMT. Probes are located at three locations: the inlet (——— , $x = 0$ m), just after the inlet (- - - , $x = 0.2$ m) and at the outlet (····· , $x = 1$ m).

predictions and theories for combustion instabilities presented in Part I of this thesis by using them as initial solutions of a LES or DNS solver which do not have the limitations due to the linear and low-Mach assumptions used in acoustic solvers. This approach (called AMT for Acoustic Mode Triggering) uses the results of a Helmholtz solver (at zero Mach number) or of theory (at zero or non-zero Mach number) as an initial condition of a LES to focus on this single mode growth. Such an approach provides the numerical estimation of the damping/growth rate of the injected mode and its limit cycle as well. In this chapter, the methodology is validated on longitudinal laminar configurations with various mean flows. An additional test case is presented where turbulence is injected to study its impact on the acoustic mode which is still an open topic today. Results show that AMT is able to reproduce non-linear behaviors such as acoustics at non-null Mach numbers. When turbulence is injected, non-linear interactions between the acoustic mode and the turbulence are observed and lead to harmonics generation.

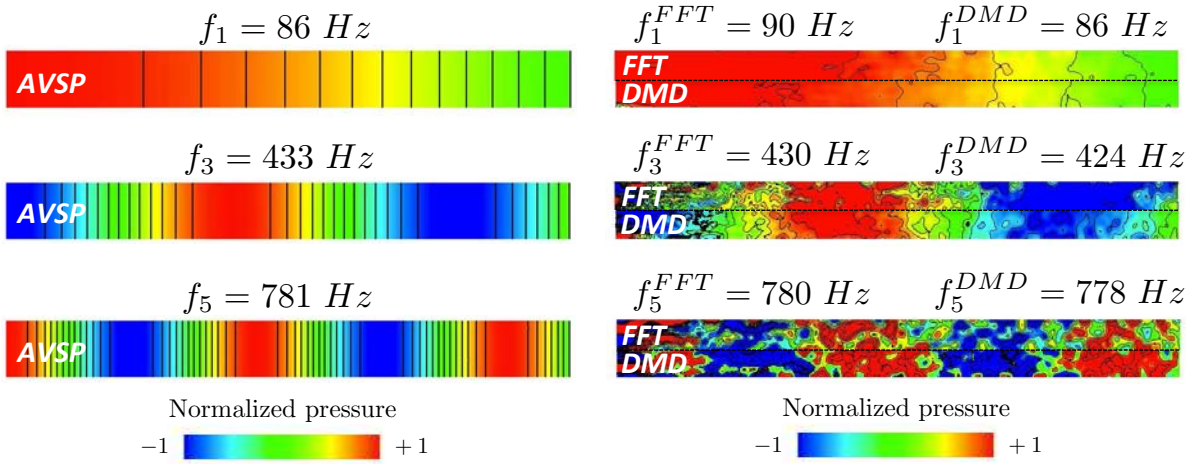

Figure 9.12: Eigenmodes obtained by the Helmholtz solver (left) and Fourier Transform (FFT) and Dynamics Mode Decomposition (DMD) of the $M0.1Turb$ case (right).

Chapter 10

Study of acoustic mode dynamics using Acoustic Mode Triggering (AMT): application to annular configurations

Contents

10.1 Introduction 218

10.2 AMT applied on a simple annular configuration 219

10.2.1 Objectives and annular setup 219

10.2.2 Large eddy simulations 220

10.2.3 Helmholtz simulations 222

10.3 AMT results on the annular configuration 222

10.3.1 The symmetric case (M0H0) 223

10.3.2 Flow symmetry breaking using a mean swirl motion (case M0.1H0) 223

10.3.3 Geometry Symmetry breaking using one Helmholtz resonator (case M0H1) 227

10.3.4 Symmetric case using two Helmholtz resonators (case M0H2) . 228

10.4 Mode dynamics analysis: time-evolution of the azimuthal mode nature 230

10.5 Conclusion 232

A new methodology combining acoustic simulations and LES, called AMT, was developed in the previous chapter and validated on laminar and turbulent longitudinal configurations. This tool is applied in this chapter on a simplified annular combustor to study effects of both FS and GS breaking. First, flow symmetry breaking is investigated by injecting an acoustic mode in an annular chamber with a mean azimuthal flow. As expected from theoretical results presented in Chapter 3, the initial mode is split into two distinct components leading to a warble phenomenon at low frequency. The mode structure of these two components is identified by a FFT as rotating, i.e. standing but rotating slowly at the mean flow velocity. Then GS breaking is studied by introducing Helmholtz dampers with various patterns distributed along the azimuthal direction. The dynamics of the resulting mode behavior is analyzed by changing the nature of the injected mode, from standing to spinning. It shows that breaking symmetry fixes the mode structure of the limit cycle for non-symmetric cases. However, for axisymmetric cases, the mode structure is determined by the initial state only. This application is a promising approach to study azimuthal modes in a time-domain with realistic damping mechanisms.

10.1 Introduction

The previous chapter described a new methodology called AMT to study acoustic modes in geometries with a mean flow and complex damping mechanisms. This tool was validated on laminar and turbulent longitudinal configurations. However, in modern gas turbines, thermo-acoustic modes often take the form of azimuthal modes and need to be investigated. The nature and stability of these modes have been the topic of numerous studies since the pioneering works of industrial companies like Siemens (Krebs *et al.*, 2002) or Alstom (Noiray *et al.*, 2011)but it is still an open topic today: high fidelity simulations applied to full annular configurations (Staffelbach *et al.*, 2009; Wolf *et al.*, 2012) (Fig. 9.1, right) show that azimuthal modes can randomly change in nature, evolving from spinning to standing structures at random instants. In parallel, new annular experiments developed at TU-Berlin (Moeck *et al.*, 2010; Gelbert *et al.*, 2012), Cambridge (Worth & Dawson, 2013*b*,*a*) and EM2C (Bourgouin *et al.*, 2013) prove that breaking symmetry by non-homogeneous power distribution of heating grids acting like flames (Moeck *et al.*, 2010), alternating co/counter-rotating swirlers (Worth & Dawson, 2013*b*,*a*) or distributing baffles along the annular chamber (Dawson & Worth, 2014), strongly affects the mode nature.

To complement LES and experiments, Noiray *et al.* (2011) have shown analytically on a simple annular chamber that non-linearities can also affect the limit cycle by fixing the nature of its two basic mode components. Ghirardo & Juniper (2013) have extended this model to take into account transverse velocity effects in the Flame Describing Function (Noiray *et al.*, 2008) describing the non-linear flame behavior. These non-linear theories rely on simple configurations where plenum, burners and mean flow have been removed. Yet, recent theories (Bauerheim *et al.*, 2014*a*,*e*) developed in Chapter 2 and 3

demonstrates that some linear effects cannot be ignored: breaking symmetry either by adding an azimuthal mean flow or by mixing burner types can also control the structure of the azimuthal components similarly to non-linear flame responses. However, all these theories fail to predict the ratio between these two components and new methodologies still need to be developed to study azimuthal modes.

10.2 AMT applied on a simple annular configuration

10.2.1 Objectives and annular setup

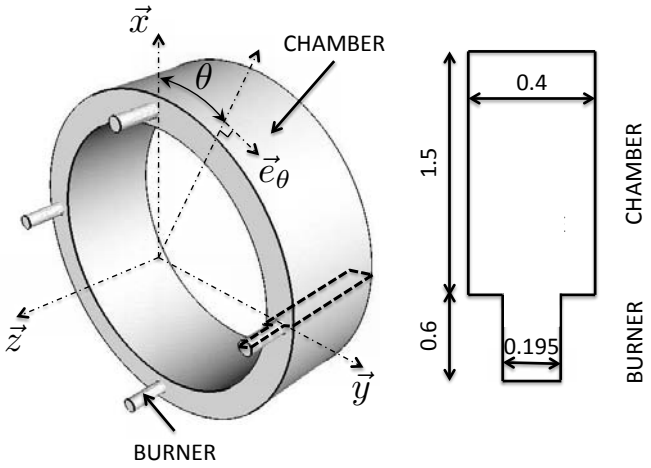

a) 3D view of the BC configuration b) Axial cut

Figure 10.1: 3D view (left) and axial cut (right) of the simplified configuration with $N = 4$ burners.

AMT is applied first on a simplified annular configuration where the rotating symmetry is broken either by FS or GS mechanism. Already studied analytically (Bauerheim *et al.*, 2014*e*) and experimentally (Moeck *et al.*, 2010; Worth & Dawson, 2013*b*,*a*), the nature and dynamics of azimuthal modes without combustion using LES can indicate that non-linearities on the flame behavior is not necessarily the only feature controlling the mode structure. The baseline configuration is a four-burner annular chamber (Fig. 10.1) without inlet, outlet or flame (no combustion, iso-thermal cases) since only geometry (Helmholtz resonators) and mean flow effects on injected azimuthal modes are investigated in this PhD:

1) **Flow Symmetry (FS) breaking:** AMT has been validated for small Mach numbers ($M < 0.1$) in Section 9.3 on longitudinal configurations and is now applied on a simple 360° case. To simplify the configuration, no inlet or outlet is introduced in the configuration. The mean azimuthal flow is therefore injected using the initial condition and walls are treated slip to minimize hydrodynamic perturbations and maintain a constant azimuthal Mach number M_θ during the simulation. Two different baseline flows are imposed as initial conditions:

a - *Quiescent flow:* The flow has no velocity ($\vec{V} = \vec{0}$) at atmospheric pressure ($P = 1013025\ Pa$) and the temperature corresponds to burnt gases ($T = 1800\ K$).

b - *Azimuthal mean flow:* An homogeneous azimuthal swirl motion (Eq. (10.1)) corresponding to $M_\theta = 0.1$ is introduced in the annular chamber to break its symmetry while no velocity is present in the surrogate burners (i.e. burners with no inlet and no flame).

$$\vec{V} = c^0 M_\theta \vec{e}_\theta = c^0 M_\theta \left(-\sin(\theta)\vec{e}_x + \cos(\theta)\vec{e}_y\right) \tag{10.1}$$

2) **Geometry Symmetry (GS) breaking:** Helmholtz resonators (Fig. 10.2) are introduced in the configuration with no mean flow to break symmetry and damp the injected azimuthal mode: both the dynamics (evolution of the nature of the azimuthal mode with time computed by the JAWA methodology presented in Chapter 8.4.2) and the damping rate α will be numerically measured. The dimensions V, L and A of the resonators are adjusted to damp the injected acoustic mode at $f^0 = 64\ Hz$:

$$f^0 = \frac{c^0}{2\pi}\sqrt{\frac{A}{VL^c}} \tag{10.2}$$

where $V = 0.125\ m^3$ is the volume of the resonator, $A = 0.00785\ m^2$ its surface and $L^c = L + \frac{8d}{3\pi} = 0.3\ m$ the corrected length depending on the diameter $d = \frac{\pi d^2}{4}$.

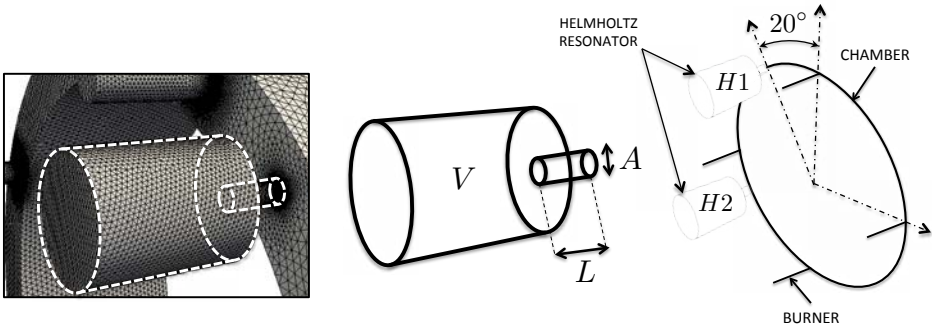

a) Mesh b) Sketch c) Localization

Figure 10.2: A) Mesh, b) sketch and c) localization of the two Helmholtz resonators introduced in the LES domain.

The different cases studied in this chapter are summarized in Fig. 10.3 and the AME methodology in Fig. 10.4. AMT requires both LES and Helmholtz simulations to be performed. The specificities of these two codes in the context of AMT applied on a annular combustor with FS and GS breaking are briefly presented in the following.

10.2.2 Large eddy simulations

Large Eddy Simulation (LES) of compressible flow is widely recognized as an accurate method (Poinsot & Veynante, 2011) to investigate acoustics in complex combustor configurations (Wolf *et al.*, 2012; Sengissen *et al.*, 2007; Fureby, 2010; Kuenne *et al.*, 2011).

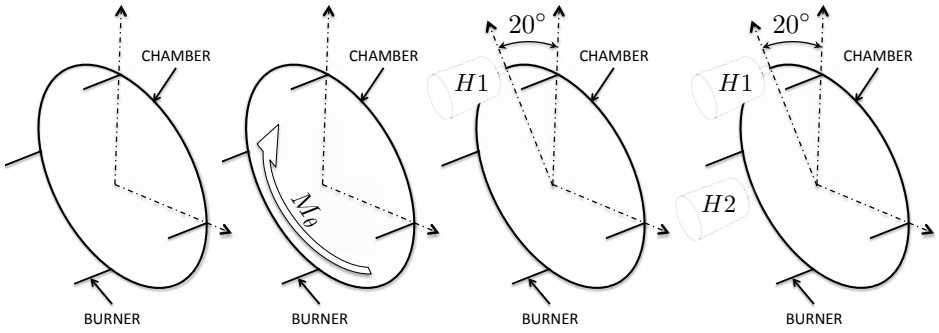

Figure 10.3: Four test cases studied: a) Quiescent flow without Helmholtz resonator, b) Swirl motion ($M_\theta = 0.1$) without Helmholtz resonator, c) Quiescent flow with one Helmholtz resonator and d) Quiescent flow with two Helmholtz resonators.

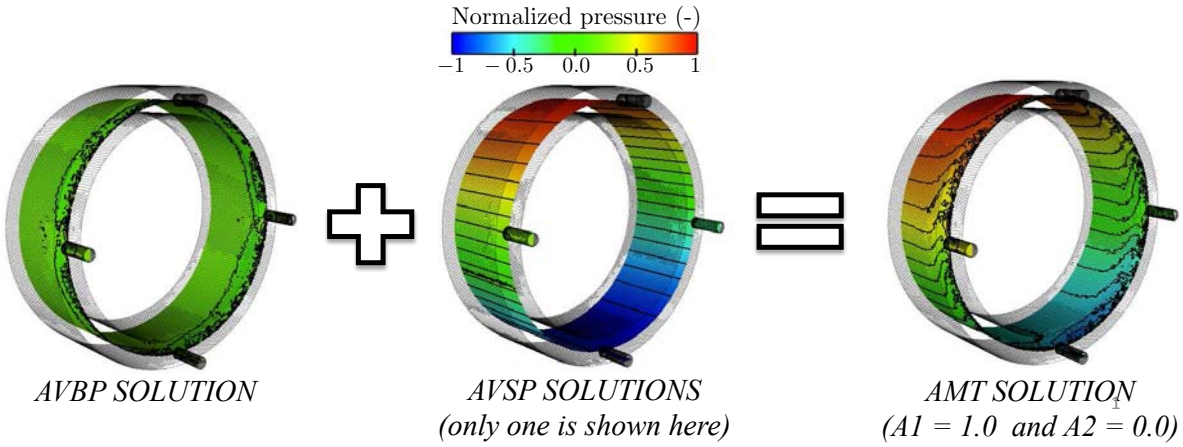

Figure 10.4: AMT methodology for annular combustors: a stable baseline flow is computed by LES (left). An acoustic solution is also computed using an Helmholtz solver (middle) and is combined with the LES baseline flow to provide a new initial solution for the LES solver (right).

To study the effect of Helmholtz resonators and mean flow on azimuthal modes dynamics, AVBP is employed again here, using a third-order spatial and temporal scheme (TTGC, Moureau *et al.*, 2005) to accurately propagate acoustic waves. Boundary conditions use the NSCBC approach (Poinsot *et al.*, 1992) to ensure reflecting/non-reflecting boundary conditions (Selle *et al.*, 2004*b*). The mean flow is introduced via the initial condition. For the case M0.1H0, a mean swirl motion (Eq. (10.1)) is imposed in the annular chamber and no velocity in the surrogate burners. The burner/chamber junctions are treated as no slip walls to avoid ill-posed problems at corners. Other walls are treated as slip walls to minimize pressure drops and to maintain the imposed mean flow as constant as possible. The swirl decay remains very small during the establishment of the acoustic cycle (typically the azimuthal mean velocity decreases by 5%). Prior to the application of the AMT methodology (Section 9.2), non-reflecting NSCBC boundary conditions (Poinsot *et al.*, 1992) are used to obtain a well established baseline flow and eliminate potential acoustic waves generated during this initialization phase. The 3D instantaneous LES

conservative variables (density ρ_{LES}, velocity $\rho\vec{V}_{LES}$ and total energy ρE_{LES}) are then extracted to be employed as a baseline flow for Helmholtz simulations (Section 10.2.3) and the application of AMT.

10.2.3 Helmholtz simulations

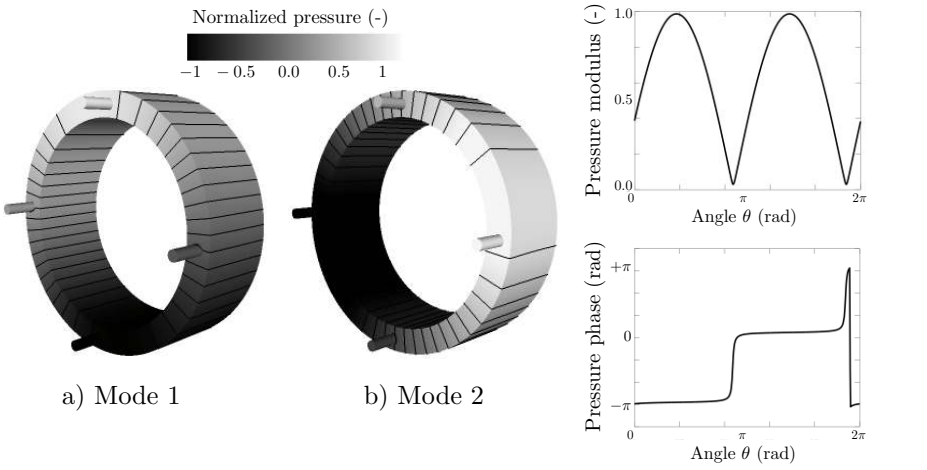

a) Mode 1 b) Mode 2

c) Pressure modulus and phase

Figure 10.5: a) and b) Normalized pressure $P_{ac} = \|\hat{P}\|\cos(\phi_p)$ fields and iso-contours for the two azimuthal modes obtained at 64 Hz reconstructed from the two outputs of the acoustic solver: c) $\|\hat{P}\|$ the pressure modulus and ϕ_p the pressure phase.

The full 3D acoustic solver called AVSP (Nicoud *et al.*, 2007) is used first to predict the azimuthal acoustic mode of the annular chamber. AVSP solves the eigenvalues problem issued from a discretization on unstructured meshes (with 1.9 millions cells) of the wave equation. Infinite impedances (corresponding to $\overrightarrow{V_{ac}} \cdot \vec{n} = 0$ where $\vec{n}$ is the wall normal) are applied on walls. Mean density and sound speed fields are extracted from the LES simulation and used as a baseline flow.

This study focuses on the first azimuthal modes of an annular chamber with four burners: as shown in Fig. 10.5, two standing modes at 64 Hz are predicted by the acoustic solver. This is a usual result at zero Mach number where the first azimuthal mode frequency is degenerate: the two modes can be combined to generate any mode structure (standing, spinning or mixed (Krebs *et al.*, 2002; Poinsot & Veynante, 2011; Evesque & Polifke, 2002)).

10.3 AMT results on the annular configuration

The AMT methodology described in Figs. 9.2 and 10.4 is then applied on the four symmetric and non-symmetric configurations presented in Fig. 10.3. The test matrix for annular configurations is summarized in Tab. 10.1. For each case, the injected acoustic mode is standing with an amplitude $\|\hat{p}\| \approx 500\ Pa$.

Cases	M_θ	Resonators	Symmetry
M0H0	0	0	Symmetric
M0.1H0	0.1	0	FS breaking
M0H1	0	1	GS breaking
M0H2	0	2	Symmetric

Table 10.1: Summary of the test cases performed on a simplified 360° annular configuration where symmetry is broken either by FS or GS mechanism by the introduction of a mean azimuthal flow or by Helmholtz resonators.

10.3.1 The symmetric case (M0H0)

First, the symmetric case without Helmholtz resonator and swirl motion is investigated (Fig. 10.3-a). A standing mode ($\alpha_1 = 500\ Pa$ and $\alpha_2 = 0\ Pa$ in Eq. (9.1)) is triggered using the AMT methodology. In this condition, the Helmholtz solver provides a solution which must match exactly the Navier-Stokes equation because the Mach number, as well as the pressure perturbation amplitude, are small. Figure 10.6 shows the result of 80 ms of the LES simulation: the amplitude remains constant, no damping is observed. The C-indicator (Wolf *et al.*, 2012; Worth & Dawson, 2013*b*) ($C(t) = \frac{1}{N}\sum_{k=1}^{N} p_k(\theta_k, t)e^{j\theta_k}$) computed from $N = 4$ equi-distributed pressure probes indicates that the mode remains standing (Appendix I). For this case, AMT performs exactly as expected.

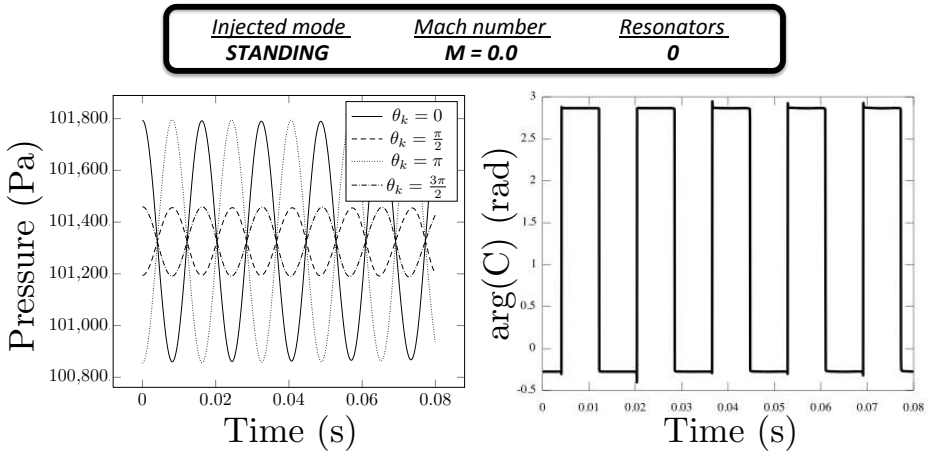

Figure 10.6: Pressure signal for the case $M0H0$ at four azimuthal locations (left) and phase of the C-indicator (right).

10.3.2 Flow symmetry breaking using a mean swirl motion (case M0.1H0)

A mean azimuthal flow is then introduced into the LES domain corresponding to $M_\theta = 0.1$ to break the axi-priodicity of the annular chamber. Recently, linear theory (Bauerheim *et al.*, 2014*e*) has shown that such a swirl motion can affect the azimuthal mode by

splitting its two components into two distinct spinning modes with different yet close frequencies f_1 and f_2 such that:

$$f_2 - f_1 = \Delta f = \frac{c^0 M_\theta}{L_c} = \frac{2}{T_c} = 12.7\ Hz \tag{10.3}$$

where $c^0 = 850\ ms^{-1}$ is the mean sound speed, $L_c = 6.7\ m$ is the half-perimeter of the annular chamber and T_c is the period of the mean flow rotation at the convective speed $u^0 = c^0 M_\theta$.

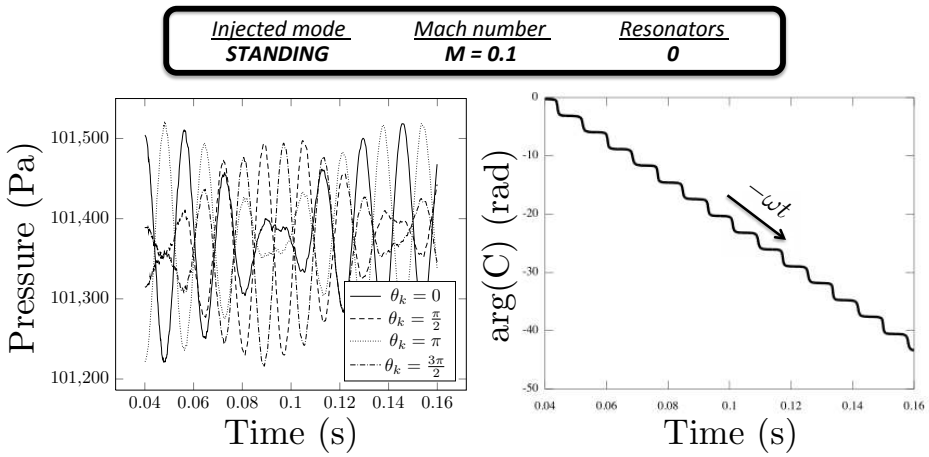

Figure 10.7: Pressure signal for the case $M0.1H0$ at four azimuthal locations (left) and phase of the C-indicator (right).

Pressure signals at different azimuthal locations θ_k (Fig. 10.7, left) show that the mode is neither standing nor spinning. The phase of the C-indicator (Fig. 10.7, right) indicates that the mode is rotating, i.e. the mode structure is standing but rotates slowly at the mean convected speed $u^0 = c^0 M_\theta$ as already observed in the full 360° LES of Wolf *et al.* (2012). This warble mode (i.e. a mode at very low frequency produced by two modes with different yet close frequencies) appears here on both the time-evolution and the Fourier analysis (Figs. 10.8 and 10.9). The measured warble frequency $f_w = \frac{1}{T_c} = \frac{\Delta f}{2} \approx 5\ Hz$ (where Δf is defined in Eq. (10.3)) leads to an estimated rotation velocity $u^0 = 2L_c f_w \approx 67\ m/s$. This measured rotation velocity is smaller than the imposed azimuthal velocity $u^0 = 85\ m/s$ (Eq. (10.3)) due to the FTF resolution (providing f_w at $\pm 5\ Hz$) and the difficulty to maintain a constant azimuthal mean flow in the chamber.

FFT (Fig. 10.8) and DMD[1] (Fig. 10.9) of pressure signals can be compared to the symmetric case with a quiescent baseline flow: at zero Mach number ($M_\theta = 0$, left) the two components of the azimuthal modes are degenerate and share the same frequency $f = 62\ Hz$. Adding a mean swirl motion ($M_\theta = 0.1$, right) splits the azimuthal mode into two distinct components at $f^- = 55\ Hz$ and $f^+ = 65\ Hz$.

[1]The warble mode has been filtered out in the DMD post-processing to highlight the splitting between the two components at 56.6 Hz and 66.2 Hz.

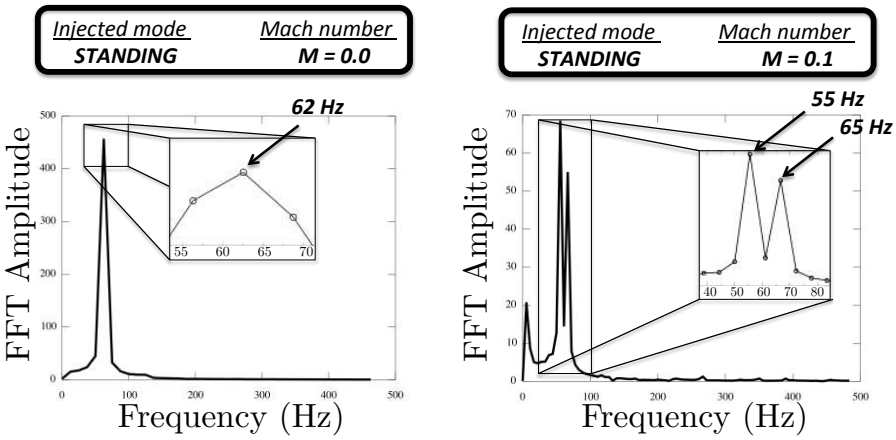

Figure 10.8: Highly resolved FTF ($\delta f = 5\ Hz$) of pressure for cases $M0H0$ (left) and $M0.1H0$ (right). At zero Mach number ($M_\theta = 0$) the two components are degenerate and share the same frequency $f = 62\ Hz$. With a mean swirl motion ($M_\theta = 0.1$), the azimuthal mode is split into two components at $f^- = 55\ Hz$ and $f^+ = 65\ Hz$ and a warble mode appears at $f_w = 10\ Hz$.

To analyze the mode structure of the two components, a Fourier Transform is performed on the whole pressure field for both the symmetric ($M0H0$) and non-symmetric ($M0.1H0$) cases. Only one component is found at $M_\theta = 0$ ($f = 62\ Hz$) while two components are obtained at 55 Hz and 65 Hz for $M_\theta = 0.1$. The associated pressure modulus and phase fields (Fig. 10.10) confirm that with no mean flow the mode is degenerate (the two components have the same frequency and structure) and remains standing (Fig. 10.10, left). The introduction of a bulk swirl however splits the mode into two spinning modes as predicted by linear analysis (Bauerheim *et al.*, 2014*e*): the co-rotating mode (Fig. 10.10, right) and a counter-rotating mode (Fig. 10.10, middle).

Indeed, adding two spinning modes with different frequencies $f^\pm = \frac{c^0(1\pm M_\theta)}{2L_c}$ but same amplitudes ($P_1 = P_2$) produces the rotating mode observed in this LES similarly to Staffelbach *et al.* (2009) and Wolf *et al.* (2012):

$$P = P_1 \cos\left(-\theta + 2\pi f^0 t + \frac{\pi c^0 M_\theta}{L_c} t\right) + P_2 \cos\left(\theta + 2\pi f^0 t - \frac{\pi c^0 M_\theta}{L_c} t\right) \quad (10.4)$$

$$= 2P_1 \cos(2\pi f^0 t)\cos(\theta - 2\pi t/T_c) \quad (10.5)$$

where $f^0 = \frac{c^0}{2L_c} \approx 62\ Hz$ is the frequency of the mode with no mean flow and $T_c = \frac{2L_c}{c^0 M_\theta} \approx 157\ ms$ is the period of rotation at the convective speed $c^0 M_\theta$ corresponding to a warble mode at the frequency $f_w = 1/T_c \approx 6\ Hz$.

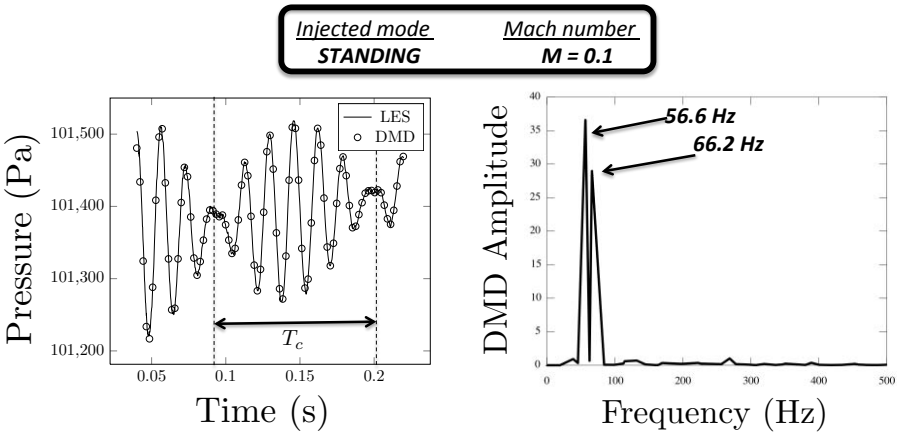

Figure 10.9: Time evolution of the pressure signal at $\theta_k = 0$ from LES and DMD reconstruction (left) and DMD spectrum (right) where low frequencies (below 20 Hz) have been filtered to highlight the two split components at 56.6 Hz and 66.2 Hz.

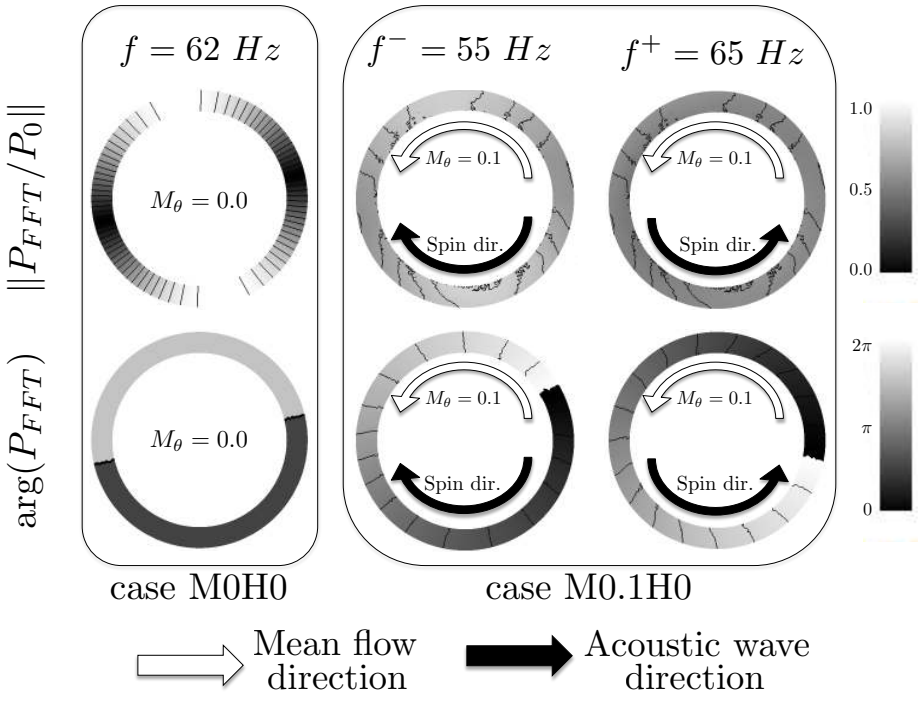

Figure 10.10: Modulus (top) and phase (bottom) of Fourier transform on pressure fields for the cases $M0H0$ (left) and $M0.1H0$ (middle and right). Mean swirl and acoustic wave directions are displayed to identify the contra-rotaing mode (middle) and the co-rotating mode (right).

10.3.3 Geometry Symmetry breaking using one Helmholtz resonator (case M0H1)

Stow & Dowling (2003) have shown that Helmholtz resonators can damp an azimuthal mode and suggest optimal locations of these damping devices. This can be tested using AMT. First, one Helmholtz resonator is introduced in the annular chamber to break symmetry (Figs. 10.2 and 10.3). Pressure signals at four probes (Fig. 10.11) located near the surrogate burners indicate that one mode is damped while the other is still present: the mode is split into two distinct components. The associated C-indicator shows that the azimuthal mode, initially standing at $t = 0\ ms$ (a- in Fig. 10.11), becomes spinning (b- in Fig. 10.11) until the limit cycle is reached at $t = 300\ ms$ (c- in Fig. 10.11), where the mode is standing again but imposing a pressure node at the Helmholtz resonator location.

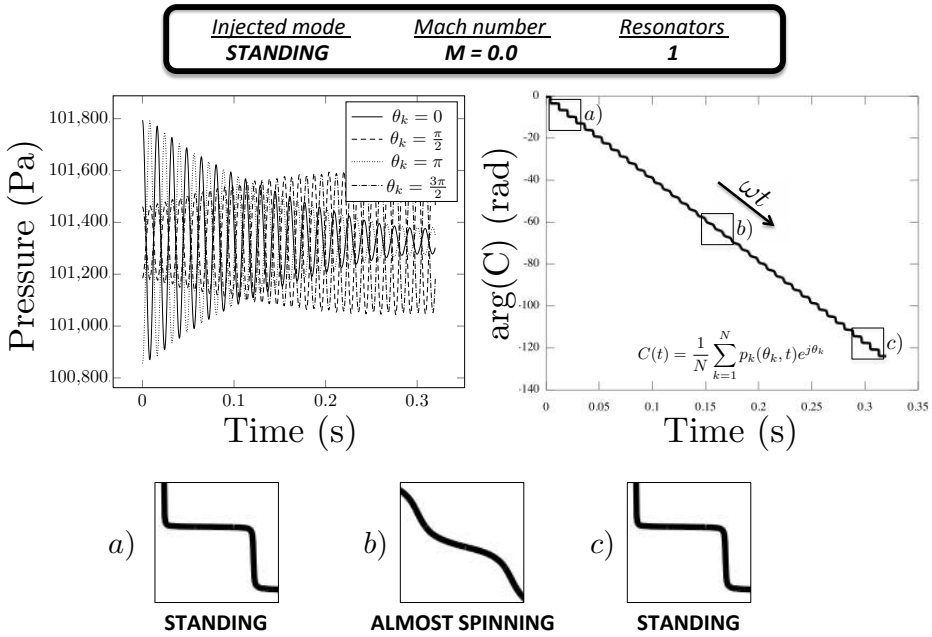

Figure 10.11: Pressure signals (left) and C-indicator (right) for the case $M0H1$: the azimuthal is split into two components with different growth rates. One is amplified while the other is damped. The nature of the mode is changing (bottom) from a) standing to b) almost spinning and finally c) standing.

To analyze these dynamic phases (standing - spinning - standing), a Sliding Fourier Transform (SFT) of the pressure field is performed. It focuses on three particular periods:

- From 0 ms to 50 ms (a- in Fig. 10.12): it corresponds to the injected standing mode.
- From 100 ms to 150 ms (b- in Fig. 10.12): a transient phase occurs where the nature changes, the azimuthal mode evolving from standing to spinning.
- From 270 ms to 320 ms (c- in Fig. 10.12): the limit cycle is reached and corresponds to a standing mode imposing a pressure node at the Helmholtz resonator location ($\times$ in Fig. 10.12).

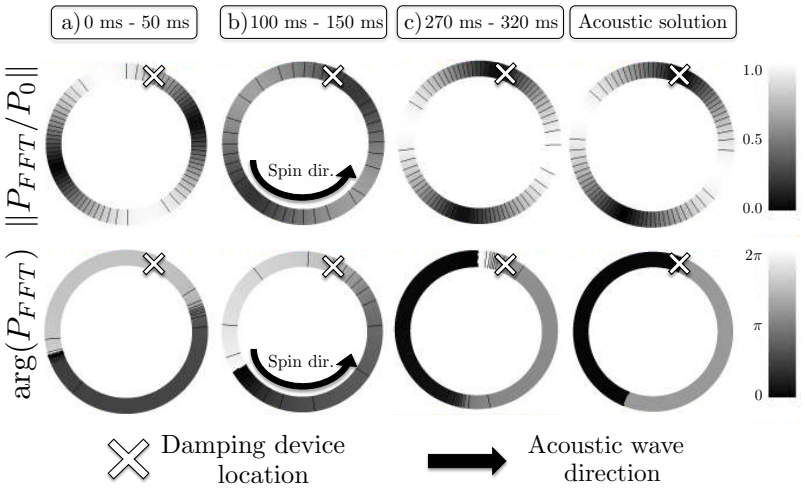

Figure 10.12: Sliding Fourier Transform (SFT) of the pressure field for the $M0H1$ case at three different time: a) initial standing mode (time from 0 ms to 50 ms), b) transient spinning mode (time from 100 ms to 150 ms) and c) final standing mode imposing a pressure node at the Helmholtz resonator location identified by $\times$ (time from 270 ms to 320 ms). In addition, the linear acoustic solution is displayed (right) showing a good agreement with the limit cycle (c).

In addition, the acoustic mode of the M0H1 case is also computed by a Helmholtz solver (Section 10.2.3). The mode (the damped component is not shown here) structure obtained (a standing mode imposing a pressure node at the Helmholtz resonator location) is in good agreement with the limit cycle observed in the LES (c- in Fig. 10.12) which demonstrates that linear analysis is able to predict structure of modes even in the limit cycle when no combustion occurs. As explained in (Bauerheim *et al.*, 2014*e*), the linear analysis provides here good estimations of mode structure because the mode nature is mainly controlled by the splitting due to the introduction of one damping device and not the non-linearities. These results show that breaking symmetry by introducing one Helmholtz resonator splits the azimuthal mode into two components which can have radically different behaviors and frequencies. This is the main specificity of azimuthal modes in non-symmetric annular combustors compared to simpler longitudinal modes with only one component or azimuthal modes in purely axisymmetric configurations where the two components are degenerate (i.e. with the same characteristics) (Bauerheim *et al.*, 2014*e*).

10.3.4 Symmetric case using two Helmholtz resonators (case M0H2)

As suggested by Stow & Dowling (2003), a second Helmholtz resonator has to be introduced to damp the two components of the azimuthal modes: the two damping devices are placed at 90° from each other (Fig. 10.3, d) to symmetrize the annular chamber and to efficiently damp the acoustic mode. Indeed, the theory developed for GS breaking in Chapter 2 proves that a splitting occurs if and only if $\gamma(\pm 2p) = 0$ where p is the azimuthal mode order (here $p = 1$) and γ is the Fourier transform of the asymmetry pat-

tern: $\gamma(k) = \sum_{i=0}^{N-1} \Gamma_i^0 e^{-j2ki\pi/N}$. For example, the previous case studied in Section 10.3.3 has introduced one Helmholtz resonator in the annular chamber with $N = 4$ sectors. If there is one resonator at the i^{th} junction between sectors, the coupling parameter is set to $\Gamma_i^0 = 1$ for the sake of simplicity here, while it is null ($\Gamma_i^0 = 0$) otherwise. Consequently, its asymmetry pattern is $s_1 = [1\ 0\ 0\ 0]$ and its Fourier transform $\gamma = \hat{s}_1 = [1\ 1\ 1\ 1]$: the splitting coefficients are $\gamma(\pm 2) = 1$ (corresponding to the third coefficient of $\hat{s}_1$ since Fourier coefficients are ranked from the 0^{th} to the $N - 1^{th}$) so that a splitting occurs, as shown in Fig. 10.11. However, introducing an other similar Helmholtz resonator at 90° modifies the asymmetry pattern (now $s_2 = [1\ 1\ 0\ 0]$) and its Fourier transform becomes $\hat{s}_2 = [2\ 1-j\ 0\ 1+j]$: the coefficients $\gamma(\pm 2)$ are now zero showing that the configuration is symmetric and that no splitting should occur. It is interesting to note that placing the second resonator at 180° instead of 90° would lead to $s_3 = [1\ 0\ 1\ 0]$ and $\hat{s}_3 = [2\ 0\ 2\ 0]$ indicating that the configuration is not symmetric ($\gamma(\pm) = 2$).

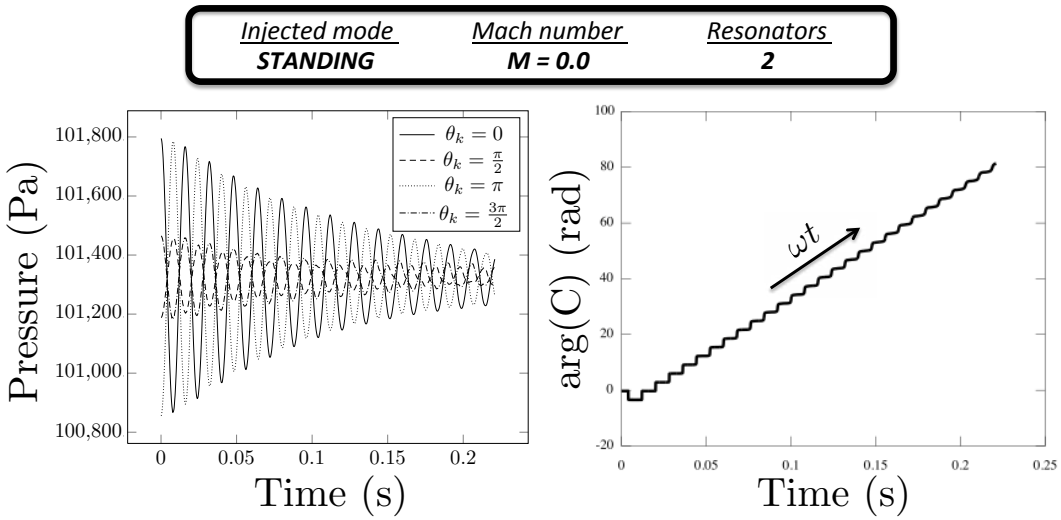

Figure 10.13: Pressure signals (left) and C-indicator (right) for the case $M0H2$: the two components of the azimuthal modes are damped with the same damping rate estimated at $\alpha = 1.0\ s^{-1}$.

Pressure signals at four probes (Fig. 10.13) located near the surrogate burners indicate that the two components are damped. The associated C-indicator shows that the azimuthal mode, initially standing at $t = 0\ ms$ becomes spinning in the clockwise direction. To numerically estimate the damping/growth rates of each component, a linear mode reconstruction is performed on the azimuthal mode. The generic form of the linear mode reconstruction is assumed to follow:

$$P_{rec} = \bar{P}_0 + \mathcal{A}e^{\alpha t}cos(2\pi ft + \phi_0) \tag{10.6}$$

where $\bar{P}_0 = 1.013\ 10^5\ Pa$ is the mean value of the pressure signal, $\mathcal{A}$ is the pressure amplitude, α is the growth or damping rate of the mode, f is the estimated frequency and ϕ_0 is a phase to match the initial pressure observed in the LES. Linear mode reconstruction using Eq. (10.6) is performed on the azimuthal mode (Fig. 10.14) using parameters described in Tab. 10.2. Both components are damped and have the same frequencies

(62.5 Hz) and growth rates ($\alpha \approx -7\ s^{-1}$): the mode is degenerate (i.e. the two components have the same characteristics) because the introduction of the second damping device has symmetrized the configuration. Note however that non-linear effects appear for low pressure amplitudes registered in the probe located at $\theta_k = \frac{\pi}{2}$ (and $\theta_k = \frac{3\pi}{2}$ not shown here) in Fig. 10.14.

Components	**Location**	$\mathcal{A}$	α	**f**	ϕ_0
Damped	$\theta_k = 0$	450 Pa	$-7\ s^{-1}$	62.5 Hz	0
Damped	$\theta_k = \frac{\pi}{2}$	125 Pa	$-7\ s^{-1}$	62.5 Hz	π

Table 10.2: Parameters used for the linear reconstruction with two Helmholtz resonators.

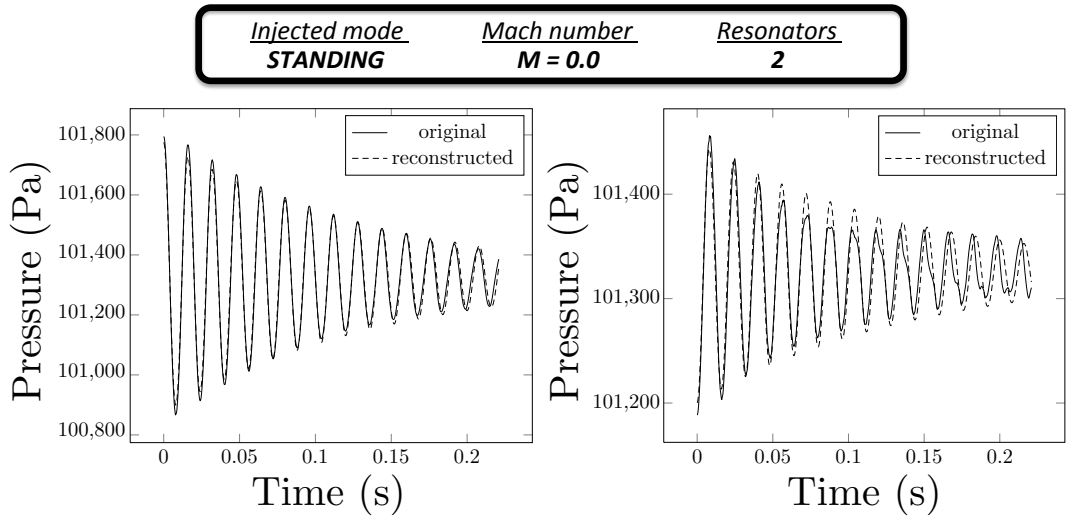

Figure 10.14: Pressure oscillations observed in the LES (——) for two probes located at $\theta_k = 0$ (left) and $\theta_k = \frac{\pi}{2}$ (right). Mode reconstruction with $\mathcal{A} \approx 450\ Pa$, $f \approx 62.5\ Hz$ and $\alpha \approx -7\ s^{-1}$ (- - - , left) and $\mathcal{A} \approx 125\ Pa$, $f \approx 62.5\ Hz$ and $\alpha \approx -7\ s^{-1}$ (····· , right).

10.4 Mode dynamics analysis: time-evolution of the azimuthal mode nature

Finally, the dynamics of azimuthal modes is unveiled for the three cases at null Mach number ($M0H0$, $M0H1$ and $M0H2$) by extracting the envelope $A^{\pm}(t)^2$ of the two components $q^{\pm} = \hat{p} \pm \rho_0 c_0 \hat{u}_\theta$ of each mode using the JAWA methodology (Section 8.4.2).

[2]The envelope extraction of the signal $q(t)$ is performed using the JAWA methodology using a filtered Hilbert transform: 1) the Hilbert transform $\mathcal{H}(q)$ is computed 2) the envelope defined by $A(t) = \sqrt{q^2 + \mathcal{H}(q)^2}$ is obtained and 3) a low-pass filtering of the envelope A(t) is performed to smooth out spurious oscillations.

Figure 10.15 shows the time evolution of the two envelopes $A^{\pm}$ for each case with iso-structure lines (i.e. constant ratio A^+/A^-, -·-·-) and iso-energy circles (i.e. constant acoustic energy[3] $E_{ac} = \frac{\hat{p}^2}{2\rho_0 c_0^2} + \frac{\rho_0}{2}\hat{u}^2$, ·····):

- **Case M0H0 :** (a) the injected mode is initially standing ($A^+ = A^-$) and remains the same because no damping, asymmetry or combustion are introduced (b).
- **Case M0H1 :** (a) the injected mode is initially standing leading to $A^+ = A^-$ but (b) because of the Helmholtz resonator, the mode rotates to impose a pressure node at the Helmholtz resonator location and cancel its effect (c): therefore the mode is finally standing ($A^+ = A^-$). Because of the damping device, acoustic energy has been dissipated leading to smaller final values of $A^{\pm}$. This result is consistent with the FFT analysis displayed in Fig. 10.12.
- **Case M0H2 :** (a) the injected mode is initially standing ($A^+ = A^-$) (b) damping devices dissipate the injected acoustic energy which leads to a decrease of the envelopes $A^{\pm}$. Compared to the previous case $M0H1$, the configuration is symmetric and only weakly affects the initial mode structure: the acoustic mode remains standing while it is dissipated by the two Helmholtz resonators. Nevertheless, the mode structure slightly drifts toward the clockwise spinning region at low amplitude as already shown by the C-indicator in Fig. 10.13

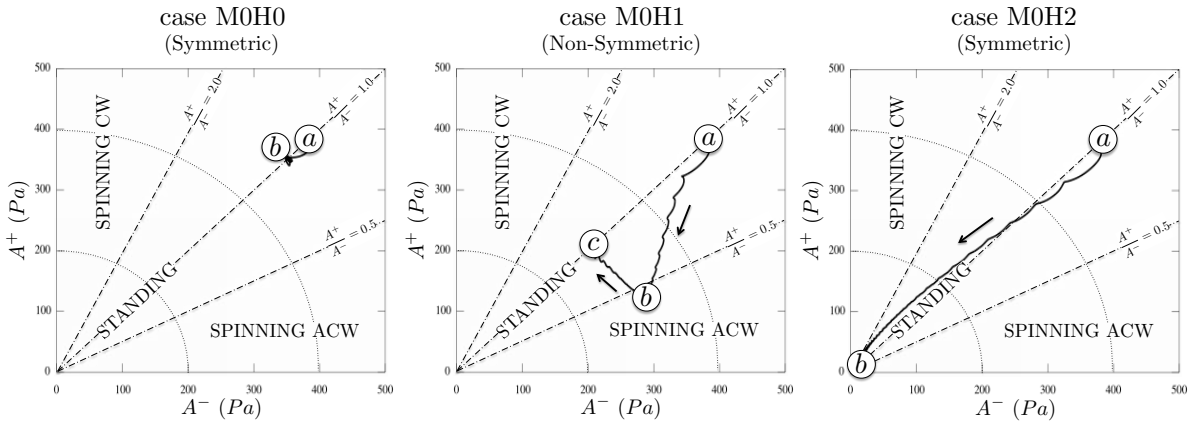

Figure 10.15: Time evolution of the two filtered envelopes of the waves $q^{\pm} = \hat{p} \pm \rho_0 c_0 \hat{u}_\theta$ in the cases at null Mach number $M0H0$ (left), $M0H1$ (middle) and $M0H2$ (right). -·-·- : Iso-structure lines $\frac{A^+}{A^-} = 0.5$, 1.0 and 2.0 ; ····· : Iso-energy circles. The initial injected modes are standing ($A^+ = A^-$).

Initializing similar cases to $M0H0$, $M0H1$ and $M0H2$ but with a clockwise (CW) spinning mode ($A^+/A^- = 4$) instead of a standing mode ($A^+/A^- = 1$) results in evolution shown in Fig. 10.16 where the time-evolution of mode dynamics for each case is:

- **Case M0H0 :** (a) the injected mode is initially spinning and remains the same (b) since no damping, asymmetry or combustion is introduced.

[3]Acoustic energy can be recast using the two waves $q^{\pm} = \hat{p} \pm \rho_0 c_0 \hat{u}$ as follow: $E_{ac} = \frac{\hat{p}^2}{2\rho_0 c_0^2} + \frac{\rho_0}{2}\hat{u}^2 = \frac{1}{4\rho_0 c_0^2}(q^{+2} + q^{-2})$. Therefore, iso-contours of acoustic energy in the diagram (q^+, q^-) or (A^+, A^-) are circles of radius $2c_0\sqrt{\rho_0 E_{ac}}$.

- **Case M0H1 :** (a) the injected mode is initially spinning ($A^+/A^- = 4$) but (c) because of the Helmholtz resonator the mode evolves and finally imposes a pressure node at the Helmholtz resonator location (after an overshoot (b)) to finish as standing ($A^+ = A^-$) . Because of the damping device, acoustic energy has been dissipated leading to smaller values of $A^{\pm}$.
- **Case M0H2 :** (a) the injected mode is initially spinning and (b) damping devices dissipate the injected acoustic energy which leads to a decrease of the envelopes $A^{\pm}$. Compared to the previous case $M0H1$, the configuration is symmetric and only weakly affects the initial mode structure: the acoustic mode remains spinning while it is dissipated by the Helmholtz resonators.

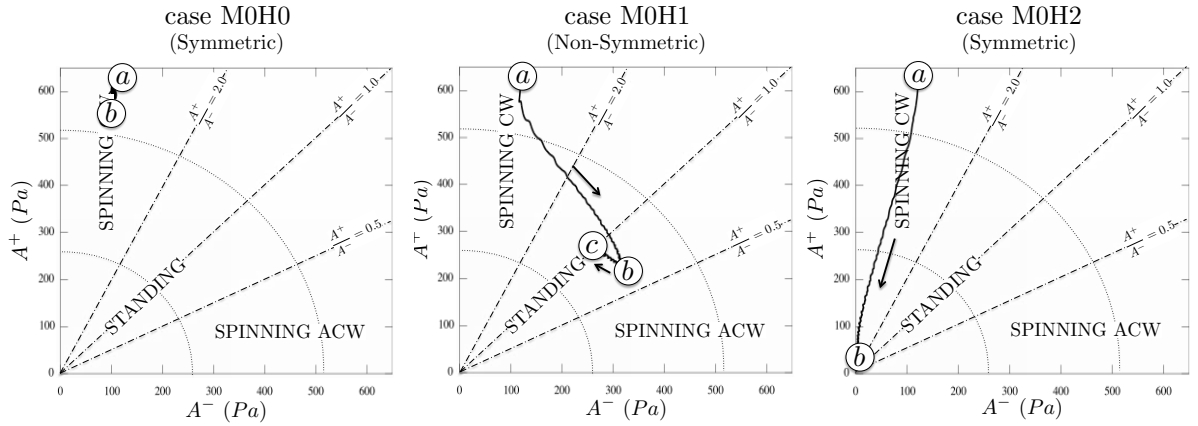

Figure 10.16: Time evolution of the two filtered envelopes of the waves $q^{\pm} = \hat{p} \pm \rho_0 c_0 \hat{u}_\theta$ in the cases at null Mach number $M0H0$ (left), $M0H1$ (middle) and $M0H2$ (right). -·-·- : Iso-structure lines $\frac{A^+}{A^-} = 0.5$, 1.0 and 2.0 ; ····· : Iso-energy circles. The initial injected modes are spinning in the clockwise direction ($A^+/A^- \sim +4$).

Figures 10.15 and 10.16 show that when the configuration is symmetric ($M0H0$ and $M0H2$), the initial ratio A^+/A^- remains constant. However, as soon as symmetry is broken ($M0H1$), the ratio A^+/A^- is not conserved and the final structure is fixed by the asymmetry of the system (here standing due to the Helmholtz resonator) as predicted by Bauerheim *et al.* (2014*e*). It proves that without combustion, the mode structure is fixed by the asymmetries of the system which can be due to an azimuthal mean flow, the introduction of one Helmholtz resonator or by mixing burners.

10.5 Conclusion

This paper presents a methodology called AMT (Acoustic Mode triggering) to study acoustic mode dynamics in annular configurations: an acoustic mode computed by a Helmholtz solver is properly introduced into the LES domain to avoid computing the transient period and study the limit cycles. In particular, this approach can provide a numerical estimation of the damping/growth rate of the injected mode. The AMT method is then applied on a simplified annular combustor with four surrogate burners

(no inlet and no combustion) to study two mechanisms controlling azimuthal modes by breaking the axi-periodicity of the annular chamber: 1) the introduction of one Helmholtz resonator and 2) the existence of a mean azimuthal flow. Results show that symmetry breaking, either by adding a Helmholtz resonator or with a swirl motion, splits the azimuthal mode into two components which can have different frequencies and growth rates. Because of this splitting, one Helmholtz resonator cannot damp completely the azimuthal mode: only one component is damped while the other remains present in the annular chamber. However, symmetrizing the configuration by adding a second Helmholtz resonator leads to a degenerate mode: the two components have the same frequencies and growth rates: both components are damped and the damping rate is numerically obtained via a linear mode reconstruction. Finally, the time-evolution of azimuthal mode dynamics is obtained by the JAWA methodology for the three cases at null Mach number showing both the asymmetry and damping devices effect on mode nature. This study proves that the dynamics of azimuthal modes can be investigated using LES combined with Helmholtz simulations. Results are in good agreement with recent linear theories which substantiates that non-linearities are not the only feature controlling the limit cycle.

Conclusion and Perspectives

The present PhD thesis deals with the fundamental aspects of symmetry breaking in azimuthal combustion instabilities and follows previous works performed at CERFACS on theory (Parmentier *et al.*, 2012) and LES (Wolf *et al.*, 2010, 2012) and at Cambridge and EM2C on the first annular experiments dedicated to azimuthal combustion instabilities (Worth & Dawson, 2013*b*,*a*; Dawson & Worth, 2014; Bourgouin *et al.*, 2013; Bourgouin, 2014). The objective was to propose and develop a novel approach and ideas on a major question encountered in the field of combustion instabilities: which key parameters control the stability and the nature of azimuthal modes ? Numerous studies have treated this problem experimentally (Krebs *et al.*, 2001; Moeck *et al.*, 2010; Worth & Dawson, 2013*b*; Bourgouin, 2014), numerically (Wolf *et al.*, 2010, 2012; Campa *et al.*, 2011) and theoretically (Parmentier *et al.*, 2012; Noiray *et al.*, 2011; Noiray & Schuermans, 2013; Ghirardo & Juniper, 2013) but usually emphasize on non-linear effects due to combustion. However, the recent experiment built at Cambridge has indicated that breaking the rotating symmetry, either by alternating different swirler types (Worth & Dawson, 2013*a*) or by introducing baffles distributed along the annular chamber (Dawson & Worth, 2014), can affect the mode nature. In addition Noiray & Schuermans (2013) also pointed out the possible effect of turbulence on the mode switching observed experimentally and on real gas turbines (Krebs *et al.*, 2001).

To investigate this new idea of symmetry breaking and unravel potential effects or even passive control techniques, the whole range of tools, from theory to full LES of the complete annular combustor, has been explored. Development of new theories (ATACAMAC, Parmentier *et al.*, 2012; Bauerheim *et al.*, 2014*d*,*a*,*e*,*c*) and tools (AMT, UQ, Bauerheim *et al.*, 2014*b*) are also required to cope with the extreme complexity of combustion instabilities in complex annular combustion chambers. Major results are summarized in the following.

Theoretical approaches

The preliminary work of Schuller *et al.* (2012) for longitudinal cases and Parmentier *et al.* (2012) for simple annular combustors was extended to more complex annular geometries to unravel coupling mechanisms between cavities. This analytical tool, called ATACAMAC provides the first fully analytical expression of the parameters controlling azimuthal modes in an annular chamber with identical or different burners, with or without mean flow.

ATACAMAC is a unique tool because it allows to study azimuthal modes directly on an analytical framework without any numerical method. For example, ATACAMAC, shows that bifurcations may occur where the annular plenum and chamber become strongly coupled which profoundly changes the stability of the whole system (Chapter 4). Validations against a full 3D acoustic tool demonstrate a good agreement between theory and acoustic simulations. Then, ATACAMAC is used to unveil key parameters on the stability of azimuthal modes. First, a generalization of the work of Parmentier *et al.* (2012) to a configuration with an arbitrary number of burners and allowing for asymmetry in the system shows that two parameters are controlling the mode in the low coupling factor limit (Chapter 2): (1) a coupling strength Σ_0 corresponding to the mean flame effect and (2) a splitting strength $\mathcal{S}_0$ associated to the symmetry breaking. Symmetry can be broken by distributing different burner types along the azimuthal direction, as done for a long time by Siemens using CBO devices on some of their burners (typically 20) and not on the others (typically 4). This type of asymmetry is called geometrical symmetry breaking (GS) and promotes standing modes. A second type of symmetry breaking, called flow symmetry (FS) breaking, is then investigated theoretically in Chapter 3 showing that a mean azimuthal Mach number can also split the azimuthal mode into two distinct components with a specific structure: this type of symmetry breaking promotes spinning modes. Finally, theory of symmetry breaking is applied on a more realistic combustion chamber containing 19 burners. The strongly coupled regime, where a full analytical solution is not known today, is investigated using a UQ methodology called Active Subspace (Chapter 5). This new method is able to reduce the size of the uncertain input space from 38 to juste a few key parameters and proves that symmetry breaking can be induced by uncertainties on the geometry or the flame models. It reveals that combustion instabilities are very sensitive to subtle changes in the chamber design. More importantly, it suggests that controlling azimuthal modes in real industrial gas turbines requires to control manufacturing margins.

This theoretical work and the ATACAMAC tool give promising results but still require future studies. More specifically:

- The strongly coupled regime is observed in many industrial applications (Campa *et al.*, 2011) but analytical studies fail to uncover this problem. More investigations, either by theory if possible or using numerical tools are needed to fully understand coupling mechanisms in axisymmetric configurations with multiple annular cavities
- Symmetry breaking in PBC configurations at high coupling factors need to be studied. Indeed, no benefit of breaking the rotating symmetry by mixing different burner types is demonstrated when coupling factors are small. However, at high coupling factors, symmetry breaking could potentially add degrees of freedom to control these modes and therefore require further investigations.
- The present ATACAMAC tool is limited to pure azimuthal modes, a limitation due to the outlet boundary condition. This limitation restrains the present work to the first azimuthal mode of industrial combustors with a chocked nozzle and fails to predict mixed modes in academic annular rig open to the atmosphere. Therefore, an extension of the quasi-one-dimensional ATACAMAC tool to a two-dimensional tool accounting for an arbitrary outlet impedance is an important path to follow.

In particular, the question of outlet impedance effects on the stability of the mode could be answered, which is still en open question today. This is one possible explanation of the difference between industrial gas turbines proned to azimuthal modes and academic configurations where azimuthal combustion instabilities are less frequent, longitudinal modes often dominating.

- For the first time UQ methodologies were applied on a thermo-acoustic problem. This path should be followed to treat more complex problems, for instance with a higher number of input parameters or by using more expensive tools such as Helmholtz solvers.
- Finally, more theories should focus on acoustic damping which is a key parameter controlling the stability of acoustic mode but only a few studies address this problem. This topic is currently investigated at CERFACS and should be continued.

Large Eddy Simulation of forced and self-excited azimuthal modes

Large Eddy Simulation is a promising tool to understand underlying phenomena leading to combustion instabilities since driving but also damping mechanisms are resolved. This PhD thesis has focused first on demonstrating the capability of such a tool to predict accurately the flame-acoustic interaction by computing Flame Transfer Functions of a single-sector of the Cambridge annular combustion chamber (Chapter 7). Results show that LES models do not affect the FTFs in this case and reveal key parameters controlling the azimuthal modes: the fuel type, the heat losses at walls and the azimuthal confinement. Combining these LES results with an Helmholtz solver computing acoustics in the full annular case demonstrates the accuracy of LES predictions, validated against experimental observations. Then, LES of the 360° configuration has been compared to experimental data provided by Cambridge (Worth & Dawson, 2013*b*,*a*; Dawson & Worth, 2014). Due to its extreme cost, only the growth phase is studied in this PhD and shows a good agreement with experimental observations. In particular, it reveals that the start-up procedure generates multiple modes in both the LES and in the experiment which complicates the understanding of key phenomena driving the instabilities and therefore methods to suppress them. Typically, the azimuthal mode grows together with a longitudinal mode, making the analysis complicated. A new post-processing methodology, called JAWA, is also developed to systematically analyze the mode nature and its dynamics even when short signals are provided. Only a few works on full LES of annular combustor have been conducted until now but this effort must be continued and complement experiments:

- A complete validation of a full annular LES against experiment is still missing due to the difficulty to represent experimental features in LES (for example here the annular plenum with sand, grids etc.). In that view, simulations and experiments in this field should be developed side-by-side and not separately.
- Even if mechanisms leading to combustion instabilities are well known in gaseous simple longitudinal premixed configurations, methodologies still lack for simulations with multiphase flows or multiple inputs - single output (MISO), sush as

complex industrial configurations with multipoint injection systems, effusive plates and complex swirlers where fuel and air are injected at different locations. Usually, these complex cases are treated by forcing one or only a few entries of the system which leads to an incomplete answer on combustion instabilities.

- A particular emphasis should be made on multiphase flows which are encountered in many industrial gas turbines. The first simulations of forced multiphase flow LES have been conducted in this PhD but not discussed in this thesis for confidentially purposes. These simulations have shown that numerous mechanisms due to liquid transport and the evaporation process lead to gaseous fuel oscillations and can impact the stability of the system. These multiphase mechanisms are less documented than pure gaseous ones and should be explored intensively using both LES and experiments. In particular, specific damping mechanisms are present in multiphase flows but are complex and not yet fully understood. An important research effort must be made in that direction.
- In general, damping mechanisms are needed for a complete framework on combustion instabilities. LES is a promising tool to build models for theories or low order models and acoustic tools. This path is currently followed at CERFACS and should be continued.

Acoustic Mode Triggering: a novel approach to study combustion instabilities

A novel methodology combining LES and Helmholtz simulations, called Acoustic Mode Triggering (AMT), is developed in this PhD thesis. It allows the study of acoustic modes in the time-domain at low cost. First, validation on simple laminar configurations have been conducted and show a very good accuracy (error is of the order of 10^{-2}) on the frequency and growth predictions at low Mach numbers (until $M = 0.1$). This tool is then applied on a longitudinal turbulent case. It offers a new method to study the cross-interaction between acoustics and turbulence. In particular, it proves that turbulence can trigger acoustic modes and that acoustic can affect back the turbulence by modifying its production and dissipation as observed on energy spectrum results. Finally, AMT is applied on simplified annular configurations to study the effects of both FS and GS breaking on azimuthal modes. Results are promising and show good agreement with the theoretical work developed in Part I of this thesis. Moreover, it allows the study of mode nature and its dynamics and reveal that: (1) Symmetry breaking affects the mode nature and (2) in axisymmetric configurations the nature is mainly impose by the initial state when no combustion occurs. This novel approach has shown interesting results and therefore needs to be applied on more complex configurations to investigate driving and damping mechanisms of combustion instabilities:

- Usually turbulence and acoustic interactions are investigated by forcing acoustic waves at the inlet or by pulsating walls. AMT provides here a third approach which deserves to be further exploited. In particular, the theoretical result of Noiray & Schuermans (2013) about turbulence affecting the azimuthal mode nature can be

investigated using AMT.

- The present work focused only on Helmholtz resonators. Other damping devices or mechanisms can be studied using AMT. In particular, baffles have been distributed along an academic chamber to analyze their impact on both stability and the nature of the unstable acoustic mode in a recent experimental work (Dawson & Worth, 2014). Moreover, mode conversion between acoustic waves into other forms like vorticity or entropy waves could be investigated using this approach. AMT appears as a potential efficient tool to build new damping models for low order and acoustic tools.
- In this PhD, AMT is applied only on configurations with no combustion. Flames should be introduced to investigate the effects and interactions between symmetry breaking and non-linear flame behavior in annular combustors and compare results to recent theories (Noiray *et al.*, 2011; Bauerheim *et al.*, 2014*e*,*a*).

Symmetry breaking in the aeroacoustic field

Symmetry breaking appears in a wide range of physical problems. A new perspective of this work is therefore the application of the theoretical background developed in Part I to other physical phenomena, especially in aeroacoustics. For instance, Fig. 10.17 (LES, left) shows the noise produced by a main landing gear (Giret *et al.*, 2013) which exhibits similar behaviors as ones observed in this thesis: coupling between the two cavities in the wheels (here in opposite phase) and GS symmetry breaking due to the vertical leg. AVSP simulations of the configuration with (Fig. 10.17, bottom right) and without (Fig. 10.17, top right) leg highlights both the coupling and the symmetry breaking effects on the mode structure and frequencies: similarly to Chapter 2, the symmetry breaking leads to a standing mode (constant phase, not shown here) and a frequency splitting $\Delta f \simeq 32\ Hz$ which may either destabilize the configuration, increase noise generation or lead to potential warble phenomena at low-frequencies. This recent observation requires further investigations, in particular using theory to complement numerical and experimental efforts.

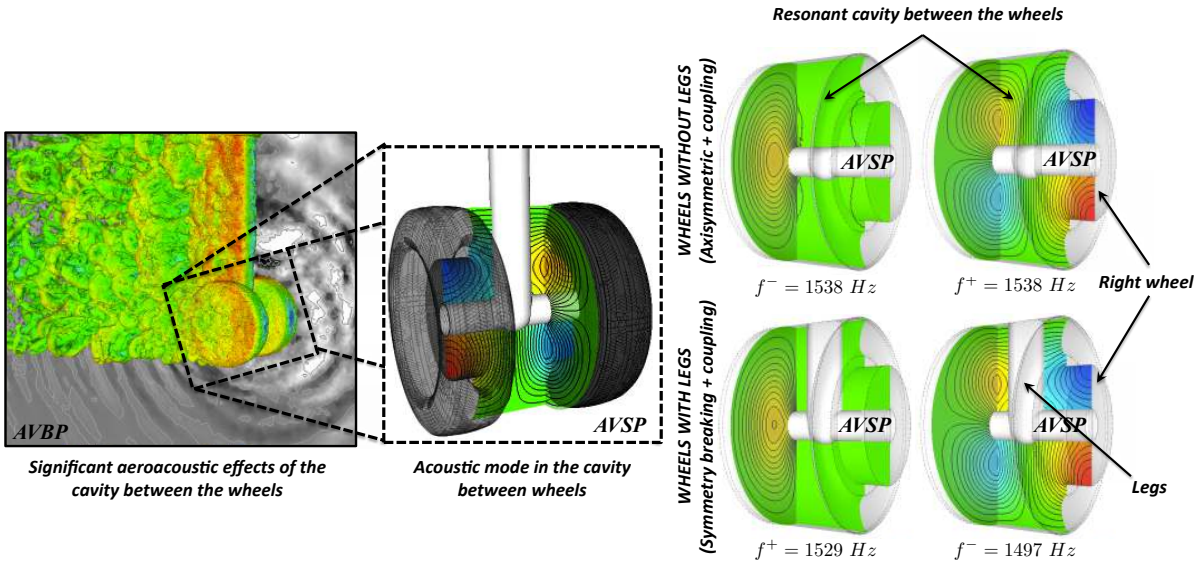

Figure 10.17: LES of an aircraft main landing gear (Lagoon project, left) and pressure fluctuations obtained by AVSP (middle) for the configuration with (right, bottom) and without (right, top) the vertical leg. Both coupling and symmetry breaking are observed and lead to a frequency splitting $\Delta f \simeq 32\ Hz$.

Publications

This work has lead to the following publications and conferences:

Ranked *A* papers

- M. Bauerheim, J-F. Parmentier, P. Salas, F. Nicoud and T. Poinsot *An analytical model for azimuthal thermo-acoustic modes in annular chamber fed by an annular plenum*, **Combustion and Flame**, 2014, 161, p. 1374-1389
- M. Bauerheim, F. Nicoud and T. Poinsot *Theoretical analysis of the mass balance equation through a flame at zero and non-zero Mach numbers*, **Combustion and Flame** (accepted, 2014, in press)
- M. Bauerheim, P. Salas, F. Nicoud and T. Poinsot *Symmetry breaking and control of azimuthal thermoacoustic modes in annular chambers*, **Journal of Fluid Mechanics** (accepted 2014, in press)
- M. Bauerheim, G. Staffelbach, N.A. Worth, J.R. Dawson, L. Gicquel and T. Poinsot *Sensitivity of LES-based flame transfer function for turbulent swirled flames and impact on the stability of azimuthal modes*, **35th International Symposium on Combustion** (accepted 2014, in press)
- M. Bauerheim, M. Cazalens and T. Poinsot *A theoretical study of mean azimuthal flow and asymmetry effects on thermoacoustic modes in annular combustors*, **35th International Symposium on Combustion** (accepted 2014, in press)

Conferences

- E. Courtine, L. Selle, F. Nicoud, W. Polifke, C. Silva, M. Bauerheim and T. Poinsot *Causality and intrinsic thermoacoustic instability modes*, **Proceedings of the Summer Program**, CTR Stanford 2014
- M. Bauerheim, A. Ndiaye, P. Constantine, G. Iaccarino, S. Moreau and F. Nicoud *Uncertainty Quantification of thermo-acoustic modes in annular combustors*, **Proceedings of the Summer Program**, CTR Stanford 2014
- M. Juniper, L. Magri, M. Bauerheim and F. Nicoud *Applications of adjoint methods in thermoacoustics*, **Proceedings of the Summer Program**, CTR Stanford 2014
- *A simple analytical model to study combustion instabilities in annular combustors*, **EuroMech colloquium 546 on acoustics** (Italy, May 2013)
- *Multiphase flow LES study of the fuel split effects on combustion instabilities in an ultra low-NOx annular combustor*, **ASME Turbo Expo 2015** (under review)
- *Uncertainty Quantification of thermoacoustic instabilities in a swirled stabilized combustor*, **ASME Turbo Expo 2015** (under review)
- *Numerical investigation of azimuthal combustion instabilities in annular combustors*, **CRCT Centrale Paris**, 2014
- *Development of ultra lean combustion systems for high OPR engines*, **3AF conference** 'Greener Aviation: Clean Sky breakthroughs and worldwide status' (Belgium, March 2014)

Appendix A

Analytical expression of the splitting strength

The general analytical expression of the splitting strength $\mathcal{S}_0$ is:

$$\mathcal{S}_0^2 = \sum_{i,k=1}^{N} \Gamma_i^0 \Gamma_k^0 \cos\left(\frac{4p\pi}{N}[k-i]\right) \tag{A.1}$$

Using $\cos(a-b) = \cos(a)\cos(b) + \sin(a)\sin(b)$ one may recast the splitting strength as:

$$\mathcal{S}_0^2 = \left[\sum_{i=1}^{N} \Gamma_i^0 \cos(4p\pi i/N)\right]^2 + \left[\sum_{i=1}^{N} \Gamma_i^0 \sin(4p\pi i/N)\right]^2$$

The above equation can be recast using the identity $a^2 + b^2 = (a+jb)(a-jb)$ where $j^2 = -1$:

$$\mathcal{S}_0^2 = \left[\sum_{i=1}^{N} \Gamma_i^0 e^{j4p\pi i/N}\right] \times \left[\sum_{i=1}^{N} \Gamma_i^0 e^{-j4p\pi i/N}\right] = \gamma(-2p) \times \gamma(2p) \tag{A.2}$$

where $\gamma(k)$ is the k^{th} Fourier coefficient of the asymmetry pattern Γ^0 defined as $\gamma(k) = \sum_{i=1}^{N} \Gamma_i^0 e^{-j2\pi ki/N}$.

Finally, the splitting strength is:

$$\mathcal{S}_0 = \sqrt{\gamma(2p) \times \gamma(-2p)} \tag{A.3}$$

The splitting strength obtained in the previous equation (A.3) gives some useful results:

- **1)** Noiray *et al.* (2011) obtained a similar result where the splitting strength is controlled only by $\gamma_{HR}(2p)$, the $2p^{th}$ Fourier coefficient of the heat-release distribution. Equation (A.3) is a generalization of such a result: the network model developed in this paper retains more geometry and flow features than the simple annular rig

considered in (Noiray *et al.*, 2011). In particular, it is shown here that the mode is controlled by the azimuthal distribution of the coupling parameter (which includes the active flame ($n-\tau$ model) but also the geometry characteristics, the upstream impedance Z of the burners as well as the difference between cold and burnt gases). It appears that all these features can effect the whole asymmetry of the system and therefore the stability and, consequently, cannot be neglected when studying combustion instabilities.

- **2)** If all coupling factors are the same (symmetric configuration), then the spectrum $\gamma(k)$ is null everywhere except for $k=0$ or $k=N$ (where $\gamma(0)=\gamma(N)=\Sigma^0=\sum_{i=1}^{N}\Gamma_i^0$ is the total coupling of the system) which leads to two types of azimuthal modes:
  a) If p is not $N/2$, N, $3N/2$ etc. then $\gamma(\pm 2p)=0$ and the splitting strength is null:

$$\mathcal{S}_0 = 0 \tag{A.4}$$

  These modes are characterized by no splitting: the two components of the azimuthal mode have the same frequencies and growth rates. They are called "degenerate doublets".
  b) However, if $p=N/2$, N, $3N/2$ etc. then $\gamma(\pm 2p)=\sum_{i=1}^{N}\Gamma_i^0=N\Gamma^0$ which gives:

$$\mathcal{S}_0 = N\Gamma^0 \tag{A.5}$$

  These modes are characterized by a strong splitting: the two components of the azimuthal mode have different frequencies and growth rates. They are called "non-degenerate singlets".
- **3)** If only two types of burner are introduced in the combustion chamber (i.e. coupling factors can only take the value Γ_1^0 or Γ_2^0 for $i\in[1,N]$), then for mode satisfying $p\neq N/2, N, ...$ the splitting strength $\mathcal{S}_0$ can be decomposed as:

$$\mathcal{S}_0 = \overbrace{2\mathcal{K}}^{\text{Imposed by the pattern}} \underbrace{\left(\Gamma_1^0-\Gamma_2^0\right)}_{\text{Imposed by the difference between burner types 1 and 2}} \tag{A.6}$$

where the reduced splitting strength $\mathcal{K}$ depends only on the asymmetry pattern and $(\Gamma_1^0-\Gamma_2^0)$ is fixed by the burner characteristics.

Proof:
The Fourier coefficient $\gamma(k)$ can be viewed as a polynomial of degree one with N indeterminates (or variables) Γ_i^0 and coefficients depending on the asymmetry pattern. When considering only two burner types (corresponding to coupling factors Γ_1^0 and Γ_2^0), $\gamma(k)$ reduces to a polynomial of only two variables. The previous point

(2) proves that for modes satisfying $p \neq N/2, N, ...$ the splitting strength and therefore $\gamma(\pm 2p)$ are null when $\Gamma_1^0 = \Gamma_2^0$. As $\Gamma_1^0 - \Gamma_2^0$ is a common root of $\gamma(\pm 2p)$ which are one-degree polynomials, they can be recast as:

$$\gamma(2p) = \alpha_{2p}(\Gamma_1^0 - \Gamma_2^0) \quad \text{and} \quad \gamma(-2p) = \alpha_{-2p}(\Gamma_1^0 - \Gamma_2^0) \tag{A.7}$$

where α_{2p} and α_{-2p} depend only on the asymmetry pattern. Consequently, using equation (A.3), the splitting strength reads:

$$\mathcal{S}_0 = \sqrt{\alpha_{2p}(\Gamma_1^0 - \Gamma_2^0) \times \alpha_{N-2p}(\Gamma_1^0 - \Gamma_2^0)} = \underbrace{\sqrt{\alpha_{2p}\alpha_{N-2p}}}_{2\mathcal{K}}(\Gamma_1^0 - \Gamma_2^0) \tag{A.8}$$

Appendix B

Summary of the analytical method providing the stability map of the p^{th} azimuthal mode

This Section summarizes the analytical method to provide the stability map of the p^{th} azimuthal mode of a chamber with N burners.

- **1)** Compute the coupling factors of each burner:

$$\Gamma_i^0 = -\frac{j}{2}\frac{S_i}{S_c}\frac{\mathbb{F}^0 C_{1-\alpha}^{k^0}[jS_\alpha^{k_u^0}Z + C_\alpha^{k_u^0}] + S_{1-\alpha}^{k^0}[jC_\alpha^{k_u^0}Z - S_\alpha^{k_u^0}]}{\mathbb{F}^0 S_{1-\alpha}^{k^0}[jC_\alpha^{k_u^0} - S_\alpha^{k_u^0}Z] + C_{1-\alpha}^{k^0}[C_\alpha^{k_u^0}Z + jS_\alpha^{k_u^0}]} \tag{B.1}$$

  where $\mathbb{F}^0 = \frac{c^0\rho^0}{c_u^0\rho_u^0}(1 + n_i e^{j\omega^0\tau_i})$, $C_x^y = cos(xyL_i)$, $S_x^y = sin(xyL_i)$, $k^0 = \omega^0/c^0$, $k_u^0 = \omega^0/c_u^0$, Z is the upstream impedance and $\omega^0 = \frac{p\pi c^0}{L_c}$.
- **2)** Compute the total "coupling strength" $\Sigma_0 = \sum_{i=1}^{N}\Gamma_i^0$.
- **3)** Compute the "splitting strength" $\mathcal{S}_0$:

$$\mathcal{S}_0 = \sqrt{\sum_{i,j=1}^{N}\Gamma_i^0\Gamma_j^0 cos\left(\frac{4p\pi}{N}(j-i)\right)} = \sqrt{\gamma(-2p)\gamma(2p)} \tag{B.2}$$

  where $\gamma(k)$ is the k^{th} Fourier coefficient of the asymmetry pattern.
- **4)** The p^{th} azimuthal mode is composed of two modes V^+ and V^- with the same order p but different wavenumber perturbations $\epsilon^\pm$ given by:

$$\epsilon^+ = -\frac{1}{2}(\Sigma_0 + \mathcal{S}_0) \quad \text{and} \quad \epsilon^- = -\frac{1}{2}(\Sigma_0 - \mathcal{S}_0) \tag{B.3}$$

- **5)** Then compute the complex frequency of the system from the definition of the wavenumber perturbation ($k^\pm L_c = \frac{2\pi f^\pm}{c^0}L_c = p\pi + \epsilon^\pm$) and equation (B.3):

$$f^\pm = \frac{pc^0}{2L_c} - \frac{c^0(\Sigma_0 \pm \mathcal{S}_0)}{4\pi L_c} \tag{B.4}$$

- **6)** Finally, the two components of the p^{th} azimuthal mode can have different frequencies ($f^+ \neq f^-$, non-degenerate singlets) if $\mathcal{S}_0 \neq 0$ or the same frequencies ($f^+ = f^-$, degenerate doublets) if $\mathcal{S}_0 = 0$. The growth rate of each mode is obtained from the imaginary part of the complex frequency obtained in equation (B.4):

$$\text{Growth rate}^{\pm} = Im(f^{\pm}) = -\frac{c^0}{4\pi L_c} Im\left(\Sigma_0 \pm \mathcal{S}_0\right) \tag{B.5}$$

Appendix C

Effect of non-linearities on symmetry breaking in annular combustors

This PhD. thesis focuses on the linear regime using $n-\tau$ or FTF models. This appendix however briefly describes a non-linear approach for ATACAMAC, similar to the one developed by Silva *et al.* (2013) to study its impact on symmetry breaking in annular gas turbines, recently observed by Ghirardo *et al.* (2015). This appendix tries to explain this non-linear behavior using the physical interpretation developed all along this PhD thesis and more specifically by relating non-linearities and the splitting strength coefficient.

For a set of FTF's (i.e. $(n_i, \tau_i)_{i=1..N}$), the ATACAMAC tool provides the corresponding frequency and growth rate of the azimuthal acoustic mode. As proposed by Silva *et al.* (2013), this linear analysis can be extended to non-linear regimes by introducing FDF's (i.e. $(n_i(\hat{u}_i), \tau_i(\hat{u}_i))_{i=1..N}$) firstly proposed by EM2C (Noiray *et al.*, 2008), which depend on the acoustic velocity level at the burner locations. Thus, the methodology follows four steps:

(1) A very small velocity perturbation $\hat{u}_i^0$ is imposed at the initial time $t = t^0$. At the initial time step, all burners have the same perturbation.
(2) The $FDF(\hat{u})$ is interpolated a the level $\hat{u}_i^0$, which provides a set $(n_i^0, \tau_i^0)_{i=1..N}$.
(3) ATACAMAC is used to predict the complex frequency ω associated to $(n_i^0, \tau_i^0)_{i=1..N}$.
(4) The frequency and growth rate are used to construct a new velocity perturbation $\hat{u}_i$ at the time $t = t^0 + \Delta t$:
(1 bis) The new velocity perturbation is used to interpolate the FDF's at the next step.

$$\hat{u}_i(t^0 + \Delta t) = \hat{u}_i(t^0) e^{-j\omega\Delta t} \tag{C.1}$$

To illustrate this methodology and non-linear behaviors of acoustic modes, a few examples are proposed here based on a PBC configuration (2 annular cavities) with $N = 4$ burners, similar to the one studied previously in this manuscript:

- **Example 1) Stable mode with standard FTF or FDF:** As shown in Fig. C.1, an arbitrary FDF and its associated FTF are chosen. The methodology proposed is performed focusing on the first azimuthal mode (the plenum mode at about 58 Hz). The velocity perturbation is rebuilt using Eq. (C.1) and is displayed in Fig. C.2. Since the mode is stable, no difference is observed between the FTF and

the FDF computations. It is worth noting that such a time-domain analysis using ATACAMAC is efficient to compute long time signals, information that cannot provide LES because of its extreme cost.

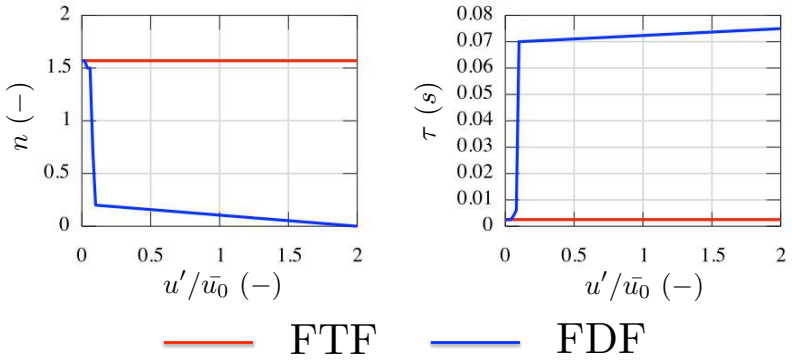

Figure C.1: FDF and its associated FTF choosen arbitrary here.

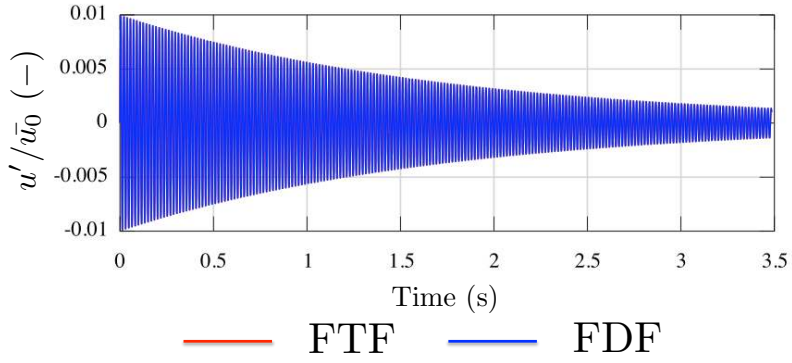

Figure C.2: Acoustic velocity perturbation of the first azimuthal mode varying in time at one burner location rebuilt using Eq. (C.1) for both FTF and FDF. Since the mode is stable, no difference between FTF and FDF is observed.

- **Example 2) Unstable mode with standard FTF or FDF:** The same FTF and FDF presented in Fig. C.1 are used but now ATACAMAC focuses on the second azimuthal mode (the chamber mode at about 90 Hz) of the configuration. Fig. C.3 shows that the mode is unstable. Compared to the FTF formulation, a limit cycle appears when using a FDF which proves, as suggested by Silva *et al.* (2013), that such an approach can incorporate non-linear behaviors into tools initially designed for the linear regime. First, for $t < 0.7s$, the amplitude and time-delay obtained by the FTF and FDF are similar and therefore both formulations leads to an unstable mode. Then, for t around $0.7s$ the FTF and FDF differ leading to different ATACAMAC predictions. In this case, the growth rate is lower when using a FDF than with a FTF, leading to a saturation effect. For $t > 0.7s$, the FTF still leads to an unstable mode while the FDF leads to a null growth rate estimation: the mode is non-linearly stable and the limit cycle appears.

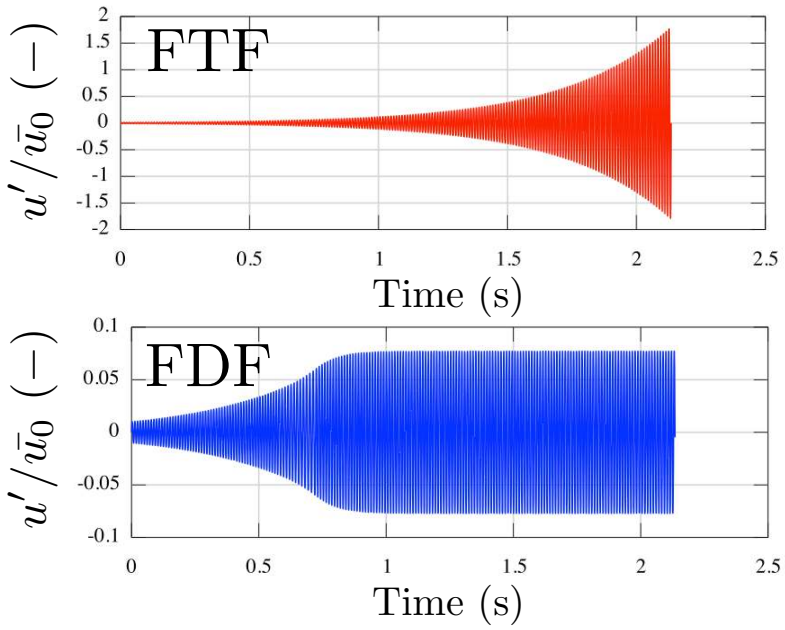

Figure C.3: Acoustic velocity perturbation of the second azimuthal mode varying in time at one burner location rebuilt using Eq. (C.1) for both FTF and FDF. The mode is found unstable and a limit cycle appears when using the FDF formulation.

- **Example 3) Mode switching and non-linear triggering:** Example 2 has shown that simple non-linear behaviors can be observed using the ATACAMAC tool (designed for the linear regime) accompanied with a FDF formulation. In this example, the same configuration is studied but with a different FDF (Fig. C.4) to highlight more complex non-linear phenomena such as mode switching and non-linear triggering. Figure C.5 displays the acoustic velocity perturbation varying in time at one burner location rebuilt using Eq. (C.1). At the initial time, the first azimuthal mode at 58 Hz is stable and the second azimuthal mode at 90 Hz is unstable. As soon as the acoustic velocity grows, the FDF is changing, leading to a case where the plenum and the chamber become strongly coupled (Bauerheim *et al.*, 2014*d*). Then, the non-linearities trigger the plenum mode which is now unstable. The acoustic perturbation growing, the plenum and chamber become again uncoupled. However, now, the chamber is stable while the plenum is unstable. Finally, the instability was triggered by the chamber mode at 90 Hz, but the limit cycle corresponds to the plenum mode at 58 Hz. Zooms on the mode switching (from chamber to plenum mode, bottom left) and on the limit cycle of the triggered plenum azimuthal mode (bottom right) are also given in Fig. C.5.

These few examples have examplified the ATACAMAC capability to retrieve some non-linear behaviors of azimuthal modes. The question asked now is "how non-linearities can affect azimuthal modes, and especially the symmetry breaking ?". Indeed, Ghirardo *et al.* (2015) have recently proven mathematically that non-linearities of the flame model can lead to a symmetry breaking. This idea is developed here using the ATACAMAC formulation, while Ghirardo *et al.* (2015) have used a full non-linear formulation, but on

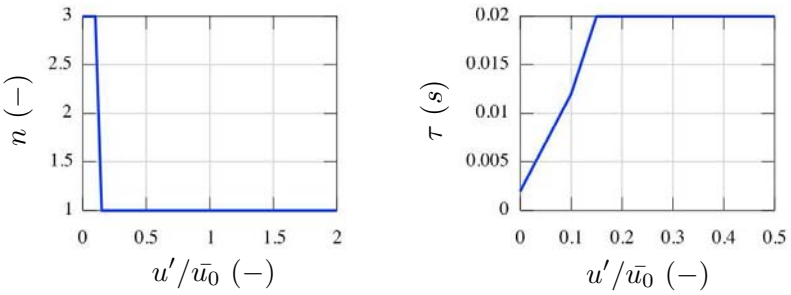

Figure C.4: FDF chosen for Example 3 to highlight mode switching and non-linear triggering.

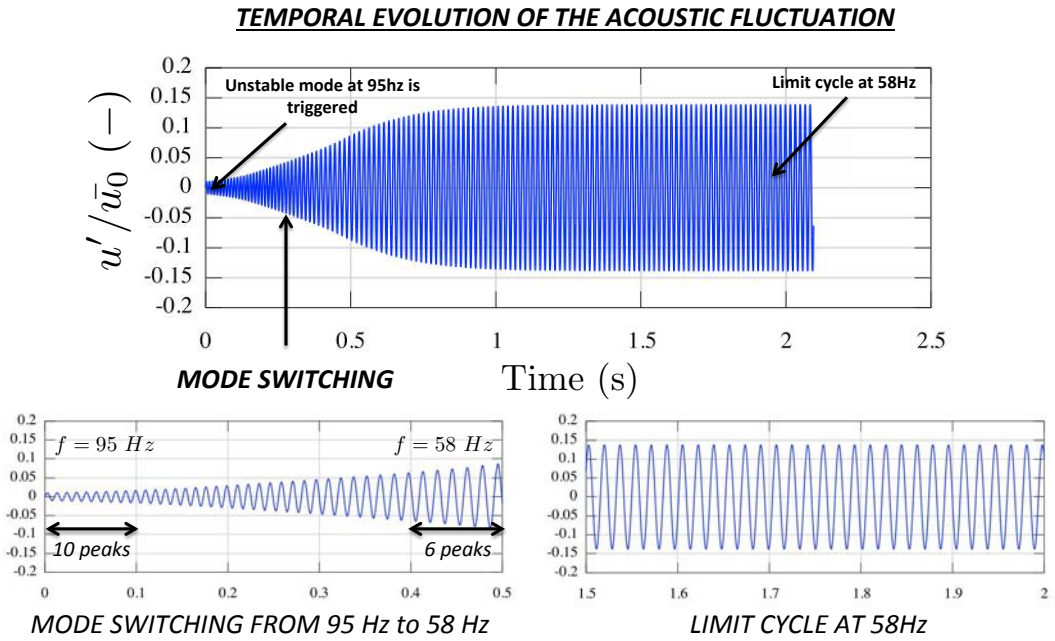

Figure C.5: Acoustic velocity perturbation of a strongly coupled mode (plenum/chamber) varying in time at one burner location rebuilt using Eq. (C.1). At the initial time the first azimuthal mode is stable while the second one is unstable. When the acoustic velocity grows, the FDF is changing leading to a mode switching (from a chamber to a plenum mode, bottom left). The final limit cycle corresponds to the plenum azimuthal mode initially stable (bottom right).

a simple annulus, as firstly proposed by Noiray *et al.* (2011) and extended by Ghirardo & Juniper (2013).

The idea proposed by Ghirardo *et al.* (2015) can be reformulated using the ATACAMAC formulation as follows: in a symmetric configuration, all flames are supposed identical, meaning that all flames have the same behavior characterized by their FTF or FDF. In other words, all flames have the same set $(n_i(\hat{u}_i,\omega),\tau_i(\hat{u}_i,\omega))$. In the FTF formulation, it implies that all flames have exactly the same (n,τ) and therefore the configuration is fully symmetric. However, in the non-linear regime, flames located at a velocity node and velocity anti-node will behave now differently: typically, flames at velocity nodes are characterized by $(n_i(\hat{u}_i,\omega),\tau_i(\hat{u}_i,\omega)) = (n_i(0,\omega),\tau_i(0,\omega)) = (n_{FTF},\tau_{FTF})$ while flames at velocity anti-nodes are described by $(n_i(\hat{u}_i,\omega),\tau_i(\hat{u}_i,\omega)) = (n_{FDF},\tau_{FDF}) \neq (n_{FTF},\tau_{FTF})$.

Consequently, as shown in Fig. C.6, the configuration is symmetric (left) but the solution is asymmetric (right). This asymmetry can be physically explained by the AT-ACAMAC formulation developed all along this PhD thesis: as displayed in Fig. C.6, the network model associated to the configuration with non-linear flames is not symmetric and the asymmetry pattern is directly linked to the azimuthal mode order p ($p = 1$ in Fig. C.6). Indeed, the FDF is usually, not a function of the velocity perturbation $\hat{u}$ itself, but rather a function of its module $\|\hat{u}\|$. For the case with $N = 4$ burners, it suggests that the two flames located at a velocity anti-node have the same $n - \tau$ parameters ($\circ$, subscript FDF) while the two other flames have different $n - \tau$ parameters ($\bullet$, subscript FTF because at a velocity node). Consequently, the asymmetry pattern is $\circ \bullet \circ \bullet$ which leads to a strong splitting strength (see Parmentier *et al.*, 2012; Bauerheim *et al.*, 2014*a*, for details about splitting effects with the asymmetry pattern $\circ \bullet \circ \bullet$): it shows that non-linearities can break the symmetry of the annular configuration. This GS breaking induces a splitting effect, which increases while the differences between $n_{FDF} - n_{FTF}$ and $\tau_{FDF} - \tau_{FTF}$ increase. More generally, an azimuthal mode of order p (i.e. $\hat{u} \sim \sin(p\theta)$) has a modulus, and therefore an asymmetry pattern due to non-linearities in the flame model, varying like $\|\hat{u}\| \sim \|\sin(p\theta)\|$ with a Fourier spectrum $\mathcal{F}[\|\hat{u}\|](k) = -\frac{2}{\pi(4k^2-1)}\delta(k - 2np)$ where $n \in \mathbb{Z}$[1]. Thus, since the splitting strength $\mathcal{S}_0$ is associated to the Fourier coefficient $\pm 2p^{th}$ of the asymmetry pattern, non-linearities can affect strongly the symmetry of the configuration leading to a non-null splitting effect increasing with the difference between the FTF (at velocity nodes) and the FDF (at velocity anti-nodes) but decreasing with the azimuthal mode order (since the Fourier coefficient varies like $\frac{1}{\pi(8p^2-1)}$).

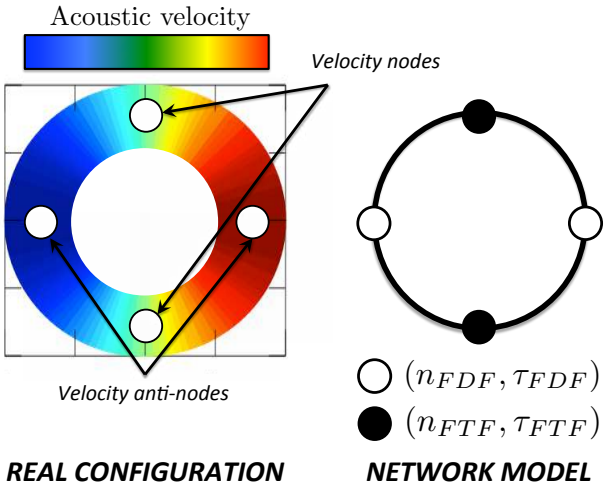

Figure C.6: First azimuthal mode in an annular cavity with $N = 4$ burners highlighting velocity nodes and anti-nodes (left) and its associated network model (right). Because of the FDF formulation, flames located at a velocity anti-nodes have different $n - \tau$ parameters than flames located at velocity nodes.

[1]One can prove that $\|sin(p\theta)\| = \frac{2}{\pi}\sum_{k\in\mathbb{Z}} \frac{sin^2(kp\theta)}{k^2-1/4} = -\frac{2}{\pi}\sum_{k\in\mathbb{Z}} \frac{1}{4k^2-1} e^{2jkp\theta}$ so that its spectrum is $-\frac{2}{\pi(4k^2-1)}\delta(k - 2np)$ where $n \in \mathbb{Z}$, thus with a strong $k = \pm 2p^{th}$ Fourier coefficient associated to the fact the $\|\hat{u}\|$ has a period two times small than $\hat{u}$

Appendix D

Analytical dispersion relation of a PBC configuration with a single burner ($N = 1$)

The analytical dispersion relation (Eq. (4.25)) is obtained for a general PBC configuration with N burners. To explain the ATACAMAC approach leading to the analytical eigenfrequencies of the system, the case of a single burner ($N = 1$) will be detailed[1].

Considering only one burner, the transfer matrix $M = R_1 T_1 - Id$ of the whole system is:

$$M = \begin{bmatrix} \cos(2k_u L_p) - 1 & -\sin(2k_u L_p) & \\ \sin(2k_u L_p) + 2\cos(2k_u L_p)\Gamma_1 & -2\sin(2k_u L_p)\Gamma_1 + \cos(2k_u L_p) - 1 & \dots \\ 0 & 0 & \\ 2\cos(k_u L_p)\Gamma_3 & -2\sin(2k_u L_p)\Gamma_3 & \end{bmatrix}$$
$$\begin{bmatrix} 0 & 0 \\ \dots \quad 2\cos(2kL_c)\Gamma_2 & -2\sin(2kL_c)\Gamma_2 \\ \cos(2kL_c) - 1 & -\sin(2kL_c) \\ \sin(2kL_c) + 2\cos(2kL_c)\Gamma_4 & -2\sin(2kL_c)\Gamma_4 + \cos(2kL_c) - 1 \end{bmatrix} \tag{D.1}$$

In the general case with N burners, a Taylor expansion of this matrix has to be performed as a first simplification. Here, the matrix is simple enough to compute analytically the determinant leading to the exact dispersion relation:

$$\begin{aligned} & (\Gamma_1\Gamma_4 - \Gamma_2\Gamma_3)\sin(2kL_c)\sin(2k_u L_p) \\ + \; & 2\Gamma_1[1 - \cos(2kL_c)]\sin(2k_u L_p) \\ + \; & 2\Gamma_4[1 - \cos(2k_u L_p)]\sin(2kL_c) \\ + \; & 4[1 - \cos(2kL_c)][1 - \cos(2k_u L_p)] = 0 \end{aligned} \tag{D.2}$$

The dispersion relation Eq. (D.2) is non-linear. The idea is to use a Taylor expansion at the second (or third) order and to solve it analytically. The expansion has to be done

[1]Since there is only one burner, the index i has been omitted to simplify notations (e.g Γ_1 instead of $\Gamma_{i=1,1}$)

around a FDCp (i.e. $kL_c = p\pi + \epsilon_c$) or FDPp (i.e. $k_u L_p = p\pi + \epsilon_p$) mode (see Section 4.3.3 for details). For instance, in the case of the WCC1 mode ($kL_c = \pi + \epsilon$ which implies $k_u L_p = \beta(\pi + \epsilon_c)$ where $\beta = \frac{c^0 L_p}{c_u^0 L_c}$), the dispersion relation Eq. (D.2) becomes:

$$[\cos(2\pi\beta) - 1][\epsilon_c \Gamma_4^0 + \epsilon_c^2 + o(\epsilon_c^2)] = 0 \tag{D.3}$$

where Γ_4^0 is the value of Γ_4 evaluated at $kL_c = p\pi$

Note that solutions of Eq. (D.3) being $\epsilon_c = -\Gamma_4^0$, it justifies that the term $\epsilon_c \Gamma_4^0$ is of the same order of magnitude than ϵ_c^2 and therefore has to be kept in the analytical dispersion relation Eq. D.2.

Analytical dispersion relations for $N > 1$ are more complex to derive but follow a similar procedure. When $N = 4$, the dispersion relation of Tab. (D.1) are obtained:

Type	Odd/Even	Second-order dispersion relation ($o(\epsilon^2)$)
WCC	Odd	$\sin(p\pi\beta)[\epsilon^2 + 4\epsilon\Gamma_4^0 + 4\Gamma_4^{0\,2}] = 0$
	Even	$\sin(p\pi\beta/2)[\epsilon^2 + 4\epsilon\Gamma_4^0] = 0$
WCP	Odd	$\sin(p\pi/\beta)[\epsilon^2 + 4\epsilon\Gamma_1^0 + 4\Gamma_1^{0\,2}] = 0$
	Even	$\sin(p\pi/(2\beta))[\epsilon^2 + 4\epsilon\Gamma_1^0] = 0$

Table D.1: Analytical expressions of wave number perturbation for WCCp and WCPp azimuthal modes

Appendix E

Stability criterion of weakly coupled modes for a four burners configuration ($N = 4$)

A mode is stable if the imaginary part of the wave number is negative. Table E.1 shows analytical expressions of the wave number perturbation ϵ for WCPp and WCCp modes[1]:

Type	Odd/Even	Wave number perturbation (ϵ)
WCC	Odd	$-2\Gamma_4^0 - H(\beta)\Gamma_2^0\Gamma_3^0$
	Even	$-2\Gamma_4^0 - G(\beta)\Gamma_2^0\Gamma_3^0$
WCP	Odd	$-2\Gamma_1^0 - H(1/\beta)\Gamma_2^0\Gamma_3^0$
	Even	$-2\Gamma_1^0 - G(1/\beta)\Gamma_2^0\Gamma_3^0$

Table E.1: Analytical expressions of wave number perturbation ϵ for WCCp and WCPp modes where $H(x) = 4\tan(p\pi x/2)$ and $G(x) = 4\frac{\sin(p\pi x/2)}{\cos(p\pi x/2)-(-1)^{p/2}}$ have real values.

Analytical stability criteria can be derived by calculating the sign of $Im(\Gamma_1^0)$, $Im(\Gamma_4^0)$ and $Im(\Gamma_2^0\Gamma_3^0)$ using the following definitions: $\mathbb{F}^*$ is the complex conjugate of the flame parameter $\mathbb{F} = \frac{\rho^0 c^0}{\rho_u^0 c_u^0}\left(1 + n.e^{j\omega^0\tau}\right)$, $\theta^0 = \omega^0(1-\alpha)L_i/c^0 \in \mathbb{R}$ and $\theta_u^0 = \omega^0\alpha L_i/c_u^0 \in \mathbb{R}$. The notation $\mathfrak{D}$ refers to $\mathfrak{D} = |\cos(\theta^0)\sin(\theta_u^0) + \mathbb{F}\sin(\theta^0)\cos(\theta_u^0)|^2$

With these notations, the sign of the imaginary part of these coupling parameters are:

$$Im(\Gamma_1^0) = \frac{S_i}{4S_p\mathfrak{D}}\sin(2\theta^0)Im(\mathbb{F}) \tag{E.1}$$

$$Im(\Gamma_4^0) = -\frac{S_i}{4S_c\mathfrak{D}}\sin(2\theta_u^0)Im(\mathbb{F}) \tag{E.2}$$

[1]Since all sectors are identical, the index i has been omitted to simplify notations (e.g Γ_1 instead of $\Gamma_{i,1}$)

Eqs. (E.1 - E.2) lead to simple analytical stability criteria for WCCp and WCPp modes:

$$\sin(2\pi\tau/\tau_c^0)\sin\left(2p\pi\frac{\alpha L_i c^0}{L_c c_u^0}\right) < 0 \quad \text{for WCCp modes} \tag{E.3}$$

$$\sin(2\pi\tau/\tau_p^0)\sin\left(2p\pi\frac{(1-\alpha) L_i c_u^0}{L_p c^0}\right) > 0 \quad \text{for WCPp modes} \tag{E.4}$$

Appendix F

Flame position effect on annular combustors stability

Similarly to longitudinal modes in the Rijke tube (Schuller *et al.*, 2012; Poinsot & Veynante, 2011; Kaess *et al.*, 2008), the flame position (defined by α) also controls the stability (Eq. (4.48)). In a quasi-isothermal Rijke tube, for common (small) values of the FTF time-delay τ, stability of the first longitudinal mode is obtained only when the flame is located in the upper half of the tubes (Heckl & Howe, 2007; Zhao, 2012), i.e. $\alpha > 1/2$, which can be extended for the p-th longitudinal mode:

$$\frac{2m+1}{2p} < \alpha < \frac{2(m+1)}{2p}, \ \forall m \in \mathbb{N} \quad \text{(Rijke tube)} \tag{F.1}$$

Eq. (4.48) highlights a similar behavior for azimuthal modes in a PBC configuration: for a WCCp mode with small values of the time-delay $\tau < \tau_c^0/2$, $\sin(2\pi\frac{\tau}{\tau_c^0})$ is positive and Eq. (4.48) leads to:

$$\frac{2m+1}{2p}\frac{L_c c_u^0}{L_i c^0} < \alpha < \frac{2(m+1)}{2p}\frac{L_c c_u^0}{L_i c^0}, \ \forall m \in \mathbb{N} \quad \text{(WCCp modes)} \tag{F.2}$$

Usually, the critical flame position $\alpha_{crit} = \frac{L_c c_u^0}{2pL_i c^0}$ is larger than unity because the half-perimeter of the annular cavity is much longer than the burner length ($L_c \gg L_i$). Since the range of the normalized flame position α is $[0-1]$, the flame position may affect the stability only for high-order modes (i.e. p large enough to get $\alpha_{crit} < 1$). For instance, in the case described in Table 4.1 with the corrected burner length $L_i \simeq 0.76\ m$, the critical flame positions α_{crit} and the stability ranges (Eq. (F.2)) are shown in Tab. F.1.

The change of stability with the flame position α for small time-delays predicted in Tab. F.1 has been validated using the numerical resolution of the dispersion relation (Eq. (4.25)) in Fig. F.1. The critical flame positions obtained in Tab. F.1 are well captured for all modes. A situation where the plenum/chamber interaction is not negligible is shown for the WCC1 mode with $\alpha = 0.3$ (i.e. the flame is close the pressure node imposed by the large annular plenum).

Mode order (p)	$p=1$	$p=3$	$p=5$	$p=7$
$\alpha_{crit} = \frac{L_c c_u^0}{2pL_i c^0}$	2.70	0.9	0.54	0.39
α satisfying Eq. (F.2)	none	[0.9 - 1]	$[0.54 - 1]$	$[0.39 - 0.78]$

Table F.1: Critical flame positions α_{crit} and flame positions satisfying Eq. (F.2) for WCCp odd-order modes of the case described in Table 4.1

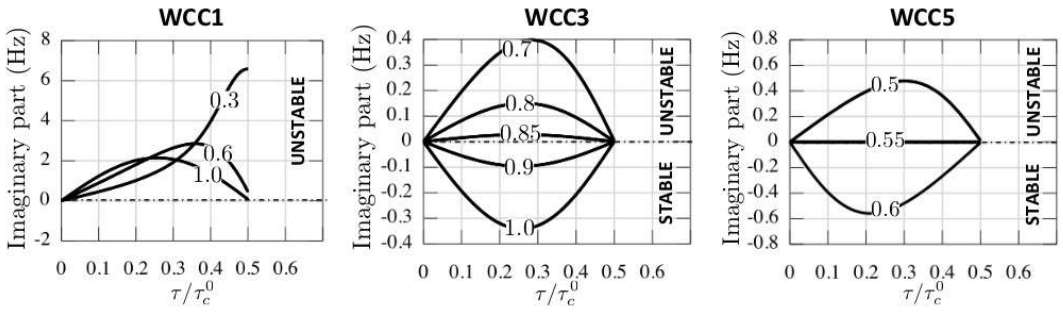

Figure F.1: Growth rate for several flame positions α of the WCC1 ($\alpha = 0.3,\ 0.6,\ 1.0$ - left), WCC3 ($\alpha = 0.5,\ 0.8,\ 0.85,\ 0.9,\ 1.0$ - middle) and WCC5 ($\alpha = 0.5,\ 0.55,\ 0.6$ - right) modes for small time delays ($\tau/\tau_c^0 < 1/2$) using the numerical resolution of the dispersion relation (Eq. (4.25)) with $n_i = 1.57$

Appendix G

Kernel Density Estimation (KDE)

Compared to experiment, Large Eddy Simulations (LES) usually provides high resolved but time-limited data or signals. This limitation complicates post-processing such as FFT or probability estimations, as the JAWA methodology proposed in Chapter 8. Indeed, a classic technique is, from a dataset α, to divide the range $[\min(\alpha) - \delta, \max(\alpha) + \delta]$ by N and create a histogram, where δ is defined by the user and corresponds to the anchor point of the histogram. However, as presented in Fig. G.1, such a simplistic method is highly sensitive to the used procedure (anchor point, number of point per bins etc.). Figure G.1 shows 50 random points whose PDF is estimated using histogram with two different anchor point (i.e. two different values for δ) leading to completely different estimated PDF. This drawback usually appears when the number of samples is limited. This problem can be tackled only by very low resolutions of the estimated PDF.

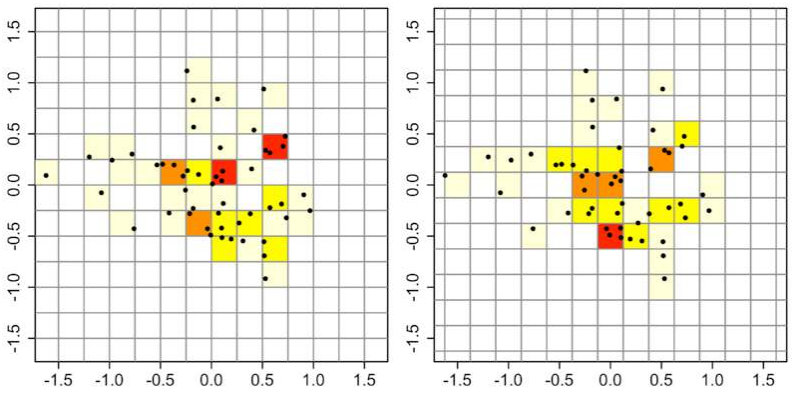

Figure G.1: Example (from internet) of the PDF estimation of 50 random values using histogram with two different anchor points: results (red for high PDF, white for null PDF) are completely different showing that such simplistic approaches are very sensitivity to the used procedure.

A solution is to use a technique known as Kernel Density Estimation (KDE) which provides accurate PDF estimations where the resolution is independent of the number of samples. Let's consider the dataset α with a true PDF called f_α. The estimation of this PDF is called f_h and is obtained by combining multiple local probability shapes, called

kernels, as shown in Fig. G.2 (left):

$$f_h(\alpha) = \frac{1}{n}\sum_{i=1}^{n} K_h(\alpha - \alpha_i) \quad \text{where} \quad K_h(\alpha - \alpha_i) = \frac{1}{h}K\left(\frac{\alpha - \alpha_i}{h}\right) \tag{G.1}$$

where K_h is called the smoothed kernel and h is the smoothing factor.

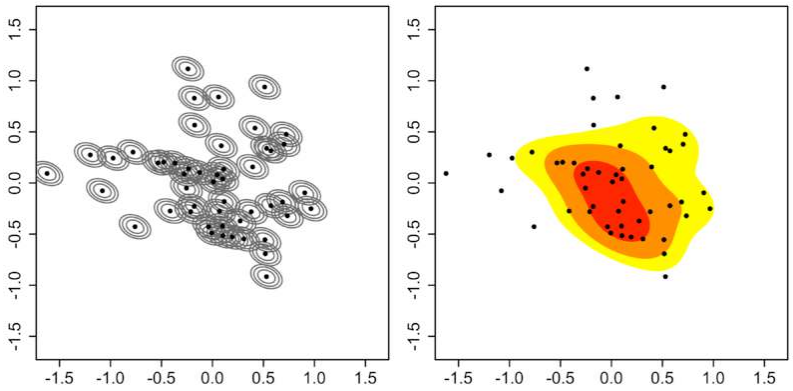

Figure G.2: Example (from internet) of the PDF estimation of 50 random values using KDE (right). Local probability functions, here smoothed gaussian functions, are centered at each sample location (left).

Usually, the kernel is chosen as a gaussian (normal) distribution since it provides simple theoretical results. The kernel is smoothed by a factor h which has to be chosen by the user. Nevertheless, this parameter can be evaluated analytically from an optimization of the error between f_α and f_h, leading to an optimal value:

$$h_{opt} = \left(\frac{\mathcal{R}(K)}{n\mathcal{M}(K)^2\mathcal{R}(f''_\alpha)}\right)^{1/5} \tag{G.2}$$

where $\mathcal{R}(g) = \int g(x)^2 dx$ and $\mathcal{M}(g) = \int x^2 g(x)$.

Obviously, the optimal smoothing factor cannot be rigorously obtained since the true PDF f_α is not known. An iterative procedure can be constructed by assuming that $f''_\alpha \simeq f''_h$. In this PhD thesis, a full analytical formula is used to approximate this parameter:

$$h_{opt} = \left(\frac{4 \times med(\|\alpha - med(\alpha)\|)}{3 \times 0.6745 \times n}\right)^{1/5} \tag{G.3}$$

An example is given in Fig. G.3 showing the PDF estimation of the centered wave ratio $\alpha = \frac{A^+ - A^-}{A^+ + A^-}$, extracted from a short LES (Chapter 8), using histogram (top left) and KDE with several smoothing factor h, from $0.25h_{opt}$ to $4h_{opt}$ where h_{opt} is obtained from Eq. (G.3). It shows that the histogram is under resolved, while KDE with $h < h_{opt}$ are noisy and $h > h_{opt}$ are over smoothed. KDE with h_{opt} provides the best PDF estimation possible. Note that the smoothing parameter h_{opt} is defined using only the sample data α and not the grid resolution on which the PDF will be estimated (corresponding to the

number of bins for a classic histogram). Therefore, increasing the resolution of the PDF does not change the procedure and the PDF results since h_{opt} is unchanged (only data can modify its value, which is what an accurate well-posed procedure intends to do). Note that this KDE procedure can be improved by choosing a local, instead of a global as presented here, smoothing factor but this topic is still an open question today.

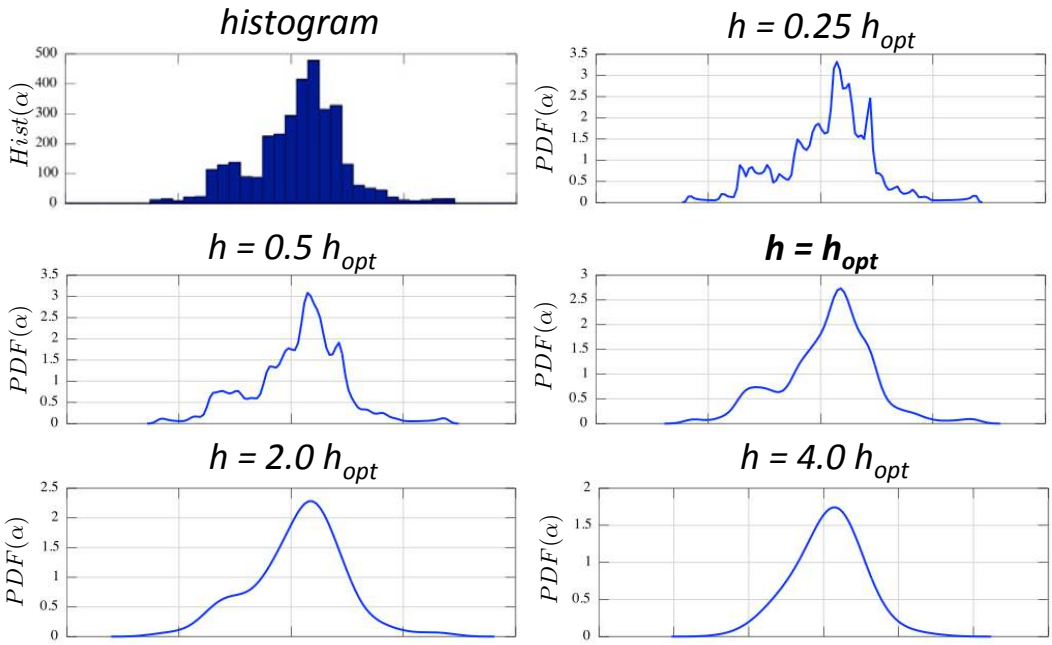

Figure G.3: Example of the PDF estimation of the centered wave ratio $\alpha = \frac{A^+ - A^-}{A^+ + A^-}$, extracted from a short LES (Chapter 8), using histogram (top left) and KDE with several smoothing factors h, from $0.25h_{opt}$ to $4h_{opt}$, where h_{opt} is obtained from Eq. (G.3)

Appendix H

Acoustic flux and growth rate of a longitudinal acoustic mode with a non-null mean flow

The case with a mean axial flow described in Fig. 9.4 is investigated here with different boundary conditions:

- **Case UP:** the inlet boundary condition is set to $\hat{u}(x=0)=0$ while the outlet is $\hat{p}(x=L)=0$.
- **Case MP:** the inlet boundary condition is now set to $\hat{m}(x=0)=\rho_0\hat{u}(x=0)+\frac{M}{c_0}\hat{p}(x=0)=0$ while the pressure outlet is still enforced: $\hat{p}(x=L)=0$.
- **Case UJ:** the inlet boundary condition is set to $\hat{u}(x=0)=0$ but now the outlet condition is an imposed enthalpy: $\rho_0\hat{J}(x=L)=\hat{p}(x=L)+\rho_0 c_0 M\hat{u}(x=L)=0$.

For these three cases, the pressure and velocity expressions are:

$$\hat{p}(x)=Ae^{jk^+x}+Be^{-jk^-x} \tag{H.1}$$

$$\rho_0 c_0\hat{u}(x)=Ae^{jk^+x}-Be^{-jk^-x} \tag{H.2}$$

where A and B are constants, x is the axial coordinate, $j^2=-1$ and $k^{\pm}=\frac{\omega}{c_0(1\pm M)}$.

Using the pressure and velocity expressions and applying boundary conditions for each case, a dispersion relation is obtained. The argument of the dispersion relation gives the frequency while its modulus gives the growth rate. Results are summarized in Tab. H.1:

Case	Frequency $Re(f)$	Growth rate $Im(f)$	$Im(f)$ (low Mach)
UP	$\frac{(2p+1)c_0}{4L}(1-M^2)$	0	0
MP		$-\frac{c_0(1-M^2)}{4\pi L}\ln\left(\frac{1+M}{1-M}\right)$	$\sim-\frac{c_0 M}{2\pi L}$
UJ		$+\frac{c_0(1-M^2)}{4\pi L}\ln\left(\frac{1+M}{1-M}\right)$	$\sim+\frac{c_0 M}{2\pi L}$

Table H.1: Analytical frequency and growth rate for the three cases UP, MP and UJ.

Table H.1 shows that non-zero Mach numbers can lead either to neutral, damped or amplified mode. Moreover the real frequency is only weakly affected by the mean

flow ($\propto M^2$) while the growth rate is significantly changed ($\propto M$). At non-null Mach numbers, the acoustic flux $\hat{F}$ is (Myers, 1986):

$$\hat{F}(x) = (\hat{u} + \frac{u_0}{\rho_0 c_0^2}\hat{p})(\hat{p} + \rho_0 u_0 \hat{u}) = \hat{m}\hat{J} \tag{H.3}$$

Consequently, acoustic fluxes at the inlet and outlet boundaries as well as the total acoustic flux $\hat{F}_{tot} = \hat{F}(x=0) - \hat{F}(x=L)$ for the three cases read:

Case	$\hat{F}(x=0)$	$\hat{F}(x=L)$	$\hat{F}_{tot}$
UP	$\frac{M}{\rho_0 c_0}\hat{p}^2(x=0) = \frac{4MA^2}{\rho c_0}$	$\rho_0 c_0 M \hat{u}^2(x=L) = \frac{4MA^2}{\rho c_0}$	0
MP	0	$\rho_0 c_0 M \hat{u}^2(x=L) > 0$	$-\rho_0 c_0 M \hat{u}^2(x=L) < 0$
UJ	$\frac{M}{\rho_0 c_0}\hat{p}^2(x=0) > 0$	0	$\frac{M}{\rho_0 c_0}\hat{p}^2(x=0) > 0$

Table H.2: Analytical frequency and growth rate for the three cases UP, MP and UJ.

Table H.2 is consistent with growth rates obtained in Tab. H.1 since the acoustic energy conservation for an isentropic flow reads (Myers, 1986):

$$\frac{\partial \hat{E}}{\partial t} = \hat{F}_{tot} \tag{H.4}$$

where the acoustic energy is $\hat{E} = \frac{\hat{p}^2}{2\rho_0 c_0^2} + \frac{1}{2}\rho_0 \hat{u}^2 + \frac{u_0}{c_0^2}\hat{p}\hat{u}$. Note that in the case UJ, the inlet boundary condition acts like an active device (positive acoustic flux $\hat{F}(x=0) = \frac{M}{\rho_0 c_0}\hat{p}^2(x=0) > 0$, Tab. H.2) and therefore a fixed velocity inlet is not a physical boundary condition.

Appendix I

C-indicator with N equi-distributed pressure probes

In this paper, the C-indicator $C(t) = \frac{1}{N}\sum_{k=1}^{N} p_k(\theta_k, t)e^{j\theta_k}$ proposed by Schuermans et al. and already used in (Wolf *et al.*, 2012; Worth & Dawson, 2013*b*) is applied to highlight the nature of the azimuthal modes observed in LES. This section intends to derive the analytical expression of the C-indicator according to the mode nature: standing or spinning.

- **Standing mode:** Assuming a standing mode at the frequency f, the pressure at the probe k reads:

$$P_k(t) = P_0 \cos(2\pi f t)\cos(\theta_k) \tag{I.1}$$

Using $\cos(\theta_k) = \frac{1}{2}\left(e^{j\theta_k} + e^{-j\theta_k}\right)$, the C-indicator reduces to:

$$C(t) = \frac{P_0}{2N}\cos(2\pi f t)\sum_{k=1}^{N}\left(e^{2j\theta_k}+1\right) = \frac{P_0}{2}\cos(2\pi f t) + \frac{P_0}{2N}\cos(2\pi f t)\sum_{k=1}^{N} e^{2j\theta_k} \tag{I.2}$$

If $N \neq 1$ or 2 (i.e. more than two probes are used), the term $\sum_{k=1}^{N} e^{2j\theta_k}$ is null leading to the C-indicator:

$$C(t) = \frac{1}{2}P_0\cos(2\pi f t) \quad \text{with the phase} \quad \arg(C(t)) = 0 \text{ or } \pi \tag{I.3}$$

- **Spinning mode:** Assuming a spinning mode at the frequency f, the pressure at the probe k reads:

$$P_k(t) = P_0\cos(2\pi f t \pm \theta_k) \tag{I.4}$$

where wave $(-)$ rotates in the clockwise direction and the wave $(+)$ in the anti-clockwise direction.
Using $\cos(2\pi f t \pm \theta_k) = \frac{1}{2}\left(e^{j2\pi f t \pm j\theta_k} + e^{-j2\pi f t \mp j\theta_k}\right)$, the C-indicator reduces to:

$$C(t) = \frac{P_0}{2}e^{\mp j2\pi f t} + \frac{P_0}{2N}e^{\pm j2\pi f t}\sum_{k=1}^{N} e^{\mp 2j\theta_k} \tag{I.5}$$

If $N \neq 1$ or 2 (i.e. more than two probes are used), the term $\sum_{k=1}^{N} e^{\mp 2j\theta_k}$ is null leading to the C-indicator:

$$C(t) = \frac{P_0}{2} e^{\mp j2\pi ft} \quad \text{with the phase} \quad \arg(C(t)) = \mp 2\pi ft = \mp \omega t \tag{I.6}$$

where ω is the angular frequency and $+$ (resp. $-$) characterizes the clockwise (resp. anti-clockwise) spinning wave.

Consequently, the phase of the C-indicator provides the nature of the azimuthal modes considering two assumptions: 1) Pressure probes are equip-distributed and 2) more than two probes are used to identified the mode. Table I.1 summarizes these results:

Nature	$\mathbf{2C(t)/P_0}$	$\arg(\mathbf{C(t)})$
Standing	$\cos(2\pi ft)$	0 or π
Spinning (clockwise)	$e^{+j2\pi ft}$	$+\omega t$
Spinning (anti-clockwise)	$e^{-j2\pi ft}$	$-\omega t$

Table I.1: analytical expressionsof the C-indicator and its phase according to the mode nature.

Bibliography

Acharya, V. & Lieuwen, T. 2013 Dynamics of axisymmetric premixed, swirling flames subjected to helical disturbances. *AIAA 51th Aerosp. Sci. Meet., AIAA Pap. 2013-1179* . (Cited on page 25.)

Agarwal, N.K. & Bull, M.K. 1989 Acoustic wave propagation in a pipe with fully developed turbulent flow. *J. Sound Vib.* **132** (2), 275–298. (Cited on page 211.)

Angelberger, C., Veynante, D., Egolfopoulos, F. & Poinsot, T. 1998 Large eddy simulations of combustion instabilities in premixed flames. *Proc. of the Summer Program* pp. 61–82. (Cited on pages 161 and 162.)

Auzillon, P., Gicquel, O., Darabiha, N., Veynante, D. & Fiorina, B. 2012 A filtered tabulated chemistry model for les of stratified flames. *Combust. Flame* **159** (8), 2704–2717. (Cited on page 163.)

Barman, A., Barman, S., Kimura, T., Fukuma, Y. & Otani, Y. 2010 Gyration mode splitting in magnetostatically coupled magnetic vortices in an array. *J. Phys. D: Appl. Phys.* **43**, 422001. (Cited on pages 15 and 16.)

Bauerheim, M., Cazalens, M. & Poinsot, T. 2014*a* A theoretical study of mean azimuthal flow and asymmetry effects on thermo-acoustic modes in annular combustors. *Proc. Combust. Inst. (accepted, in press)* **35**. (Cited on pages 17, 26, 27, 56, 120, 135, 218, 235, 239, and 253.)

Bauerheim, M., Ndiaye, A., Constantine, P., Iaccarino, G., Moreau, S. & Nicoud, F. 2014*b* Uncertainty quantification of thermo-acoustic instabilities in annular combustors. *Proc. of the Summer Program (in press)* . (Cited on pages 26 and 235.)

Bauerheim, M., Nicoud, F. & Poinsot, T. 2014*c* Theoretical analysis of the mass balance equation through a flame at zero and non-zero mach numbers. *Combust. Flame (in press)* . (Cited on pages 29 and 235.)

Bauerheim, M., Parmentier, J.F., Salas, P., Nicoud, F. & Poinsot, T. 2014*d* An analytical model for azimuthal thermoacoustic modes in an annular chamber fed by an annular plenum. *Combustion and Flame* **161**, 1374–1389. (Cited on pages 15, 26, 27, 32, 44, 46, 47, 51, 55, 69, 74, 76, 77, 78, 84, 118, 121, 235, and 251.)

Bauerheim, M., Salas, P., Nicoud, F. & Poinsot, T. 2014*e* Symmetry breaking of azimuthal thermoacoustic modes in annular cavities: a theoretical study. *J. Fluid Mech. (in press)* . (Cited on pages 17, 26, 27, 206, 218, 219, 223, 225, 228, 232, 235, and 239.)

Berenbrink, P. & Hoffmann, S. 2001 Suppression of dynamic combustion instabilities by passive and active means. *ASME Paper 2001-GT-42* . (Cited on pages 32, 43, 54, 62, and 63.)

Blimbaum, J., Zanchetta, M., Akin, T., Acharya, V., J.O'Connor, Noble, D.R. & Lieuwen, T. 2012 Transverse to longitudinal acoustic coupling processes in annular combustion chambers. *International journal of spray and combustion dynamics* **4** (4), 275–298. (Cited on pages 46 and 75.)

Blumenthal, R.S., Subramanian, P., Sujith, R. & Polifke, W. 2013 Novel perspectives on the dynamics of premixed flames. *Combust. Flame* **160** (7), 1215–1224. (Cited on page 25.)

Borisnika, S.V. 2006 Symmetry, degeneracy and optical confinement of modes in coupled microdisk resonators and photonic crystal cavities. *IEEE J. Sel. Topics Quantum Electron* **12** (6), 1175–1182. (Cited on page 15.)

Bourgouin, J-F. 2014 Dynamique de flamme dans les foyeres annulaires comportant des injecteurs multiples. PhD thesis, Ecole Centrale de Paris (EM2C). (Cited on pages 23, 195, 196, and 235.)

Bourgouin, J-F., Durox, D., Moeck, J.P., Schuller, T. & Candel, S. 2013 Self-sustained instabilities in an annular combustor coupled by azimuthal and longitudinal acoustic modes. *ASME Paper 2013-GT-95010* . (Cited on pages 23, 32, 35, 72, 84, 89, 120, 168, 174, 218, and 235.)

Bourgouin, J-F., Durox, D., Moeck, J.P., Schuller, T. & Candel, S. 2014 Characterization and modeling of a spinning thermoacoustic instability in an annular combustor equipped with multiple matrix injectors. *ASME Paper 2014-GT-25067* . (Cited on page 114.)

Boussinesq, J. 1877*a* Essai sur la théorie des eaux courantes. *26ème édn. Acad. Sci. Paris* . (Cited on page 155.)

Boussinesq, J. 1877*b* Théorie de l'écoulement tourbillant. *Mém. Présentés par Divers Savants. Acad. Sci. Inst. Fr.* **23**, 46–50. (Cited on page 156.)

Branley, N. & Jones, W. P. 2001 Large eddy simulation of a turbulent non-premixed flame. *Combust. Flame* **127**, 1914–1934. (Cited on page 28.)

Bray, K. N. C. & Moss, J. B. 1977 A closure model for the turbulent premixed flame with sequential chemistry. *Combust. Flame* **30**, 125–131. (Cited on page 159.)

Brear, M.J., Nicoud, F., Talei, M., Giauque, A. & Hawkes, E.R. 2012 Disturbance energy transport and sound production in gaseous combustion. *J. Fluid Mech.* **707**, 53–73. (Cited on page 24.)

Brown, R. S., Blackner, A., M. Willoughby, P. G. & Dunlap, R. 1986 Coupling between acoustic velocity oscillations and solid propellant combustion. *Tech. Rep.*. United Technologies Chemical Systems, San Jose, CA. (Cited on page 19.)

Busse, F.H. 1984 Oscillations of a rotating liquid drop. *J. Fluid Mech.* **142**, 1–8. (Cited on page 17.)

Butler, T. D. & O'Rourke, P. J. 1977 A numerical method for two-dimensional unsteady reacting flows. *Proc. Combust. Inst.* **16** (1), 1503 – 1515. (Cited on page 160.)

Cabral, B. & Leedom, L.C. 1993 Imaging vector fields using line integral convolution. *Proceedings of the 20th annular conference on computer graphics and interactive techniques* pp. 263–270. (Cited on page 175.)

Campa, G. & Camporeale, S.M. 2014 Influence of nonlinear effects on the limit cycle in a combustion chamber equipped with helmholtz resonators. *ASME Paper 2014-GT-25228* . (Cited on page 88.)

Campa, G., Camporeale, S.M., Guaus, A., Favier, J., Bargiacchi, M., Bottaro, A., Cosatto, E. & Mori, G. 2011 A quantitative comparison between a low order model and a 3d fem code for the study of thermoacoustic combustion instabilities. *ASME Paper 2011-GT-45969* . (Cited on pages 27, 87, 88, 89, 93, 120, 235, and 236.)

Candel, S. 1992 Combustion instabilities coupled by pressure waves and their active control. *Proc. Combust. Inst.* **24**, 1277–1296. (Cited on pages 19 and 21.)

Candel, S. 2002 Combustion dynamics and control:. *Proc. of the Combustion Institute* **29**, 1–28. (Cited on pages 18, 19, and 23.)

Candel, S., Durox, D., Schuller, T., Bourgouin, J-F. & Moeck, J.P. 2014 Dynamics of swirling flames. *Annu. Rev. fluid Mech.* **46**, 147–173. (Cited on page 25.)

Chantrasmi, T., Constantine, P., Etemadi, N., Iaccarino, G. & Wang, Q. 2006 Uncertainty quantification in simple linear and non-linear problems. *Annual Research Briefs of CTR* . (Cited on page 118.)

Chantrasmi, T. & Iaccarino, G. 2012 Forward and backward uncertainty propagation for discontinuous system response using the padé-legendre method. *International Journal of Uncertainty Quantification* **2** (2), 125–143. (Cited on page 127.)

Charlette, F., Veynante, D. & Meneveau, C. 2002 A power-law wrinkling model for LES of premixed turbulent combustion: Part I - non-dynamic formulation and initial tests. *Combust. Flame* **131**, 159–180. (Cited on pages 162, 172, and 188.)

Chu, B. T. 1965 On the energy transfer to small disturbances in fluid flow (part i). *Acta Mechanica* pp. 215–234. (Cited on page 24.)

Clanet, C., Searby, G. & Clavin, P. 1999 Primary acoustic instability of flames propagating in tubes: cases of spray and premixed gas combustion. *J. Fluid Mech.* **385** (157-197). (Cited on page 25.)

Clavin, P. & Joulin, G. 1983 Premixed flames in large scale and high intensity turbulent flow. *J. Physique Lettres* **44**, L1–L12. (Cited on page 23.)

Clavin, P. & Siggia, E. D. 1991 Turbulent premixed flames and sound generation. *Combust. Sci. Tech.* **78**, 147–155. (Cited on page 19.)

Colin, O., Ducros, F., Veynante, D. & Poinsot, T. 1999 A thickened flame model for large eddy simulations of turbulent premixed combustion. *Tech. Rep.* HEP/123-qed. CERFACS. (Cited on page 28.)

Colin, O., Ducros, F., Veynante, D. & Poinsot, T. 2000 A thickened flame model for large eddy simulations of turbulent premixed combustion. *Phys. Fluids* **12** (7), 1843–1863. (Cited on pages 159, 161, 163, and 172.)

Colin, O. & Rudgyard, M. 2000 Development of high-order taylor-galerkin schemes for unsteady calculations. *J. Comput. Phys.* **162** (2), 338–371. (Cited on page 158.)

Comte, P., Haberkorn, M., Bouchet, G., Pagneaux, V. & Auregan, Y. 2006 *Large-Eddy Simulation of acoustic propagation in a turbulent channel flow*, pp. 521–528. Direct and Large Eddy Simulation VI. (Cited on page 211.)

Constantine, P. G., Dow, E. & Wang, Qiqi 2014 Active subspace methods in theory and pratice: applications to kriging surfaces. *SIAM Journal on Scientific Computing* **36** (4), 1500–1524. (Cited on pages 120 and 127.)

Creighton, J. A. 1982 Splitting of degenerate vibrational modes due to symmetry perturbations in tetrahedral m4 and octahedral m6 clusters. *Inorganic Chemistry* **21** (1), 1–4. (Cited on page 15.)

Crighton, D. G., Dowling, A. P., Williams, J. E. Ffowcs, Heckl, M. & Leppington, F. 1992 *Modern methods in analytical acoustics*. New-York: Springer Verlag. (Cited on page 21.)

Crocco, L. 1951 Aspects of combustion instability in liquid propellant rocket motors. Part I. *J. American Rocket Society* **21**, 163–178. (Cited on pages 47, 54, 94, 102, 167, 173, and 174.)

Crocco, L. 1952 Aspects of combustion instability in liquid propellant rocket motors. part II. *J. American Rocket Society* **22**, 7–16. (Cited on page 119.)

Crocco, L. 1969 Research on combustion instability in liquid propellant rockets. *Proc. Combust. Inst.* **12**, 85–99. (Cited on page 25.)

Culick, F. E. C. 1987 Combustion instabilities in liquid-fueled propulsion systems- an overview. *AGARD 72B PEP meeting* . (Cited on page 18.)

Culick, F. E. C. & Kuentzmann, P. 2006 *Unsteady Motions in Combustion Chambers for Propulsion Systems*. NATO Research and Technology Organization. (Cited on pages 18 and 33.)

Cummings, D.L. & Blackburn, D.A. 1991 Oscillations of magnetically levitated aspherical droplets. *J. Fluid Mech.* **224**, 395–416. (Cited on page 17.)

Cuquel, A., Durox, D. & Schuller, T. 2011 Theoretical and experimental determination of the flame transfer function of confined premixed conical flames. *Proceedings of the seventh Mediterranean Combustion Symposium* . (Cited on page 25.)

Davey, A. & Salwen, H. 1994 On the stability in an elliptic pipe which is nearly circular. *J. Fluid Mech.* **281**, 357–369. (Cited on page 17.)

Davies, P. O. A. L. 1988 Practical flow duct acoustics. *J. Sound Vib.* **124** (1), 91–115. (Cited on page 46.)

Dawson, J.R. & Worth, N.A. 2014 The effect of baffles on self-excited azimuthal modes in an annular combustor. *Proc. Combust. Inst. (in press)* . (Cited on pages 34, 218, 235, 237, and 239.)

Domingo, P., Vervisch, L. & Bray, K. 2002 Partially premixed flamelets in LES of non premixed turbulent combustion. *Combust. Theory and Modelling* **6** (529-551). (Cited on page 28.)

Dopazo, C. 1994 Recent developments in pdf methods. In *Turbulent Reacting Flows* (ed. P. A. Libby & F. A. Williams), pp. 375 – 474. London: Academic. (Cited on page 159.)

Dowling, A & Stow, R. S. 2003 Acoustic analysis of gas turbine combustors. *AIAA* **19**, 751–764. (Cited on page 19.)

Dowling, A. P. 1995 The calculation of thermoacoustic oscillations. *J. Sound Vib.* **180** (4), 557–581. (Cited on pages 19, 26, 46, 75, and 204.)

Dowling, A. P. 1997 Nonlinear self-excited oscillations of a ducted flame. *J. Fluid Mech.* **346**, 271–290. (Cited on page 19.)

Duchaine, F. & Poinsot, T. 2011 Sensitivity of flame transfer functions of laminar flames. *Proc. of the Summer Program* pp. 250–258. (Cited on page 205.)

Duchaine, F., Selle, L. & Poinsot, T. 2011 Sensitivity analysis of transfer functions of laminar flames. *Combust. Flame* **158** (12), 2384–2394. (Cited on pages 29, 120, 167, and 173.)

Ducros, F., Nicoud, F. & Poinsot, T. 1998 Wall-adapating local eddy-viscosity models for simulations in complex geometries. *ICFD* pp. 293–300. (Cited on page 157.)

Duran, I. & Moreau, S. 2013 Solution of the quasi-one-dimensional linearized euler equations using flow invariants and the magnus expansion. *J. Fluid Mech.* **723**, 190–231. (Cited on page 26.)

Enaux, B., Granet, V., Vermorel, O., Lacour, C., Pera, C., Angelberger, C. & Poinsot, T. 2011 Les and experimental study of cycle-to-cycle variations in a spark ignition engine. *Proc. Combust. Inst.* **33**, 3115–3122. (Cited on page 163.)

Evesque, S. & Polifke, W. 2002 Low-order acoustic modelling for annular combustors: Validation and inclusion of modal coupling. *ASME Paper 2002-GT-30064* . (Cited on pages 19, 26, 27, 32, 204, and 222.)

Evesque, S., Polifke, W. & Pankiewitz, C. 2003 Spinning and azimuthally standing acoustic modes in annular combustors. *AIAA Paper 2003-3182* . (Cited on pages 21, 32, and 87.)

Feng, Z.C. & Sethna, P.R. 1989 Symmetry-breaking bifurcation in resonant surface waves. *J. Fluid Mech.* **199**, 495–518. (Cited on pages 15 and 16.)

Fiorina, B., Vicquelin, R., Auzillon, P., Darabiha, N. & Veynante, D. 2010 A filtered tabulated chemistry model for les of premixed combustion. *Combust. Flame* **157** (3), 465–475. (Cited on page 163.)

Forkel, H. & Janicka, J. 2000 Large-eddy simulation of a turbulent hydrogen diffusion flame. *Flow, Turb. and Combustion* **65** (2), 163–175. (Cited on page 28.)

Franzelli, B., Riber, E. & Cuenot, B. 2013 Impact of the chemical description on a large eddy simulation of a lean partially premixed swirled flame. *Combustion, spray and flow dynamics for aerospace propulsion* **341** (1-2), 247–256. (Cited on pages 152 and 166.)

Franzelli, B., Riber, E., Sanjosé, M. & Poinsot, T. 2010 A two-step chemical scheme for Large-Eddy Simulation of kerosene-air flames. *Combust. Flame* **157** (7), 1364–1373. (Cited on page 173.)

Frenklach, M., Wang, H., Goldenberg, M., Smith, G. P., Golden, D. M., Bowman, C. T., Hanson, R. K., Gardiner, W. C. & Lissianki, V. 1995 GRI-mech: an optimized detailed chemical reaction mechanism for methane combustion. *Tech. Rep.* GRI-Report GRI-95/0058. Gas Research Institute. (Cited on page 173.)

Fureby, C. 2010 LES of a multi-burner annular gas turbine combustor. *Flow, Turb. and Combustion* **84**, 543–564. (Cited on pages 169 and 220.)

Gelbert, G., Moeck, J.P., Paschereit, C.O. & King, R. 2012 Feedback control of unstable thermoacoustic modes in an annular rijke tube. *Control Engineering Practice* **20**, 770–782. (Cited on pages 33, 44, and 218.)

Ghirardo, G. & Juniper, M. 2013 Azimuthal instabilities in annular combustors: standing and spinning modes. *Proceedings of the Royal Society A* (2013-0232). (Cited on pages 72, 84, 87, 89, 218, 235, and 252.)

Ghirardo, G., Juniper, M.P. & Moeck, J.P. 2015 Stability criteria for standing and spinning waves in annular combustors. *Turbo Expo GT2015-43127* . (Cited on pages 25, 43, 249, 251, and 252.)

Giauque, A., Selle, L., Poinsot, T., Buechner, H., Kaufmann, P. & Krebs, W. 2005 System identification of a large-scale swirled partially premixed combustor using LES and measurements. *J. Turb.* **6** (21), 1–20. (Cited on page 167.)

Giret, J-C., Sengissens, A., Moreau, S. & Jouhaud, J-C. 2013 Prediction of lagoon landing-gear noise using an unstructured les solver. *19th AIAA/CEAS Aeronautics conference* . (Cited on page 240.)

Goodwin, D.G. 2009 Cantera code site (http://code.google.com/p/cantera/). (Cited on page 173.)

Guckenheimer, J. & Mahalov, A. 1992 Instability induced by symmetry reduction. *Physical Review Letter* **68**, 2257. (Cited on page 17.)

Guezennec, N. & Poinsot, T. 2009 Acoustically nonreflecting and reflecting boundary conditions for vorticity injection in compressible solvers. *AIAA Journal* **47**, 1709–1722. (Cited on page 212.)

Guslienko, K.Y., A.N.Slavin, Tiberkevich, V. & Kim, S.K. 2008 Dynamic origin of azimuthal modes splitting in vortex-state magnetic dots. *Physical Review Letter* **24**, 247203. (Cited on pages 15 and 16.)

Harrje, D. J. & Reardon, F. H. 1972 Liquid propellant rocket instability. *Tech. Rep.* Report SP-194. NASA. (Cited on page 18.)

Hawkes, E. R. & Cant, S. R. 2000 A flame surface density approach to large eddy simulation of premixed turbulent combustion. *Proc. Combust. Inst.* **28**, 51–58. (Cited on page 159.)

Heckl, M.A. & Howe, M.S. 2007 Stability analysis of the rijke tube with a green's function approach. *Journal of Sound and Vibration* **305**, 672–688. (Cited on page 259.)

Hirsch, C. 2007 Finite volume method and conservative discretization with an introduction to finite element method. In *Numerical Computation of internal & external flows: Fundamentals of Computational Fluid Dynamics, second edition*, chap. 5, pp. 203–248. New York: John Wiley & Sons. (Cited on page 158.)

Hirschfelder, J. O., Curtiss, C. F. & Bird, R. B. 1969 *Molecular theory of gases and liquids*. New York: John Wiley & Sons. (Cited on page 143.)

Hoffmann, F., Woltersdorf, G., Perzlmaier, K., Slavin, A.N., Tiberkevich, V.S., Bischof, A., Weiss, D. & Back, C.H. 2007 Mode degeneracy due to vortex core removal in magnetic disks. *Physical Review B* **76**, 014416. (Cited on pages 15 and 16.)

Howe, M. S. 1979 On the theory of unsteady high reynolds number flow through a circular aperture. *Proc. R. Soc. Lond. A , Mathematical and Physical Sciences* **366** (1725), 205–223. (Cited on page 26.)

Howe, M. S. 1997 Influence of wall thickness on Rayleigh conductivity and flow-induced aperture tones. *J. Fluids Struct.* **11** (4), 351–366. (Cited on page 26.)

J. Kopitz, E. Brocker, W. Polifke 2005 Characteristics-based filter for identification of planar acoustic waves in numerical simulation of turbulent compressible flow. *12th International Congress on Sound and Vibration* . (Cited on page 28.)

Janicka, J. & Sadiki, A. 2004 Large eddy simulation for turbulent combustion. *Proc. Combust. Inst.* **30**, 537–547. (Cited on page 28.)

Jiménez, C., Quinard, J., Grana-Otero, J., Schmidt, H. & Searby, G. 2012 Unsteady response of hydrogen and methane flames to pressure waves. *Combust. Flame* **159**, 1894–1908. (Cited on page 25.)

Jones, W. P. & Whitelaw, J. H. 1982 Calculation methods for reacting turbulent flows: a review. *Combust. Flame* **48**, 1–26. (Cited on page 28.)

Juniper, M.P., Magri, L., Bauerheim, M. & Nicoud, F. 2015 Applications of adjoint methods in thermoacoustics. *Proc. of the Summer Program* . (Cited on page 128.)

Kaess, R., Polifke, W., Poinsot, T., Noiray, N., Durox, D., Schuller, T. & Candel, S. 2008 Cfd-based mapping of the thermo-acoustic stability of a laminar premix burner. *Proc. of the Summer Program* pp. 289–302. (Cited on pages 167 and 259.)

Kammerer, M., Weigand, M., Curcic, M., Sproll, M., Vansteenkiste, A., Waeyenberge, B. Van, Stoll, H., Woltersdorf, G., Back, C.H. & Schuetz, G. 2011 Magnetic vortex core reversal by excitation of spin waves. *Nature communication* **2**, 279. (Cited on pages 15 and 16.)

Kaufmann, A., Nicoud, F. & Poinsot, T. 2002 Flow forcing techniques for numerical simulation of combustion instabilities. *Combust. Flame* **131**, 371–385. (Cited on page 205.)

Kedia, K.S., Altay, H.M. & Ghoniem, A.F. 2011 Impact of flame-wall interaction on premixed flame dynamics and transfer function characteristics. *Proc. Combust. Inst.* **33**, 1113–1120. (Cited on pages 173, 176, 188, and 205.)

Kippenberg, T.J. 2010 Microresonators: particle sizing by mode splitting. *Nature Photonics* **4**, 9–10. (Cited on page 16.)

Kolmogorov, A. N. 1941 The local structure of turbulence in incompressible viscous fluid for very large reynolds numbers. *C. R. Acad. Sci. , USSR* **30**, 301. (Cited on pages 27, 144, and 156.)

Kopitz, J., Huber, A., Sattelmayer, T. & Polifke, W. 2005 Thermoacoustic stability analysis of an annular combustion chamber with acoustic low order modeling and validation against experiment. *ASME Paper 2005-GT-68797* . (Cited on pages 19, 23, 25, and 32.)

Kosovichev, A.G. 1999 Inversion methods in helioseismology and solar tomography. *Journal of computational and applied mathematics* **109**, 1–39. (Cited on page 16.)

Krebs, W., Flohr, P., Prade, B. & Hoffmann, S. 2002 Thermoacoustic stability chart for high intense gas turbine combustion systems. *Combust. Sci. Tech.* **174**, 99–128. (Cited on pages 15, 21, 26, 32, 72, 87, 218, and 222.)

Krebs, W., Walz, G., Flohr, P. & Hoffmann, S. 2001 Modal analysis of annular combustors: effect of burner impedance. *ASME Paper 2001-GT-42* . (Cited on pages 76 and 235.)

Krstic, M., Krupadanam, A. & Jacobson, C.; 1999 Self-tuning control of a nonlinear model of combustion instabilities. *Control Systems Technology* **7**. (Cited on page 20.)

Krüger, U., Hüren, J., Hoffmann, S., Krebs, W. & Bohn, D. 1999 Prediction of thermoacoustic instabilities with focus on the dynamics flame behavior for the 3a-series gas turbines of siemes kwu. *ASME Turbo Expo 99-GT-111* . (Cited on page 26.)

Krüger, U., Hüren, J., Hoffmann, S., Krebs, W., Flohr, P. & Bohn, D. 2000 Prediction and measurement of thermoacoustic improvements in gas turbines with annular combustion systems. *J. Eng. for Gas Turbines and Power* **123** (3), 557–566. (Cited on pages 26, 33, 43, 54, 62, and 63.)

Kuenne, G., Ketelheun, A. & Janicka, J. 2011 LES modeling of premixed combustion using a thickened flame approach coupled with fgm tabulated chemistry. *Combust. Flame* **158** (9), 1750 – 1767. (Cited on pages 169 and 220.)

Kumar, A. & Krousgrill, C.M. 2012 Mode-splitting and quasi-degeneracies in circular plate vibration problems: The example of free vibrations of the stator of a travelling wave ultrasonic motor. *J. Sound Vib.* **331** (26), 5788–5802. (Cited on page 15.)

Kuo, K.K. 2005 *Principles of combustion*. Hoboken, New Jersey: John Wiley & Sons, Inc. (Cited on page 160.)

Lamarque, N. 2007 Schémas numériques et conditions limites pour la simulation aux grandes échelles de la combustion diphasique dans les foyers d'hélicoptère. Phd thesis, INP Toulouse. (Cited on page 158.)

Lavely, E.M. 1983 Theoretical investigations in helioseismology. PhD thesis, Columbia University. (Cited on pages 15 and 16.)

Lax, P. D. & Wendroff, B. 1960 Systems of conservation laws. *Commun. Pure Appl. Math.* **13**, 217–237. (Cited on page 158.)

Lecocq, G., Hernandez-Vera, T., Poitou, D., Riber, E. & Couenot, B. 2013 Soot prediction by large-eddy simulation of complex geometry combustion chambers. *Comptes rendus de l'Académie des Sciences - Mécanique* **341** (1-2), 230–237. (Cited on page 173.)

Lee, D. S. & Anderson, T. J. 1999 Measurements of fuel/air-acoustic coupling in lean premixed combustion systems. *AIAA paper 99-0450* . (Cited on page 19.)

Lee, J. G. & Santavicca, D.A. 2003 Experimental diagnostics for the study of combustion instabilities in lean premixed combustors. *Journal of Propulsion and Power* **19**, 735–750. (Cited on page 19.)

Légier, J.-Ph., Poinsot, T. & Veynante, D. 2000 Dynamically thickened flame LES model for premixed and non-premixed turbulent combustion. *Proc. of the Summer Program* pp. 157–168. (Cited on pages 159 and 162.)

Légier, J.-Ph., Varoquié, B., Lacas, F., Poinsot, T. & Veynante, D. 2002 Large eddy simulation of a non-premixed turbulent burner using a dynamically thickened flame model. In *IUTAM Symposium on Turbulent Mixing and Combustion*, pp. 315 – 326. Kluwer Academic Publishers. (Cited on page 163.)

Lepers, J., Krebs, W., Prade, B., Flohr, P., Pollarolo, G. & Ferrante, A. 2005 Investigation of thermoacoustic stability limits of an annular gas turbine combustor test-rig with and without helmholtz resonators. *ASME Turbo Expo GT2005-68246* . (Cited on page 26.)

Lespinasse, F., Baillot, F. & Boushaki, T. 2013 Response of v-flames placed in an hf transverse acoustic field from a velocity to pressure antinode. *Comptes rendus de l'Académie des Sciences - Mécanique* **341**, 110–120. (Cited on pages 21 and 172.)

Levich, E. & Tsinober, A. 1983 On the role of helicity structures in three-dimensional turbulent flow. *Phys. Lett. A* **93** (6), 293–297. (Cited on page 17.)

Lieuwen, T. 2001 Theoretical investigation of unsteady flow interactions with a premixed planar flame. *J. Fluid Mech.* **435**, 289–303. (Cited on page 25.)

Lieuwen, T. & Neumeier, Y. 2002 Nonlinear pressure-heat release transfer function measurements in a premixed combustor. *Proc. Combust. Inst.* **29**, 99–105. (Cited on page 20.)

Lieuwen, T. & Yang, V. 2005 *Combustion Instabilities in Gas Turbine Engines. Operational Experience, Fundamental Mechanisms and Modeling*, , vol. 210. Progress in Astronautics and Aeronautics, AIAA. (Cited on pages 18, 21, and 87.)

Lieuwen, T. & Zinn, B. T. 1998 The role of equivalence ratio oscillations in driving combustion instabilities in low nox gas turbines. *Proc. Combust. Inst.* **27**, 1809–1816. (Cited on page 20.)

Lin, J. & Parker, R.G. 2000*a* Mesh stiffness variation instabilities in two-stage gear systems. *Journal of Vibration and Acoustics* **124**, 68–76. (Cited on page 15.)

Lin, J. & Parker, R.G. 2000*b* Structured vibration characteristics of planetary gears with unequally spaced planets. *J. Sound Vib.* **235** (5), 921–928. (Cited on page 15.)

Lumley, J. 1967 The structure of inhomogeneous turbulent flows. *Atmospheric Turbulent and Radio Wave Propagation* pp. 166–178. (Cited on page 28.)

Lynch, E.D. 2011 High fidelity modeling program approach. *ALREST, Technical meeting* . (Cited on pages 18 and 19.)

Marble, F. E. & Candel, S. 1977 Acoustic disturbances from gas nonuniformities convected through a nozzle. *J. Sound Vib.* **55**, 225–243. (Cited on pages 26 and 44.)

Mazzei, A., Gotzinger, S., de S. Menezes, L., Zumofen, G., Benson, O. & Sandoghdar, V. 2007 Controlled coupling of counterpropagating whispering-gallery modes by a single rayleigh scatterer: a classical problim in a quantum optical light. *Physical Review Letter* **99**, 173603. (Cited on page 16.)

McIntosh, A.C. 1993 The linearized response of the mass burning rate of a premixed flame to rapid pressure changes. *Combust. Sci. Tech.* **91**, 329–346. (Cited on page 25.)

McManus, K., Poinsot, T. & Candel, S. 1993 A review of active control of combustion instabilities. *Prog. Energy Comb. Sci.* **19**, 1–29. (Cited on page 19.)

Meier, W., Weigand, P., Duan, X.R. & Giezendanner-Thoben, R. 2007 Detailed characterization of the dynamics of thermoacoustic pulsations in a lean premixed swirl flame. *Combust. Flame* **150** (1-2), 2–26. (Cited on page 166.)

Mejia, D., Selle, L., Bazile, R. & Poinsot, T. 2014 Wall-temperature effects on flame response to acoustic oscillations. *Proc. Combust. Inst. (in press)* . (Cited on pages 26, 29, 173, and 181.)

Mendez, S. & Eldredge, J. 2009 Acoustic modeling of perforated plates with bias flow for large-eddy simulations. *J. Comput. Phys.* **228** (13), 4757–4772. (Cited on page 26.)

Moeck, J.P., Bourgouin, J-F., Durox, D., Schuller, T. & Candel, S. 2012 Non-linear interaction between a precessing vortex core and acoustic oscillations in a turbulent swirl flame. *Combust. Flame* **159**, 2650–2668. (Cited on page 25.)

Moeck, J.P., Paul, M. & Paschereit, C. 2010 Thermoacoustic instabilities in an annular flat rijke tube. *ASME Paper 2010-GT-23577* . (Cited on pages 26, 33, 44, 89, 218, 219, and 235.)

Moin, P. 2002 Advances in large eddy simulation methodology for complex flows. *Int. J. Heat Fluid Flow* **23** (5), 710–720. (Cited on page 28.)

Motheau, E., Nicoud, F. & Poinsot, T. 2012 Using boundary conditions to account for mean flow effects in a zero mach number acoustic solver. *ASME Paper 2012-GT-68852* . (Cited on pages 26 and 75.)

Moureau, V., Fiorina, B. & Pitsch, H. 2009 A level set formulation for premixed combustion LES considering the turbulent flame structure. *Combust. Flame* **156** (4), 801–812. (Cited on page 159.)

Moureau, V., Lartigue, G., Sommerer, Y., Angelberger, C., Colin, O. & Poinsot, T. 2005 Numerical methods for unsteady compressible multi-component reacting flows on fixed and moving grids. *J. Comput. Phys.* **202** (2), 710–736. (Cited on pages 158, 169, 188, and 221.)

Myers, M.K. 1986 An exact energy corollary for homentropic flow. *J. Sound Vib.* **109**, 277–284. (Cited on page 266.)

Ndiaye, A., Bauerheim, M., Moreau, S. & Nicoud, F. 2015 Uncertainty quantification of thermo-acoustic instabilities in a swirled stabilized combustor. *ASME Turbo Expo (accepted)* . (Cited on pages 129 and 138.)

Nicoud, F., Baya-Toda, H., Cabrit, O., Bose, S. & Lee, J. 2011 Using singular values to build a subgrid-scale model for large eddy simulations. *Physics of fluids* **23** (085106), 1–12. (Cited on pages 158 and 172.)

Nicoud, F., Benoit, L., Sensiau, C. & Poinsot, T. 2007 Acoustic modes in combustors with complex impedances and multidimensional active flames. *AIAA Journal* **45**, 426–441. (Cited on pages 27, 43, 52, 54, 55, 80, 102, 103, 119, 167, 174, 204, and 222.)

Nicoud, F. & Ducros, F. 1999 Subgrid-scale stress modelling based on the square of the velocity gradient. *Flow, Turb. and Combustion* **62** (3), 183–200. (Cited on pages 27, 172, and 188.)

Nicoud, F. & Poinsot, T. 2005 Thermoacoustic instabilities: should the rayleigh criterion be extended to include entropy changes ? *Combust. Flame* **142**, 153–159. (Cited on pages 24 and 105.)

Nicoud, F. & Wieczorek, K. 2009 About the zero mach number assumption in the calculation of thermoacoustic instabilitie. *Int. J. Spray and Combustion Dynamic* **1**, 67–112. (Cited on pages 26 and 204.)

Noiray, N., Bothien, M. & Schuermans, B. 2011 Analytical and numerical analysis of staging concepts in annular gas turbines. *Combustion Theory and Modelling* **15** (5), 585–606. (Cited on pages 15, 17, 22, 31, 33, 44, 52, 57, 72, 80, 81, 82, 84, 87, 89, 120, 196, 204, 214, 218, 235, 239, 243, 244, and 252.)

Noiray, N., Durox, D., Schuller, T. & Candel, S. 2008 A unified framework for nonlinear combustion instability analysis based on the flame describing function. *J. Fluid Mech.* **615**, 139–167. (Cited on pages 25, 26, 167, 218, and 249.)

Noiray, N. & Schuermans, B. 2013 On the dynamic nature of azimuthal thermoacoustic modes in annular gas turbine combustion chambers. *Proceedings of the Royal Society A* **469** (2151), 1471–2946. (Cited on pages 31, 32, 72, 235, and 238.)

O'Connor, J. & T.Lieuwen 2012*a* Further characterization of the disturbance field in a transversely excited swirl-stabilized flame. *Journal of Engineering for Gas Turbines and Power* **134** (011501-9). (Cited on page 91.)

O'Connor, J. & T.Lieuwen 2012*b* Influence of transverse acoustic modal structure on the forced response of a swirling nozzle flow. *ASME Paper 2012-GT-70053* . (Cited on pages 21 and 46.)

O'Connor, J. & T.Lieuwen 2012*c* Recirculation zone dynamics of a transversely excited swirl flow and flame. *Physics of fluids* **24** (075107). (Cited on pages 17, 21, 32, 46, 75, 91, and 172.)

Oefelein, J. C. & Yang, V. 1993 Comprehensive review of liquid-propellant combustion instabilities in f-1 engines. *J. Prop. Power* **9** (5), 657–677. (Cited on page 32.)

Orr, W. McFadden 1907*a* The stability or instability of the steady motions of a perfect liquid and of a viscous liquid. part i: A perfect liquid. *Proceedings of the Royal Irish Academy* **27**, 9–68. (Cited on page 205.)

Orr, W. McFadden 1907*b* The stability or instability of the steady motions of a perfect liquid and of a viscous liquid. part ii: A viscous liquid. *Proceedings of the Royal Irish Academy* **27**, 69–138. (Cited on page 205.)

Palies, P. 2010 Dynamique et instabilités de combustion de flammes swirlées. Phd thesis, Ecole Centrale Paris. (Cited on pages 25, 47, and 76.)

Palies, P, Durox, D, Schuller, T & Candel, S 2011 Experimental study on the effect of swirler geometry and swirl number on flame describing functions. *Combustion Science and Technology* **183** (7), 704–717. (Cited on page 25.)

Pang, L., Tetz, K.A. & Fainman, Y. 2007 Observation of the splitting of degenerate surface plasmon polariton modes in a two-dmiensional metallic nanohole array. *Applied Physics Letters* **90** (11), 111103. (Cited on page 15.)

Pankiewitz, C. & Sattelmayer, T. 2003 Time domain simulation of combustion instabilities in annular combustors. *ASME Journal of Engineering for Gas Turbines and Power* **125** (3), 677–685. (Cited on pages 27, 32, 87, 120, and 204.)

Parmentier, J.F., Salas, P., Wolf, P., Staffelbach, G., Nicoud, F. & Poinsot, T. 2012 A simple analytical model to study and control azimuthal instabilities in annular combustion chamber. *Combustion and Flame* **159**, 2374–2387. (Cited on pages 15, 17, 26, 31, 32, 36, 42, 43, 44, 45, 47, 52, 74, 76, 77, 79, 88, 89, 99, 100, 115, 120, 235, 236, and 253.)

Paschereit, C. O., Polifke, W., Schuermans, B. & Mattson, O. 2002 Measurement of transfer matrices and source terms of premixed flames. *J. Eng. Gas Turb. and Power* **124**, 239–247. (Cited on page 204.)

Passot, T. & Pouquet, A. 1987 Numerical simulation of compressible homogeneous flows in the turbulent regime. *J. Fluid Mech.* **181**, 441–466. (Cited on page 211.)

Perrin, R. & Charnley, T. 1973 Group theory and the bell. *J. Sound Vib.* **31** (4), 411–418. (Cited on pages 15, 32, 33, 57, 58, and 68.)

Pierce, A. D. 1981 *Acoustics: an introduction to its physical principles and applications*. New York: McGraw Hill. (Cited on pages 55 and 103.)

Piomelli, U., Moin, P. & Ferziger, J. H. 1988 Model consistency in large eddy simulation of turbulent channel flows. *Phys. Fluids* **31** (7), 1884–1891. (Cited on page 28.)

Pitsch, H. 2006 Large eddy simulation of turbulent combustion. *Ann. Rev. Fluid Mech.* **38**, 453–482. (Cited on page 28.)

Poinsot, T. 1987 Analyse des instabilités de combustion de foyers turbulents prémélangés. Thèse d'etat, Université d'Orsay. (Cited on page 29.)

Poinsot, T., Echekki, T. & Mungal, M. G. 1992 A study of the laminar flame tip and implications for premixed turbulent combustion. *Combust. Sci. Tech.* **81** (1-3), 45–73. (Cited on pages 29, 169, 188, and 221.)

Poinsot, T., Trouvé, A., Veynante, D., Candel, S. & Esposito, E. 1987 Vortex driven acoustically coupled combustion instabilities. *J. Fluid Mech.* **177**, 265–292. (Cited on pages 19 and 25.)

Poinsot, T. & Veynante, D. 2005 *Theoretical and Numerical Combustion*. R.T. Edwards, 2nd edition. (Cited on pages 21, 23, 26, and 119.)

Poinsot, T. & Veynante, D. 2011 *Theoretical and Numerical Combustion*. Third Edition (www.cerfacs.fr/elearning). (Cited on pages 18, 28, 46, 54, 93, 94, 105, 145, 151, 161, 169, 204, 220, 222, and 259.)

Polifke, W. 1990 Aspects of helicity in turbulent flows. PhD thesis, City university of New York. (Cited on page 17.)

Polifke, W., Paschereit, C. & Doebbeling, K. 2001*a* Constructive and destructive interference of acoustic and entropy waves in a premixed combustor with a choked exit. *Int. J. Acoust. Vib.* **6**, 135–146. (Cited on page 26.)

Polifke, W., Poncet, A., Paschereit, C. O. & Doebbeling, K. 2001*b* Reconstruction of acoustic transfer matrices by instationnary computational fluid dynamics. *J. Sound Vib.* **245** (3), 483–510. (Cited on pages 119 and 204.)

Rayleigh, L. 1894 *The Theory of Sound*. Mac Millan (reprinted by Dover, New York, 1945). (Cited on pages 20 and 24.)

Riber, E., García., M., Moureau, V., Pitsch, H., Simonin, O. & Poinsot, T. 2006 Evaluation of numerical strategies for LES of two-phase reacting flows. *Proc. of the Summer Program* pp. 197–211. (Cited on page 28.)

Roache, P.J. 1997 Quantification of uncertainty in computational fluid dynamics. *Annu. Rev. fluid Mech.* **29**, 123–160. (Cited on page 118.)

Roux, A., Gicquel, L. Y. M., Sommerer, Y. & Poinsot, T. J. 2007 Large eddy simulation of mean and oscillating flow in a side-dump ramjet combustor. *Combust. Flame* **152** (1-2), 154–176. (Cited on page 28.)

Roux, S., Lartigue, G., Poinsot, T., Meier, U. & Bérat, C. 2005 Studies of mean and unsteady flow in a swirled combustor using experiments, acoustic analysis and large eddy simulations. *Combust. Flame* **141**, 40–54. (Cited on page 169.)

Sagaut, P. 2006 *Large eddy simulation for incompressible flows*. Springer-Verlag, 3rd Edition. (Cited on page 157.)

Saito, M., Hoshikawa, M. & Sato, M. 1996 Enhancement of evaporation/combustion rate coefficient of a single fuel droplet by acoustic oscillation. *Fuel* **75** (6), 669–674. (Cited on page 25.)

Sattelmayer, T. 2003 Influence of the combustor aerodynamics on combustion instabilities from equivalence ratio fluctuations. *J. Eng. Gas Turb. and Power* **125** (1), 11–19. (Cited on page 20.)

Schmid, P.J. 2010 Dynamic mode decomposition of numerical and experimental data. *J. Fluid Mech.* **656**, 5–28. (Cited on pages 178, 193, and 210.)

Schmitt, P., Poinsot, T., Schuermans, B. & Geigle, K. P. 2007 Large-eddy simulation and experimental study of heat transfer, nitric oxide emissions and combustion instability in a swirled turbulent high-pressure burner. *J. Fluid Mech.* **570**, 17–46. (Cited on page 28.)

Schønfeld, T. & Poinsot, T. 1999 Influence of boundary conditions in LES of premixed combustion instabilities. In *Annual Research Briefs* , pp. 73–84. Center for Turbulence Research, NASA Ames/Stanford Univ. (Cited on page 169.)

Schuermans, B., Paschereit, C. & Monkewitz, P. 2006 Non-linear combustion instabilities in annular gas-turbine combustors. *AIAA paper 2006-0549* . (Cited on pages 21, 22, 33, 72, and 87.)

Schuller, T., Durox, D. & Candel, S. 2003 A unified model for the prediction of laminar flame transfer functions: comparisons between conical and v-flames dynamics. *Combust. Flame* **134**, 21–34. (Cited on page 25.)

Schuller, T., Durox, D., Palies, P. & Candel, S. 2012 Acoustic decoupling of longitudinal modes in generic combustion systems. *Combustion and Flame* **159**, 1921–1931. (Cited on pages 26, 47, 76, 88, 100, 105, 115, 235, and 259.)

Searby, ed. 2008 *Le bruit de combustion*, 11e Ecole de Combustion. (Cited on page 19.)

Selle, L., Benoit, L., Poinsot, T., Nicoud, F. & Krebs, W. 2006 Joint use of compressible large-eddy simulation and Helmholtz solvers for the analysis of rotating modes in an industrial swirled burner. *Combust. Flame* **145** (1-2), 194–205. (Cited on pages 27, 43, and 54.)

Selle, L., Lartigue, G., Poinsot, T., Koch, R., Schildmacher, K.-U., Krebs, W., Prade, B., Kaufmann, P. & Veynante, D. 2004*a* Compressible large-eddy simulation of turbulent combustion in complex geometry on unstructured meshes. *Combust. Flame* **137** (4), 489–505. (Cited on page 163.)

Selle, L., Nicoud, F. & Poinsot, T. 2004*b* The actual impedance of non-reflecting boundary conditions: implications for the computation of resonators. *AIAA Journal* **42** (5), 958–964. (Cited on pages 26, 169, 188, and 221.)

Sengissen, A., Giauque, A., Staffelbach, G., Porta, M., Krebs, W., Kaufmann, P. & Poinsot, T. 2007 Large eddy simulation of piloting effects on turbulent swirling flames. *Proc. Combust. Inst.* **31**, 1729–1736. (Cited on pages 169 and 220.)

Sensiau, C. 2008 Simulations numériques des instabilités thermoacoustiques dans les chambres de combustion aéronautiques - th/cfd/08/127. PhD thesis, Université de Montpellier II, - Institut de Mathématiques et de Modélisation de Montpellier, France. (Cited on page 22.)

Sensiau, C., Nicoud, F. & Poinsot, T. 2009 A tool to study azimuthal and spinning modes in annular combustors. *Int. Journal Aeroacoustics* **8** (1), 57–68. (Cited on pages 22, 32, 33, 43, 54, 55, 57, 58, 69, and 72.)

Silva, C.F., Nicoud, F., Schuller, T., Durox, D. & Candel, S. 2013 Combining a helmholtz solver with the flame describing function to assess combustion instability

in a premixed swirled combustor. *Combustion and Flame* **160**, 1743–1754. (Cited on pages 27, 43, 54, 55, 249, and 250.)

Silva, F., Guillemain, Ph., Kergomard, J., Mallaroni, B. & Norris, A.N. 2009 Approximation formulae for the acoustic radiation impedance of a cylindrical pipe. *Journal of Sound and Vibration* **322**, 255–263. (Cited on pages 55 and 103.)

Simonelli, F. & Gollub, J.P. 1989 Surface wave mode interactions: effects of symmetry and degeneracy. *J. Fluid Mech.* **199**, 471–494. (Cited on pages 15, 16, and 17.)

Smagorinsky, J. 1963 General circulation experiments with the primitive equations: 1. the basic experiment. *Mon. Weather Rev.* **91**, 99–164. (Cited on pages 27, 157, and 172.)

Smirnov, A., Shi, S. & Celik, I. 2001 Random flow generation technique for large eddy simulations and particle-dynamics modeling. *Trans. ASME. J. Fluids Eng.* **123**, 359–371. (Cited on page 212.)

Smith, R., Anderson, W. & Merkle, C.L. 2010 Computational studies of the effects of oxidizer injector length on combustion instability. *AIAA 2010-6564* . (Cited on page 20.)

Smith, R., Xia, G., Anderson, W. & Merkle, C.L. 2012 Computational studies of the effects of oxidizer injector length on combustion instability. *Combustion Theory and Modelling* **16** (2), 2012. (Cited on page 20.)

Staffelbach, G., Gicquel, L.Y.M., Boudier, G. & Poinsot, T. 2009 Large eddy simulation of self-excited azimuthal modes in annular combustors. *Proc. Combust. Inst.* **32**, 2909–2916. (Cited on pages 19, 28, 32, 55, 72, 89, 90, 91, 218, and 225.)

Stow, S. & Dowling, A.P. 2004 Low-order modelling of thermoacoustic limit cycles. *ASME Paper 2004-GT-54245* . (Cited on pages 26 and 89.)

Stow, S. R. & Dowling, A. P. 2001 Thermoacoustic oscillations in an annular combustor. *ASME Paper 2001-GT-0037* . (Cited on pages 26, 32, and 75.)

Stow, S. R. & Dowling, A. P. 2003 Modelling of circumferential modal coupling due to helmholtz resonators. *ASME Paper 2003-GT-38168* . (Cited on pages 32, 75, 227, and 228.)

Strahle, W. 1985 A more modern theory of combustion noise. In *Recent Advances in the Aerospace Sciences*, pp. 103–114. New York: Plenum Press. (Cited on page 19.)

Strahle, W. C. 1972 Some results in combustion generated noise. *J. Sound Vib.* **23** (1), 113–125. (Cited on page 19.)

Stull, D. R. & Prophet, H. 1971 JANAF thermochemical tables, 2nd Edition. *Tech. Rep.* NSRDS-NBS 37. US National Bureau of Standards. (Cited on page 149.)

Tay Wo Chong, L., Kaess, R., Komarek, T., Foller, S. & Polifke, W. 2010 Identification of flame transfer functions using les of turbulent reacting flows. In *High Performance Computing in Science and Engineering, Garching/Munich 2009*, pp. 255–266. Springer Berlin Heidelberg. (Cited on page 205.)

Tay-Wo-Chong, L. & Polifke, W. 2012 Les-based study of the influence of thermal boundary condition and combustor confinement on premix flame transfer functions. *ASME Paper 2012-GT-68796* . (Cited on pages 29, 173, 176, and 181.)

Tran, N., Ducruix, S. & Schuller, T. 2009 Damping combustion instabilities with perforates at the premixer inlet of a swirled burner. *Proc. Combust. Inst.* **32** (2), 2917–2924. (Cited on page 26.)

Tripathy, S.C., Jain, K. & Bhatnagar, A. 2000 Helioseismic solar cycle changes and splitting coefficients. *J. Astrophys. Astr.* **21**, 349–352. (Cited on page 16.)

UCSD 2013 "chemical-kinetic mechanisms for combustion applications", san diego mechanism web page, ucsd. (Cited on pages 173 and 188.)

Venkataraman, K. K., Preston, L. H., W., Simons D., Lee, B.J., Lee, J.G. & Santavicca, D. 1999 Mechanism of combustion instability in a lean premixed dump combustor. *Journal of Propulsion and Power* **15**, 909–918. (Cited on page 19.)

Williams, F. A. 1985 *Combustion Theory*. Menlo Park, CA: Benjamin Cummings. (Cited on pages 23 and 160.)

Wolf, P., Staffelbach, G., Balakrishnan, R., Roux, A. & Poinsot, T. 2010 Azimuthal instabilities in annular combustion chambers. *Proc. of the Summer Program* pp. 259–269. (Cited on pages 19, 28, 163, 186, and 235.)

Wolf, P., Staffelbach, G., Gicquel, L.Y.M., Muller, J.D & T., Poinsot 2012 Acoustic and large eddy simulation studies of azimuthal modes in annular combustion chambers. *Combustion and Flame* **159**, 3398–3413. (Cited on pages 28, 32, 72, 87, 120, 169, 218, 220, 223, 224, 225, 235, and 267.)

Wolf, P., Staffelbach, G., Roux, A., Gicquel, L., Poinsot, T. & Moureau, V. 2009 Massively parallel LES of azimuthal thermo-acoustic instabilities in annular gas turbines. *C. R. Acad. Sci. Mécanique* **337** (6-7), 385–394. (Cited on pages 19, 21, 28, and 44.)

Worth, N.A. & Dawson, J.R. 2013*a* Modal dynamics of self-excited azimuthal instabilities in an annular combustion chamber. *Combustion and Flame* **160** (11), 2476–2489. (Cited on pages 22, 23, 28, 32, 33, 35, 36, 44, 73, 91, 166, 167, 168, 174, 188, 197, 206, 218, 219, 235, and 237.)

Worth, N.A. & Dawson, J.R. 2013*b* Self-excited cricumferential instabilities in a model annular gas turbine combustor: global flame dynamics. *Proceedings of the Combustion Institute* **34**, 3127–3134. (Cited on pages 5, 12, 22, 23, 28, 32, 33, 34, 36, 44,

69, 72, 73, 84, 89, 91, 120, 165, 166, 167, 168, 172, 173, 175, 176, 177, 184, 186, 187, 188, 189, 190, 196, 197, 198, 206, 218, 219, 223, 235, 237, and 267.)

Yang & Anderson 1995 Liquid rocket engine combustion instability, progress in astronautics and aeronautics. *AIAA* **169**. (Cited on page 18.)

You, D. & Moin, P. 2007*a* A dynamic global-coefficient subgrid-scale eddy-viscosity model for large-eddy simulation in complex geometries. *Phys. Fluids* **19** (6), 065110. (Cited on page 27.)

You, D. & Moin, P. 2007*b* A dynamic global-coefficient subgrid-scale model for large-eddy simulation of turbulent scalar transport in complex geometries. In *Annual Research Briefs* , pp. 169–182. Center for Turbulence Research, NASA Ames/Stanford Univ. (Cited on page 27.)

Zhao, Dan 2012 Transient growth of flow disturbances in triggering a rijke tube combustion instability. *Combustion and Flame* **159** (6), 2126–2137. (Cited on page 259.)

Résumé court

Une large gamme de problèmes physiques, des petites molécules aux étoiles géantes, contiennent des symétries de rotation et sont sujets à des oscillations azimutales ou transverses. Quand cette symétrie est rompue, le système peut devenir instable. Dans cette thèse, les brisures de symétries sont étudiées dans les chambres de combustion annulaires, sujettes à des instabilités thermo-acoustiques azimutales. En premier lieu, deux types de brisures sont obtenues analytiquement : la première en répartissant des bruleurs différents le long de la chambre et la seconde provoquée par le champ moyen lui-même. Ces ruptures de symétries entraînent une séparation des fréquences, fixe la structure du mode et peut déstabiliser le système. De plus, une approche Quantification d'Incertitudes (UQ) permet d'évaluer l'effet de la rupture de symétries provoquée par les incertitudes sur la description ou le comportement des flammes. Pour compléter cette théorie, des Simulations aux Grandes Echelles (SGE) sont réalisées sur un mono-secteur ainsi que sur une configuration complète 360° de l'expérience annulaire de Cambridge. Les résultats numériques sont comparés aux données expérimentales et montrent un bon accord. En particulier, un mode instable à 1800 Hz croît dans les deux cas. Cependant, la SGE, limitée par son coût important, ne permet pas l'étude du cycle limite s'établissant après plusieurs centaines de millisecondes. Pour palier à ce problème, une nouvelle approche, appelée AMT, est développée : les résultats d'une théorie ou d'un solveur acoustique sont injectés dans une simulation SGE. Cette approche permet d'étudier les brisures de symétries, la nature et la dynamique des modes acoustiques, ainsi que d'évaluer l'amortissement dans des configurations réalistes.

Short abstract

A large range of physical problems, from molecules to giant stars, contains rotating symmetry and can exhibit azimuthal waves or vibrations. When this symmetry is broken, the system can become unstable with chaotic behaviors. Symmetry breaking is investigated in annular combustors prone to azimuthal thermo-acoustic instabilities. First, theories reveal that two types of symmetry breaking exist : due to different burner types distributed allong the chamber or due to the flow itself . It leads to frequency splitting, fixes the mode structure and can destabilize the configuration. A UQ analysis is also performed to quantify the symmetry breaking effect due to uncertainties of flame descriptions or behaviors. To complete theory, Large Eddy Simulations are performed on a single-sector as well as on a complete 360° configuration of the annular experiment of Cambridge. Numerical results are compared to experimental data showing a good agreement. In particular, an unstable azimtuthal mode at 1800 Hz grows in both LES and experiment. However, LES cannot investigate the limit cycle because of its extreme cost. To tackle this problem, a new methodology is developed, called AMT, where theory or Helmholtz solver predictions are injected into LES or DNS. This method allows to study symmetry breaking, mode nature and dynamics as well as evaluating damping in realistic annular configurations.